Universidade Estadual de Campinas

Instituto de Física Gleb Wataghin

Pedro Antonio Santos Flórez

Atomistic simulations: mechanical properties of ice and nonequilibrium processes in repulsive binary mixtures

Simulações atomísticas: propriedades mecânicas do gelo e processos fora do equilíbrio em misturas binárias repulsivas

CAMPINAS
2020

Universidade Estadual de Campinas

Instituto de Física Gleb Wataghin

Pedro Antonio Santos Flórez

Atomistic simulations: mechanical properties of ice and nonequilibrium processes in repulsive binary mixtures

Simulações atomísticas: propriedades mecânicas do gelo e processos fora do equilíbrio em misturas binárias repulsivas

Thesis presented to the Institute of Physics "Gleb Wataghin" of the University of Campinas in partial fulfillment of the requirements for the degree of Doctor of Sciences, in the area of Physics.

Tese apresentada ao Instituto de Física "Gleb Wataghin" da Universidade Estadual de Campinas como parte dos requisitos exigidos para a obtenção do título de Doutor em Ciências, na área de Física.

Orientador: Prof. Dr. Maurice de Koning

Este exemplar corresponde à versão final da tese defendida pelo aluno Pedro Antonio Santos Flórez, e orientada pelo Prof. Dr. Maurice de Koning.

Campinas
2020

Ficha catalográfica
Universidade Estadual de Campinas
Biblioteca do Instituto de Física Gleb Wataghin
Lucimeire de Oliveira Silva da Rocha - CRB 8/9174

Santos Florez, Pedro Antonio, 1992-
Sa59a Atomistic simulations : mechanical properties of ice and nonequilibrium processes in repulsive binary mixtures / Pedro Antonio Santos Florez. – Campinas, SP : [s.n.], 2020.

Orientador: Maurice de Koning.
Tese (doutorado) – Universidade Estadual de Campinas, Instituto de Física Gleb Wataghin.

1. Gelo - Propriedades mecânicas. 2. Mecânica estatística de não-equilíbrio. 3. Dinâmica molecular. I. Koning, Maurice de, 1969-. II. Universidade Estadual de Campinas. Instituto de Física Gleb Wataghin. III. Título.

Informações para Biblioteca Digital

Título em outro idioma: Simulações atomísticas : propriedades mecânicas do gelo e processos fora do equilíbrio em misturas binárias repulsivas
Palavras-chave em inglês:
Ice - Mechanical properties
Nonequilibrium statistical mechanics
Molecular dynamics
Área de concentração: Física
Titulação: Doutor em Ciências
Banca examinadora:
Maurice de Koning [Orientador]
Alex Antonelli
Edison Zacarias da Silva
Caetano Rodrigues Miranda
Roberto Gomes de Aguiar Veiga
Data de defesa: 10-09-2020
Programa de Pós-Graduação: Física

Identificação e informações acadêmicas do(a) aluno(a)
- ORCID do autor: https://orcid.org/0000-0001-5264-923X
- Currículo Lattes do autor: http://lattes.cnpq.br/9721419328175328

MEMBROS DA COMISSÃO JULGADORA DA TESE DE DOUTORADO DE **PEDRO ANTONIO SANTOS FLÓREZ – RA 153917** APRESENTADA E APROVADA AO INSTITUTO DE FÍSICA "GLEB WATAGHIN", DA UNIVERSIDADE ESTADUAL DE CAMPINAS, EM 10 / 09 / 2020.

COMISSÃO JULGADORA:

- Prof. Dr. Maurice de Koning – Orientador – DFMC/IFGW/UNICAMP
- Prof. Dr. Alex Antonelli – DFMC/IFGW/UNICAMP
- Prof. Dr. Edison Zacarias da Silva – DFMC/IFGW/UNICAMP
- Prof. Dr. Caetano Rodrigues Miranda – IF/USP
- Prof. Dr. Roberto Gomes de Aguiar Veiga – CEMCSA/UFABC

OBS.: Ata da defesa com as respectivas assinaturas dos membros encontra-se no SIGA/Sistema de Fluxo de Dissertação/Tese e na Secretaria do Programa da Unidade.

CAMPINAS
2020

Dedico este trabajo a todos mis seres queridos quienes cerca o lejos siempre están presentes brindándome su apoyo.

Acknowledgements

I would first like to thank God for keeping me with enough energy to go on forever.

I would like to thank my advisor, Prof. Dr. Maurice de Koning, whom I consider a great professional and an excellent advisor. Thank you for your patience and dedication during these last years, for always being calm and reliable and for collaborating with me whenever I needed.

My sincerest thanks to all the people who somehow supported me in this process, to those who welcomed me to their country in the best possible way during all these years in Brazil,

I would like to thank to my parents, Pedro Antonio and Edelmira, my sisters, Luz Helena and Jenny and my beautiful and beloved partner Aline, for all their love and unconditional support and for encouraging me to always give my best. ¡Los quiero mucho!

I would like to thank to my housemates André, Breno, Giselle, Jaqueline, Rebeka and those who are gone (Jair, Jefry, Juliana, Marcelo and Rebecca) for sharing with me on a day-to-day life.

I would like to thank to my colleagues in the research group, Rodolfo, Ingrid, Jéssica, Victor and Danilo for the various meetings and discussions.

I would like to thank to Prof. Dr. Carlos Ruestes for his important collaboration during my doctorate, supervision in my internship in Argentina and friendship.

I would like to thank to Professors Alex Antonelli and Eduardo Miranda for

their excellent courses, and to Professors Luis Eduardo de Araujo, Francisco Rouxinol and Jean Rinkel for their supervision in the Teaching Internship Program (PED).

I would like to thank to Professors Marcus Aguiar, Alex Antonelli, Francisco Rouxinol and Edison Zacarias da Silva for the participation and suggestions on my qualifying exam and my PhD defense prerequisite seminar. Finally, I also thank Professors Maurice de Koning, Alex Antonelli, Edison Zacarias da Silva, Caetano Rodrigues Miranda and Roberto Gomes de Aguiar Veiga for their disposition in composing the judging committee of this Thesis.

I would like to acknowledge the IFGW Postgraduate Coordination, the functionaries of the Condensed Matter Physics Department, the John David Rogers Computer Center (CCJDR) for the management and maintenance of the Clusters and the DERI International Relations Executive Board for the financial support with resources from the Unicamp/Santander Agreement for my mobility to Argentina.

This study was financed in part by Coordenação de Aperfeiçoamento de Pessoal de Nível Superior - Brasil (CAPES) - Finance Code 001 (Process number: 1583238/2016).

Universidade Estadual de Campinas - UNICAMP

Campinas, SP - Brasil

September 2020

Pedro Antonio Santos Florez

"...if we were to name the most powerful assumption of all, which leads one on and on in an attempt to understand life, it is that all things are made of atoms, and that everything that living things do can be understood in terms of the jigglings and wigglings of atoms.".
Richard P. Feynman

Resumo

A partir do uso de técnicas de simulações atomísticas, que podem ser consideradas como un método de "microscopia computacional in situ", estudamos as propriedade mecânicas do gelo I_h observando em detalhe os mecanismos de deformação a escalas atómicas. Como segunda parte desta Tese, também investigamos através de simulações atomísticas, os processos fora do equilíbrio em misturas binárias repulsivas.

Usando simulações de dinâmica molecular, avaliamos a deformação uniaxial e a resposta à nanoindentação do gelo I_h, descrito por dois modelos populares de água, o potencial TIP4P/Ice e o modelo de água monoatômica (mW). Em particular, investigamos a resposta às deformações uniaxiais de tração e compressão ao longo de direções cristalográficas e temperaturas diferentes. Enquanto o modelo TIP4P/Ice falha por clivagem frágil sob tensão a baixas temperaturas ou por amorfização/fusão em larga escala, o potencial mW comporta-se de forma muito mais dúctil, apresentando inúmeros casos em que o alívio de tensão envolve a nucleação e subsequente atividade de discordâncias na estrutura cristalina. Estudamos também o processo de nanoindentação sob o plano basal, considerando duas temperaturas diferentes nas quais, respectivamente, uma camada quase-líquida (QLL) está ou não presente. A temperaturas muito baixas, na ausência de uma QLL, ambos os potenciais produzem curvas de carga e mecanismos de deformação similares. Perto da temperatura de fusão, porém, foram encontradas diferenças importantes, incluindo desvios na espessura e fração da QLL, bem como a presença de uma competição entre eventos de fusão e recristalização induzidos por pressão. No entanto, ambos os potenciais apresentam mecanismos de deformação semelhantes e estimativas de dureza que são consistentes com os dados experimentais.

Na segunda parte, consideramos os processos fora do equilíbrio de misturas binárias clássicas descritas por um conjunto de diferentes potenciais de interação de pares puramente repulsivos, nos quais uma configuração de temperatura infinita (gás ideal) é rapidamente resfriada até a temperatura zero. Encontra-se que tais sistemas apresentam dois tipos de processos de ordenamento, cujo tipo pode ser controlado através do ajuste das interações entre partículas, sendo que, uma forte repulsão inter-espécies leva ao ordenamento químico em termos de uma separação de fase, e uma fraca repulsão dá origem à cristalização espontânea, mantendo a homogeneidade química. Além disso, o comportamento do tipo dual parece ser universal para funções repulsivas de energia potencial em geral, com a propensão para o processo de cristalização sendo relacionada ao seu comportamento na vizinhança de separação zero.

Palavras-chave: Gelo - Propriedades mecânicas, Mecânica estatística de não-equilíbrio, Dinâmica molecular.

Abstract

Using atomistic simulation techniques, which can be considered as a method of "computational microscopy in situ", we study the mechanical properties of ice I_h by observing in detail the deformation mechanisms at atomic scales. As a second part of this Thesis, we also investigate through atomistic simulations, the nonequilibrium processes in repulsive binary mixtures.

Using molecular dynamics simulations, we assess the uniaxial deformation and nanoindentation response of ice I_h as described by two popular water models, namely, the all-atom TIP4P/Ice potential and the coarse-grained mW model. In particular, we investigate the response to both tensile and compressive uniaxial deformations along different crystallographic directions and temperatures. While the TIP4P/Ice model fails by either brittle cleavage under tension at low temperatures or large-scale amorphization/melting, the mW potential behaves in a much more ductile manner, displaying numerous cases in which stress relief involves the nucleation and subsequent activity of lattice dislocations. We study also the nanoindentation process on the basal plane, considering two different temperatures at which, respectively, a quasi-liquid layer (QLL) is or is not present. At very low temperatures, in the absence of a QLL, both potentials produce similar loading curves and deformation mechanisms. Close to the melting temperature, however, important differences were found, including deviations in the QLL thickness and fraction, as well as the presence of a competition between pressure-induced melting and recrystallization events. Nevertheless, both potentials exhibit similar deformation mechanisms and hardness estimates that are consistent with experimental data.

Secondly, we consider nonequilibrium processes for classical binary mixtures described by a set of different purely repulsive pair interaction potentials in which an infinite-temperature (ideal-gas) configuration is rapidly quenched to zero temperature. It is found that such systems display two kinds of ordering processes, the type of which can be controlled by tuning the interactions between unlike particles. While strong inter-species repulsion leads to chemical ordering in terms of an unmixing process, weak repulsion gives rise to spontaneous crystallization, maintaining chemical homogeneity. Furthermore, the dual-type behavior appears to be universal for repulsive pair-interaction potential- energy functions in general, with the propensity for the crystallization process being related to their behavior in the neighborhood of zero separation.

Keywords: Ice - Mechanical properties, Nonequilibrium statistical mechanics, Molecular dynamics.

Resumen

A partir del uso de técnicas de simulaciones atomísticas, que pueden ser consideradas como un método de "microscopia computacional in situ", estudiamos las propiedaded mecánicas del hielo I_h observando en detalle los mecanismos de deformación a escalas atómicas. Como segunda parte de esta Tesis, también investigamos através de simulaciones atomísticas, los procesos fuera del equilibrio en mezclas binarias repulsivas.

Usando simulaciones de dinámica molecular, evaluamos la deformación uniaxial y la respuesta a la nanoindentación del hielo I_h, descrita por dos modelos de agua populares, el potencial TIP4P/Ice y el modelo de agua monoatómica (mW). En particular, investigamos la respuesta a la deformación uniaxial de tracción y compresión a lo largo de direcciones cristalográficas y temperaturas diferentes. Mientras que el modelo TIP4P/Ice falla por ruptura frágil bajo tensión a bajas temperaturas o por amorfización/fusión a gran escala, el potencial mW se comporta mucho más dúctil, presentando numerosos casos en los que el alivio de tensiones implica nucleación y la actividad subsiguiente de dislocaciones en la estructura cristalina. También estudiamos el proceso de nanoindentación sobre el plano basal, considerando dos temperaturas diferentes en las que, respectivamente, una capa cuasi-líquida (QLL) está o no está presente. A temperaturas muy bajas, en ausencia de una QLL, ambos potenciales producen curvas de carga y mecanismos de deformación similares. Sin embargo, cerca de la temperatura de fusión se encontraron importantes diferencias, incluyendo desviaciones en el grosor y la fracción de la QLL, así como la presencia de una competencia entre los eventos de fusión y recristalización inducidos por presión. Sin embargo, ambos potenciales presentan mecanismos de deformación similares y estimaciones de dureza que concuerdan con los datos experimentales.

En la segunda parte, consideramos los procesos fuera del equilibrio de mezclas binarias clásicas descritas por un conjunto de diferentes potenciales de interacción de pares puramente repulsivos, en los que una configuración de temperatura infinita se enfría rápidamente hasta la temperatura cero. Se encuentra que esos sistemas presentan dos tipos de procesos de ordenamiento, cuyo tipo puede controlarse ajustando las interacciones entre las partículas, en donde una fuerte repulsión inter-especie conduce al ordenamiento químico en términos de una separación de fases, y una repulsión débil da origen a la cristalización espontánea, manteniendo la homogeneidad química. Además, el comportamiento de tipo dual parece ser universal para funciones de energía potencial repulsivas en general, y la propensión al proceso de cristalización está relacionada con su comportamiento en la vecindad de la separación cero.

Palabras-clave: Hielo - Propiedades mecánicas, Mecánica Estadística del no equilibrio, Dinámica molecular.

List of Figures

List of abbreviations and acronyms

MC Monte Carlo.

MD Molecular Dynamics.

DFT Density Functional Theory.

PBC Periodic Boundary Condition.

TIP4P Transferable Intermolecular Potential with 4 Points.

mW Monatomic Water.

LAMMPS Large-scale Atomic/Molecular Massively Parallel Simulator.

TEM Transmission Electron Microscopy.

NVE ensemble Microcanonical ensemble: The variables N (number of particles), V (volume) and E (total energy), influence the nature of the system's micro-states.

NVT ensemble Canonical ensemble: The variables N (number of particles), V (volume) and T (temperature), influence the nature of the system's internal states.

NPT ensemble Isothermal–Isobaric ensemble: Constant number of particles (N), constant pressure (P) and constant temperature (T) ensemble.

PPPM Particle-Particle/Particle-Mesh.

OVITO Open Visualization Tool.

DXA Dislocation Extraction Algorithm.

HB Hydrogen Bond.

AFM Atomic Force Microscopy.

QLL Quasi-Liquid Layer.

TIP5P/Ew Transferable Intermolecular Potential with 5 Points/ Ew refers to Ewald sums.

IDS Identify-Diamond-Structure.

FP Force-Penetration.

H Hardness.

$\mathbf{F}_N$ Normal Force.

PEL Potential Energy Landscape.

IS Inherent Structure.

CG Conjugate-Gradient.

UF Uhlenbeck-Ford.

IPL4 Inverse Fourth-Power Law.

IPL6 Inverse Sixth-Power Law.

WCA Weeks-Chandler-Andersen.

GC Gaussian-core.

LJ Lennard-Jones.

fcc Face-Centered-Cubic.

GSA Grain-Segmentation Algorithm.

MPD mean particle displacement.

Contents

Chapter 1

Introduction

1.1 Atomistic simulations

Numerical approaches, through computational simulations have been adopted in the last decades for the study of complex systems in several research areas of physics, astrophysics, chemistry, biology, engineering and even human sciences. Nowadays, computational physics has an important role in describing the phenomena of nature, where many physical systems are mathematically modeled by equations that cannot be solved analytically, or in which the number of physical variables to manipulate is very large, making it difficult to obtain a satisfactory approximation and a numerical treatment is necessary.

The computational methods to study complex systems are increasingly sophisticated and thanks to technological advances represented in processors with increasing speeds, parallelism and large memories with fast access, numerical simulation techniques based on statistical physics, developed for the treatment of systems of many bodies have become the most efficient. These techniques are known as atomistic simulations, [1] which allow the study of the movement of atoms in materials, and the collective behaviour of these atoms allows us to understand, for example, how a material undergoes deformation, phase transitions, among other phenomena.

These atomistic simulation techniques can be roughly divided into two

groups: The first corresponds to non deterministic simulations, based on Monte Carlo (MC) methods, which are linked to stochastic processes. These methods are based on random events, which allow a direct sampling of a probability distribution in an ensemble associated with equilibrium statistical mechanics, where physical observables can be calculated in terms of ensemble averages. [2, 3] The second corresponds to simulations of a deterministic character, using Molecular Dynamics (MD) techniques based on the integration of a set of classical Newton motion equations, compatible with a statistical ensemble associated with Boltzmann's statistical mechanics, where observables are determined as temporal averages over trajectories in phase space. [4–6]

The advances in computing allow that these atomistic simulations can be used to better understand the microscopic mechanisms underlying the observed physical phenomena. For example, molecular dynamics (MD) simulations are an extremely useful alternative avenue of investigation that can be considered as a method of "computational microscopy in situ", since they provide a detailed view of the mechanisms operating on atomic scales of length and time.

Thus, molecular dynamics (MD) simulations are widely applied to investigate the fundamental mechanisms that control, for example, the mechanical properties of materials, or the physical and chemical properties of biological systems. But to study these types of systems through the movement of atoms, it is necessary to represent reasonably well the interactions between them. Understanding the interaction of two particles through a classical interaction is relatively simple, but the interaction between a huge set of atoms and molecules is much more complex, and the more complex the interaction, the greater the number of calculations needed to obtain the trajectories.

A classical approach to perform the calculation of energy and forces as a function of time within an atomistic system makes use of interatomic potentials generally of a empirical character, which consist of an explicit functional form with parameters that are adjusted to reproduce reference values and properties of experimental character or from first principles by using quantum mechanical calculations. Another approach, where in principle, the calculations are more precise, is based on quantum-mechanical calculations of the electronic structure, also named Ab Initio Molecular Dynamics, such as density-functional theory (DFT). But this type of

simulation has a considerably higher computational cost, limiting to smaller systems and shorter times.

All results obtained in this Thesis were obtained through molecular dynamics (MD) simulations based on interatomic potentials of a empirical character.

1.2 Molecular dynamics

Molecular dynamics (MD) is a technique that seeks to determine the thermodynamic properties of many-body systems from the numerical integration of the classical equations of motion, where, from the definition of an interatomic potential $V(\mathbf{r}^N)$, it is possible to calculate the forces and potential energies as a function of time. Based on these results we can determine the trajectories in the phase space of each atom that composes the system and thus obtain the properties of interest (thermodynamic observables) from time averages over these trajectories.

In 1955, the first numerical approximations of nonlinear classical equations of motion were published by E. Fermi, et. al., [7]. Some years later, Alder and Wainwright developed the first DM simulations studying phase transitions in a system of rigid spheres. [8, 9] In 1964, Rahman was able to study the argon in the liquid phase through MD simulations, using the potential of Lennard-Jonnes and comparing calculations of properties of the system as the self-diffusion coefficient, with experimental results. [10] Later, in 1967, Verlet presented a more efficient algorithm for the integration of equations of motion studying the same system of Argon, building the diagram using the potential of Lennard-Jones. [11] Already in 1974, Stillinger and Rahman used MD simulations to study water in the liquid phase. [12]

To perform an MD simulation, we must define the geometry of the system under study, specifying the number of particles contained in a box of variable volume and shape. Likewise, the initial positions and velocities should be specified, to define the initial conditions necessary for the solution of the equations of motion. Furthermore, defining the potential of interaction between the particles is essential for the calculation of forces and establish the dynamics of the system. Other parameters such as temperature

and pressure can be defined as a function of the velocities (equipartition theorem) and the volume of the simulation box.

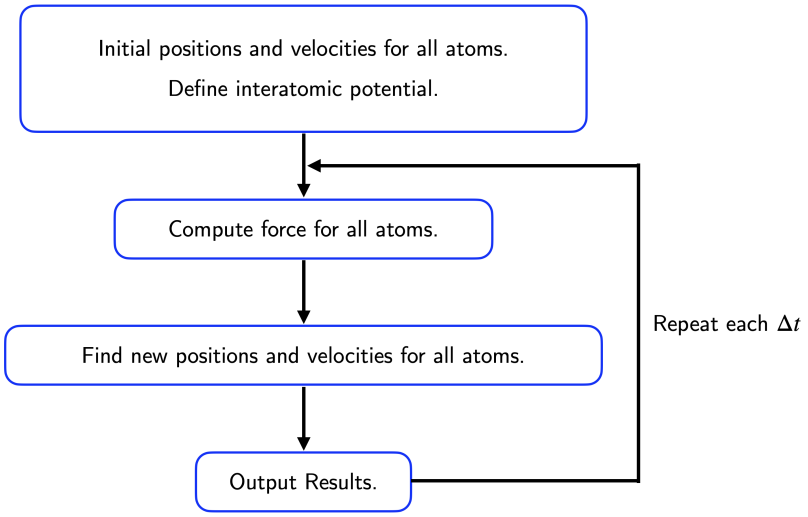

Figure 1.1: Simple flow diagram of the process of a molecular dynamics simulation.

The numerical solution of the equations of motion requires that time be discretized into time steps Δt, large enough that the differential equations of motion can be discretized and smaller in comparison with the period of highest vibrational frequency of the molecules in the system under study. Thus, by establishing the initial positions $\mathbf{r}_i^0$ and velocities $\mathbf{v}_i^0$ and defining an interaction potential $V(\mathbf{r}^N)$, we can determine the interaction forces for each particle $\mathbf{F} = -\nabla V(\mathbf{r}^N)$, and perform numerically this integration of the equations of motion to find the new positions and velocities after a step of time Δt. The trajectories of particles are determined from the calculation of forces and the integration of equations of motion in each step of time. A simple flow diagram of this process can be viewed in figure 1.1, and the optimization of this process are the basis of MD.

1.2.1 Interatomic potentials

As discussed above, an MD simulation requires the definition of a potential function, explicit usually referred to as a force field or an interatomic potential. Working with an functional form of potential energy is advantageous because it allows one to determine the force from the gradient of this potential.

Most of these potentials are empirical and contain free parameters that are adjusted to reproduce reference values and properties of experimental character or from first-principles quantum mechanical calculations, as mentioned previously. The functional form of these potentials is associated with bonded forces (chemical bonds) and non-bonded forces (van der Waals forces and electrostatic charges).

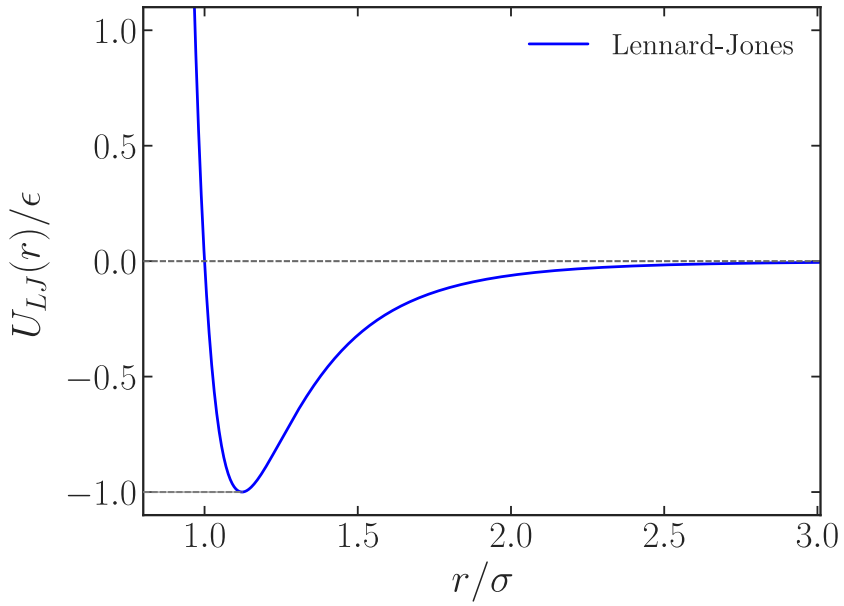

Figure 1.2: Graph of Lennard-Jones potential. The potential energy U is zero when $r = \sigma$ and the minimum potential energy has the value $U = -\epsilon$.

There are ways to simplify these types of interatomic potentials, one of them being to represent the non-bonded forces through pairwise potentials. A well-known example is the Lennard Jones (LJ) potential, used for describing van der Waals forces,

$$U(r) = 4\epsilon \left[\left(\frac{\sigma}{r} \right)^{12} - \left(\frac{\sigma}{r} \right)^{6} \right], \tag{1.2.1}$$

where r is the distance between the particles, σ is the distance for which the potential energy is zero (also used to define the size of the particles) and ϵ corresponds to the depth of the potential well, that is, the minimum potential energy has the value $U = -\epsilon$. This potential has a positive and a negative term, so that it describes very well the interaction of two atoms, where they repel each other at short distances, attract each other when the distance is moderate and the interaction tends to zero for much greater distances, as observed in figure 1.2.

In addition to pairwise potentials, there are also other types of potentials that often better describe the forces of chemical bonds. This type of potentials called bond-order potentials, describe interaction as the combination of two and three-body interactions,

$$U = \sum_i \sum_{i>i} \phi_2(r_{ij}) + \sum_i \sum_{i \neq j} \sum_{k>j} \phi_3(r_{ij}, r_{ik}, \theta_{ijk}), \tag{1.2.2}$$

where θ_{ijk} is the bond angle subtended by the bonds r_{ij} and r_{ik} at vertex i. Thus, the strength of chemical bonds depends on their local bonding environment, considering the number of bonds, the angles and bond lengths. An example of this type of potential is the potential of Stillinger-Weber, whose functional form we will show in the next subsection, which describes very well the interactions in solid and liquid forms of Si. [13]

Another way to further simplify the description of the interactions is to use "pseudo-atoms" to represent groups of atoms. These types of models are known as coarse-grained models, allowing to perform MD simulations on very large systems. Soft-matter materials such as polymers and colloids are studied with this type of models. In particular, repulsive pair potentials, which are very useful in this type of systems, are studied in this Thesis.

1.2.2 Water models

The representation of atomistic interactions through models does not generally fully describe the properties of a system. Accordingly, some models better represent thermodynamic quantities or system behaviours than others. In the last decades, for example, a plethora of empirical water models have been developed.

The empirical models for the case of water must take into account the geometry of the structure, such as covalent bonds, electrostatic interactions and Van-der-Waals interactions. The characteristics that define such models are the number of electrostatic interaction sites, whether the molecules are rigid or flexible and whether polarization is possible.

The rigid models are considered to be the simplest all-atom water models and rely on non-bonded interactions. In such models, bonding interactions are implicitly treated by holonomic constraints, with OH bond lengths and HOH bond angles being fixed. The electrostatic interaction is modeled using Coulomb's law, and the dispersion and repulsion forces using the LJ potential. For example, a four-site model like the TIP4P/Ice (Transferable Intermolecular Potential with 4 Points) is a popular water model that has been used to describe solid phases of water, describes very well the melting properties, provides a well overall phase diagram and efficiently predicts the densities of various forms of ice and liquid water. [14] This model has four interaction points including a dummy atom near the oxygen along the bisector of the HOH angle. The dummy atom only has a negative charge, without mass, and improves the electrostatic distribution around the water molecule. The model is described by an interatomic potential of the form:

$$U_{ab} = \frac{A}{r_{oo}^{12}} - \frac{B}{r_{oo}^{6}} + \sum_{i}^{a}\sum_{j}^{b}\frac{k_C q_i q_j}{r_{ij}}, \tag{1.2.3}$$

where U_{ab} corresponds to the potential energy of molecules a and b, k_C, the electrostatic constant, q_i and q_j are the partial charges in the sites i and j within the molecule; r_{ij} is the distance between two charge sites and A and B are the Lennard-Jones parameters (applying only to the interaction between the oxygen atoms.)

On the other hand, a coarse-grained model that shows a reasonable description of water at a much lower computational cost is the mW model, which describes the water molecule as an effective single particle (monoatomic water). [15] It is an adaptation of Stillinger and Weber's potential for silicon [13], explicitly disregarding the protons as well as long-range electrostatic interactions.

The model is given by a bond-order function:

$$U = \sum_{i}\sum_{i>i}\phi_2(r_{ij}) + \sum_{i}\sum_{i\neq j}\sum_{k>j}\phi_3(r_{ij}, r_{ik}, \theta_{ijk}), \tag{1.2.4}$$

where

$$\phi_2(r) = A\epsilon \left[B \left(\frac{\sigma}{r} \right)^p - \left(\frac{\sigma}{r} \right)^q \right] \exp\left(\frac{\sigma}{r - a\sigma} \right), \tag{1.2.5}$$

and

$$\phi_3(r, s, \theta) = \lambda\epsilon \left[\cos\theta - \cos\theta_0 \right] \exp\left(\frac{\gamma\sigma}{r - a\sigma} \right) \exp\left(\frac{\gamma\sigma}{s - a\sigma} \right), \tag{1.2.6}$$

where, $A = 7.049556277$, $B = 0.6022245584$, $p = 4$ $q = 0$, $\epsilon = 6.189$ Kcal/mol, $\sigma = 2.3925$ Å and $\gamma = 1.2$ give the form and scale to the potential; $a = 1.8$ is the reduced cutoff; and $\theta = 109.47$ and $\lambda = 23.15$ favor tetrahedral angles. Even if this model considers only short-range interactions, it faithfully reproduces ice and liquid water structure, density and phase transitions with great precision at a much lower computational cost. [15]

Comparing these two models, an all-atom and a coarse-grained model, is one objective of this Thesis, in particular with regard to the mechanical response of ice I_h.

1.2.3 Boundary Conditions

When we want to study the bulk properties of a given substance, surface effects in MD simulations can be mitigated by imposing periodic boundary conditions (PBC). A set of identical images of the simulation box in all directions can be imagined, so that when a i particle leaves the simulation box, a particle of the image box enters from the opposite side as shown in the figure 1.3. When we want to study the surface properties, these PBC in other directions are useful to avoid the border effects.

Based on these periodic conditions, each particle can interact with all other particles, even at the edges through the image particles, and the force would be incalculable for a large number of particles. However, in general, the intensity of the potential interaction decreases rapidly with increasing distance. Thus, we can study a short-range interaction, defined through a spherical truncation, where interactions at

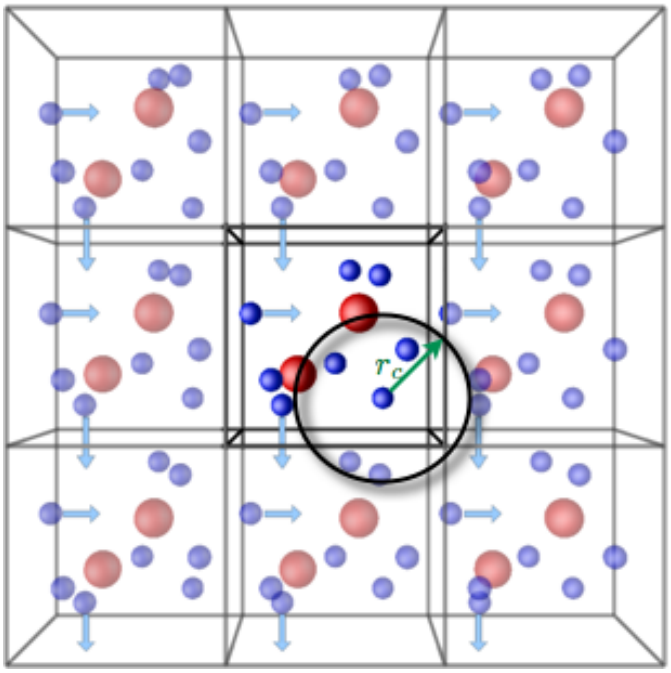

Figure 1.3: Schematic representation of the PBC and the cutting radius r_c in a MD simulation. (modified figure from the ISAACS program website) [16])

distances greater than a certain r_c cutting radius are disregarded, and this cutting radius should be smaller than half the length of the simulation box. Thus, the force acting on each particle will be calculated as the sum of the forces exerted by each of the neighboring particles within the cutoff radius. However, when long-range interactions such as charge-charge interactions between ions and dipole-dipole interactions between molecules are involved, special techniques such as the Particle–Particle Particle–Mesh (PPPM) method are required. [17]

1.2.4 Integration of equations of motion

Having defined the interatomic potential and the initial conditions of the system, the next step is to determine the dynamics of the system from the numerical integration of the classical equations of motion, given from Newton's second law as follows:

$$\frac{d^2\mathbf{r}_i(t)}{dt^2} = \frac{1}{m_i}\mathbf{F}_i(t) = -\frac{1}{m_i}\frac{\partial V(\mathbf{r}^N)}{\partial \mathbf{r}_i}. \tag{1.2.7}$$

This set of equations can also be written as a set of first order coupled equations:

$$\begin{aligned} \frac{d\mathbf{r}_i(t)}{dt} &= \mathbf{v}_i(t) \\ \frac{d\mathbf{v}_i(t)}{dt} &= \frac{\mathbf{F}_i(t)}{m_i}, \end{aligned} \tag{1.2.8}$$

or in an equivalent form, from the Hamiltonian formalism of classical mechanics: [18]

$$\begin{aligned} \frac{d\mathbf{r}_i(t)}{dt} &= \frac{\partial H(\mathbf{r}^N, \mathbf{p}^N)}{\partial \mathbf{p}_i} \\ \frac{d\mathbf{p}_i(t)}{dt} &= -\frac{\partial H(\mathbf{r}^N, \mathbf{p}^N)}{\partial \mathbf{r}_i}, \end{aligned} \tag{1.2.9}$$

where $\mathbf{r}_i(t)$ and $\mathbf{p}_i(t)$ are respectively the position and the conjugate momentum for the i-th particle. Thus, integrating these equations of motion we can deterministically calculate a $6N$-dimensional microstate of the system $\{\mathbf{r}^N(t), \mathbf{p}^N(t)\}$ from an initial microstate $\{\mathbf{r}^N(0), \mathbf{p}^N(0)\}$.

One of the key points in the construction of a MD simulation, besides a good choice of the Δt time step, is to implement an efficient integration algorithm, which satisfies criteria such as: speed of integration, conservation of the amplitude of movement (which indicates the veracity of the trajectories, because any small error in the numerical integration of the equations of motion, will blow up exponentially) and conservation of the energy of the system. The latter depends on two properties that present the equations of motion: the temporal reversibility (the equations remain unchanged under the exchange of $t \to -t$ and $\mathbf{p} \to -\mathbf{p}$) and the fact that a volume $d\Gamma$ of the phase space is constant under canonical transformations (Liouville's theorem). [18] The algorithms that satisfy these properties are called symplectic algorithms.

The first symplectic algorithm was the one proposed by Verlet in 1967. [11] A few years later, in 1982, Swope, et. al., [19] introduced a more efficient version of this algorithm known as *velocity-Verlet* which is still widely used today.

More generally, from Liouville's formulation of classical mechanics [3, 4], the position and momentum for each time step $t + \Delta t$, are determined through the following

scheme:

1. $\mathbf{p}(t+\frac{\Delta t}{2}) = \mathbf{p}(t) + \mathbf{F}(t)\frac{\Delta t}{2}$
2. $\mathbf{r}(t+\Delta t) = \mathbf{r}(t) + \frac{\mathbf{p}(t+\frac{\Delta t}{2})}{m}\Delta t$
3. Compute $\mathbf{F}(t+\Delta t)$ from $\mathbf{r}(t+\Delta t)$
4. $\mathbf{p}(t+\Delta t) = \mathbf{p}(t+\frac{\Delta t}{2}) + \mathbf{F}(t+\Delta t)\frac{\Delta t}{2}$,

where position and velocity are determined for each time step in two steps, calculating the force in an intermediate step. First, the velocity is calculated for half a time step $(t + \Delta t/2)$ and the new position for a time step $(t + \Delta t)$, then the force is calculated for time step $(t + \Delta t)$, and finally the velocity at time $(t + \Delta t)$ is calculated.

This algorithm allows us to determine a set of microstates $\{\mathbf{r}^N(t), \mathbf{p}^N(t)\}$ with energy, volume and number of particles remaining constant, which in terms of statistical mechanics is called ensemble NVE or *microcanonical ensemble*. [1] However in practice, if we want to carry out a simulation under conditions of fixed temperature and/or fixed pressure through a *canonical ensemble* NVT or an *isobaric-isothermic ensemble* NPT, the equations of motion need to be reformulated. From the point of view of statistical mechanics, we can impose a temperature by setting the system in contact with a thermal bath that exchanges heat with it, which in MD simulations is called a thermostat, or a barostat in case of imposing a pressure through dynamic shape change (volume is a variable in the simulation).

An example of a widely used thermostat, including in this Thesis, is the Langevin thermostat, where the probability densities of position and momentum sample the Boltzmann canonical distribution correctly. The idea of the Langevin thermostat is to consider the Brownian motion of macroscopic particles immersed in a fluid of fictitious microscopic particles. Following Langevin's formalism, the equations of motion for each of the macroscopic particles are:

$$\begin{aligned} \frac{d\mathbf{r}_i(t)}{dt} &= \frac{\mathbf{p}_i(t)}{m_i} \\ \frac{d\mathbf{p}_i(t)}{dt} &= \mathbf{F}_i(t) - \gamma\mathbf{p}_i(t) + \mathbf{R}_i(t), \end{aligned} \tag{1.2.10}$$

where γ is a friction coefficient that represents a damping viscosity due to the fictitious particles of the thermal bath, and $\mathbf{R}_i$ is a random force acting on the i-th particle, arising from collisions with the fictitious particles. [20]. This random force has two properties, dictated by the fluctuation-dissipation theorem;

$$\begin{aligned} \langle R_{i\alpha}(t)\rangle &= 0 \\ \langle R_{i\alpha}(t)R_{i\beta}(t')\rangle &= 2m_i K_B T\gamma\delta(t-t'). \end{aligned} \tag{1.2.11}$$

In the same way that the *velocity-Verlet* algorithm is implemented to determine the temporal evolution of the system, from the formalism of Liouville the following scheme is obtained for the integration of the Langevin equations [21]:

1. $\mathbf{p}(t+\frac{\Delta t}{4}) = e^{-\gamma\Delta t/2}\mathbf{p}(t) + \sqrt{(1-e^{-\gamma\Delta t})mk_BT}\mathbf{R}$
2. $\mathbf{p}(t+\frac{\Delta t}{2}) = \mathbf{p}(t+\frac{\Delta t}{4}) + \mathbf{F}(t)\frac{\Delta t}{2}$
3. $\mathbf{r}(t+\Delta t) = \mathbf{r}(t) + \frac{\mathbf{p}(t+\frac{\Delta t}{2})}{m}\Delta t$
4. Computed $\mathbf{F}(t+\Delta t)$ from $\mathbf{r}(t+\Delta t)$
5. $\mathbf{p}(t+\frac{3\Delta t}{4}) = \mathbf{p}(t+\frac{\Delta t}{2}) + \mathbf{F}(t+\Delta t)\frac{\Delta t}{2}$
6. $\mathbf{p}(t+\Delta t) = e^{-\gamma\Delta t/2}\mathbf{p}(t+\frac{3\Delta t}{4}) + \sqrt{(1-e^{-\gamma\Delta t})mk_BT}\mathbf{R}'$,

where the scheme is applied to each of the particles in the system. $\mathbf{R}$ and $\mathbf{R}'$ are two independent random Gaussian values, with probability densities:

$$\rho(R) = \frac{1}{\sqrt{2\pi\sigma}}\exp\left(-\frac{|R|^2}{2\sigma^2}\right), \tag{1.2.12}$$

with $\sigma^2 = 2\gamma m_i k/_B T$.

1.2.5 Thermodynamic observables

MD simulations provide the positions and velocities of the system atoms at each step of time, i.e., the set of microstates $\mathbf{\Gamma(t)} = \{\mathbf{r}^N(t), \mathbf{p}^N(t)\}$ that describes the

trajectories in phase space. From these microstates and the formulation of statistical mechanics, we can determine the macroscopic thermodynamic observables (physical quantities) of the system. In this sense, we can determine the expected value of a thermodynamic observable $\mathcal{A}$ as an *ensemble* average, according to the form:

$$\frac{\mathcal{A}}{N} = \lim_{N,V\to\infty} \frac{\langle \mathcal{A}(\mathbf{\Gamma}) \rangle}{N} = \lim_{N,V\to\infty} \frac{1}{N} \int \rho(\mathbf{\Gamma}) \mathcal{A}(\mathbf{\Gamma}) d\mathbf{\Gamma}, \tag{1.2.13}$$

where V/N remains constant, $\mathcal{A}(\mathbf{\Gamma})$ is the observable that depends on the microstates of the system Γ, and $\rho(\mathbf{\Gamma})$ is the probability density of a statistical ensemble compatible with the thermodynamic conditions of the system.

The ensemble average $\langle \mathcal{A}(\mathbf{\Gamma}) \rangle$ cannot be determined directly through a MD simulation. Although if we consider valid the Ergodic hypothesis [22], which postulates that for simulation times large enough, the dynamics of the system will cover all accessible states of the phase space; we can say that the ensemble averages are equivalent to the time averages over trajectories in the phase space, such that:

$$\begin{aligned} \langle \mathcal{A}(\mathbf{\Gamma}) \rangle &= \overline{\mathcal{A}(\mathbf{\Gamma})} \\ &= \lim_{t_{sim}\to\infty} \frac{1}{t_{sim}} \int_o^{t_{sim}} \mathcal{A}[\mathbf{\Gamma}(t)] dt \approx \frac{1}{M} \sum_i \mathcal{A}[\mathbf{\Gamma}(t)], \end{aligned} \tag{1.2.14}$$

where, $\mathcal{A}[\mathbf{\Gamma}(t)]$ corresponds to the instantaneous value of the observable $\mathcal{A}$ for the set of M configurations $\mathbf{\Gamma}(t) = \{\mathbf{r}^N(t), \mathbf{p}^N(t)\}$, with $0 < t < t_{sim}$, sampled at time intervals longer than the system correlation time.

1.3 The importance of ice as a material

At this point we have seen in a general way the bases of the atomistic simulations, and we mentioned the existence of several models to represent the atomic interactions of liquid water and ice, presenting two of the most popular that will be studied in this thesis. But what is the importance of studying water and especially ice? Well, water is the most abundant substance on the planet and we can find it naturally

in the three states of matter: solid, liquid and gaseous. Most of the liquid water is found in the oceans covering the 70% of the Earth's surface, also our body is composed by approximately 65% of liquid water and the water suitable for human consumption (fresh water), is mostly found in the solid state in the polar ice sheets in Antarctica and in the high mountain regions. Solid water is also seen in the form of snow and in the atmosphere as a gas, and the presence in the air is fundamental for breathing. Ice is also present on other planets, moons and comets in our Solar System.

Although water is composed of an apparently simple molecule, water is a very complex substance, it presents some properties that are unusual, such as the high melting and boiling point (thanks to this we can easily find it in the 3 states), the high thermal capacity (thanks to this we maintain the thermal balance on the planet and in our body), presents anomalies in density, in the solid state is less dense than in the liquid state and crystallizes in at least 19 different crystalline forms. [23] The figure 1.4 shows the solid-liquid phase diagram and some of its phases, here we will focus on the phase known as hexagonal ice I_h, which is the only phase we can find naturally on Earth.

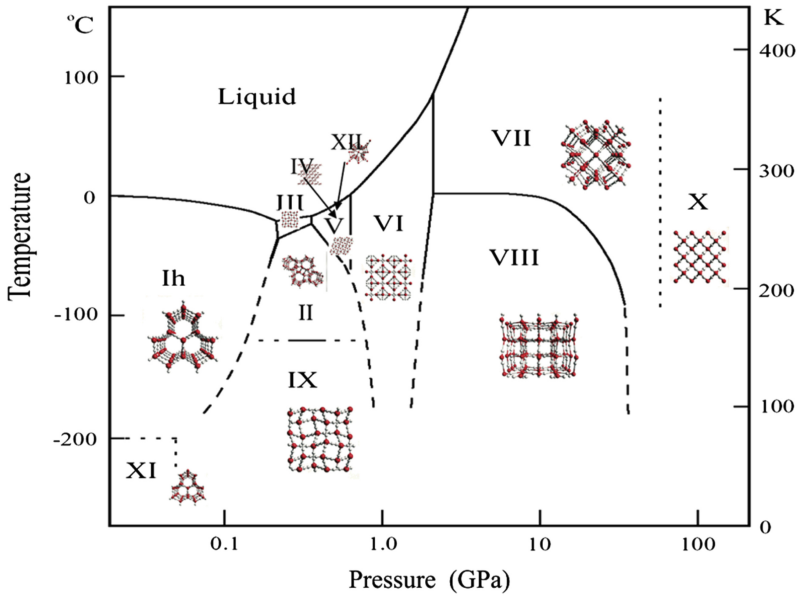

Figure 1.4: The solid-liquid phase diagram of ice (the solid-liquid-gas triple point and liquid-gas coexistence line lie off the diagram to the left). [24]

Ice and its properties are very important in biological and climatic processes. For example in winter it is common to observe the freezing of rivers and lakes, because the ice is less dense than liquid water, the formation of ice occurs on the surface, acting

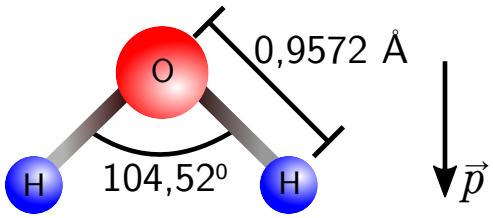

Figure 1.5: Illustration of the isolated water molecule, indicating the distance O-H, the angle H-O-H and the direction of the simple dipole formed by the three point charges.

as a thermal insulator (the environment can be at $-40°$C, the water below does not go down from 0°C). On the other hand, the snow not only reflects the 90% of ultraviolet radiation, in Antarctica and high mountain regions accumulates without melting and is converted into ice layers that increase more and more forming the known glaciers that can be up to almost 4 km high and due to the high pressures by its own weight the ice flows in a malleable way. These glaciers are important in the dynamics of the climate and it is important to know their dynamics.

The daily experience told us that the ice is a brittle material, for example if we throw an ice cube on the ground, it will break into several pieces, but on wide scales like in glaciers due to the high pressures the ice flows in a malleable way. A better understanding of ice structures, patterns and processes is therefore a current topic of research in physics, as the molecular mechanisms behind these processes are not yet well understood.

Each of the crystalline phases of ice presents a different crystalline structure, where protons may or may not be ordered. This variety of phases is due in part to the shape of the electronic structure of the isolated water molecule, composed of two atoms of H and one of O, as shown in the figure 1.5. The bonds between O and H are covalent and due to the distribution of charges, the molecule has an electric dipole moment in the direction of this bisector angle. The distance O-H is 0.9572(3) Å and the angle H-O-H is 104.52(5)°, obtained experimentally by spectrometry. [25]

1.3.1 The crystalline structure of Ice I_h

The water molecular has an electronic distribution so that the two hydrogen atoms share electrons with the oxygen atom. However, there are two other electron pairs

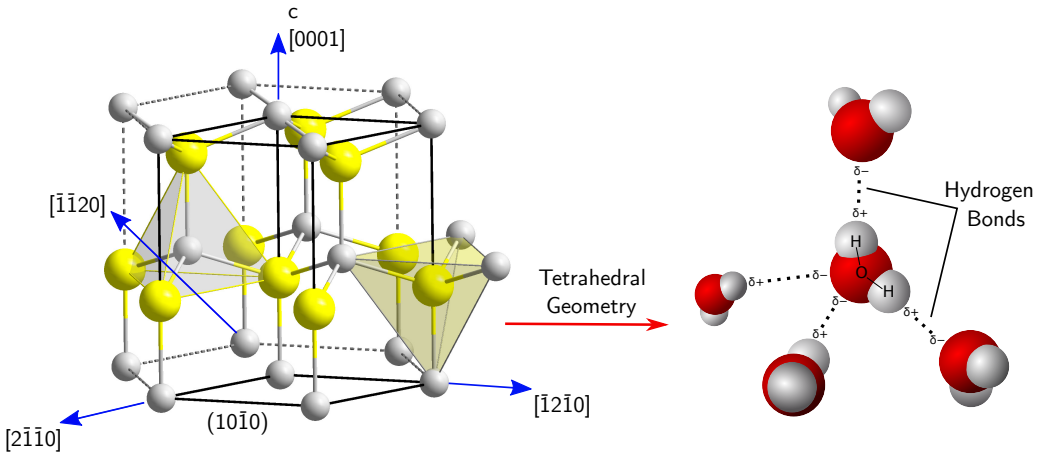

Figure 1.6: Representation of the crystalline structure of the mineral ZnS, also known as wurtzita. In the ice the Oxygen occupies the sites of a hexagonal Wurtzite lattice. The last molecular orbital contributes to the formation of pairs of isolated electrons that bond with the Hydrogen of the neighboring molecules forming a tetrahedral pattern. [26]

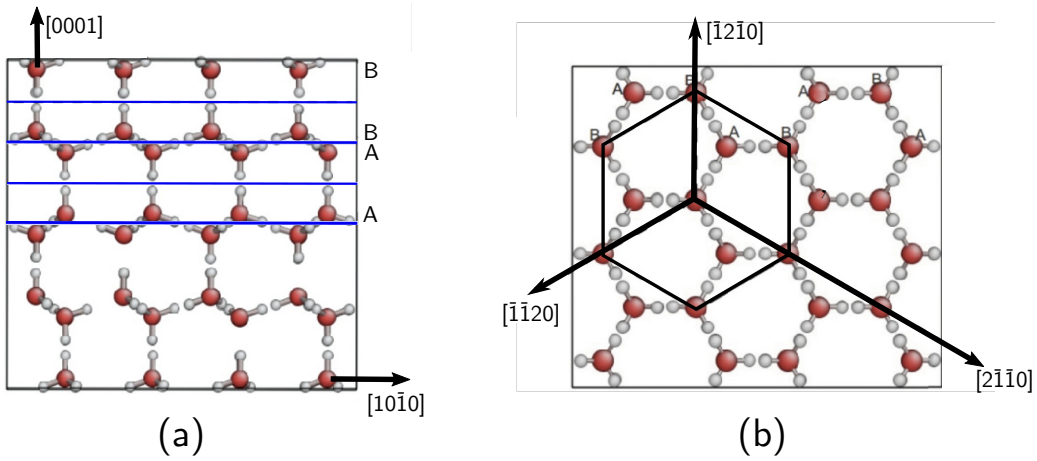

Figure 1.7: (a) Ice I_h Wurtzite structure projected on a $11\bar{2}0$ plane, with the c axis running vertically. Oxygen ions are arranged in a double-layer sequence of the type $\cdots$AABB$\cdots$. (b) Ice Ih structure projected on a (0001) plane depicting positions of layers A and B. [27]

of the oxygen atom that do not participate in the covalent bond, also called lone pairs. Thus, the “v" shape of the molecule is due to the fact that the nuclei of the hydrogen atoms are in excess of positive charge and repel each other. On the other hand, the connection between two water molecules is through an attraction between a proton donor molecule (of hydrogen) and a proton receptor molecule (in oxygen), or also known as hydrogen bond.

In the ice I_h structure, as shown in the figure 1.6, each molecule of water has four hydrogen bonds, in which it donates two protons and receives two protons, in such

way that each molecule is bonded to another four molecules forming a tetrahedral pattern. The oxygen atoms occupies the sites of a hexagonal Wurtzite lattice. The name is due to the mineral ZnS, the zinc sulfide represented in wurtzite lattice of the figure, but in this context both the gray and yellow atoms correspond to oxygen atoms. Given its hexagonal character, the Wurtzite ice Ih structure can be seen as a stacking of (0001) layers along the c axis. The figure 1.7 shows the projection of the structure in the basal and prismatic planes, where it is possible to see a sequence of hexagonal stacks and oxygen atoms are arranged in a double-layer sequence of the type $\cdots$AABB$\cdots$.

Another aspect of the ice I_h structure is that only the oxygen follows this tetrahedral pattern shown above and there is no ordering in the orientation of the molecules (it is proton disordered) and therefore, following the symmetry of the structure there are 6 possible orientations of the molecules, all with equal probability (figura 1.8). This proton disorder, over the hydrogen sites in the structure, satisfies the two ice rules, also known as Bernal-Fowler's ice rules: [28, 29]

1) There are two hydrogen which are covalently bonded to each oxygen.
2) The oxygen in each molecule of water forms two hydrogen bonds with other oxygen atoms, so there is exactly one hydrogen between each pair of oxygen atoms.

Violations of these rules produce particular defects, also called Bjerrum defects. [30] But in this work we will work with perfect ice structures.

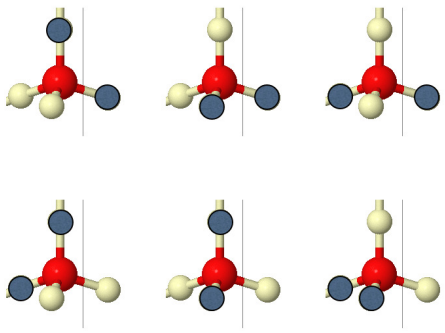

Figure 1.8: The six possible orientations of the water molecule in a certain site on the crystal ice lattice.. [26]

Through high resolution neutron diffraction techniques, experimental values of the molecular geometry of ice I_h were obtained by Kuhs and Lehmann in 1983. [31] For temperatures of 60 K and 223 K, the value of the average distance between the neighboring

oxygen is $2,748(1)$ Å and $2,760(1)$ Å respectively.For the same temperature values, the average distance of covalent bonds is $1,743(2)$ Å and $1,758(3)$ Å, and the value of the angle O'-O-O' is $109,32(2)^\circ$ and $109,58(4)^\circ$ respectively, which are very close to the ideal tetrahedral angle $109,47(4)^\circ$.

Other interesting aspects about the crystal structure of ice and some experimental and computational challenges will be discussed in chapters 2 and 3.

1.4 Objectives

In the previous sections, we discussed the basics of atomistic simulations, specifically focusing on molecular dynamics, and how this technique can be applied in the study of several phenomena, as well as the importance of representing interactions through an interatomic potential. In this context, this Thesis presents two main objectives, which, although distinct, find a common point in the fact that interatomic potentials play an essential role in these studies.

To understand the microscopic processes that control the mechanical deformation of materials, atomistic simulations have proven to be an extremely useful tool in recent years. However, even though there are several interatomic potentials that reproduce a good description of water in different phases, the mechanical response of the many water models developed over the last decades is essentially unknown. Therefore, one of the objectives of this Thesis is to contribute to the microscopic understanding of the mechanical behavior of ice by investigating the mechanical response of ice I_h using two of the most popular water models. On the one hand, we investigate the explicit-proton TIP4P/Ice model, which has been used to describe the solid phases of water, and on the other we consider the coarse-grained mW model that describes the water molecule as a single particle. Specifically, we intend to investigate how the explicit representation of hydrogen atoms affects the mechanical behavior of ice.

In the same way, classical systems described by repulsive pair potentials, are useful descriptions for interactions in soft-condensed-matter systems. Equilibrium phase behavior of such models has been the subject of many studies in last decades using

atomistic simulations. Non-equilibrium phenomena, on the other hand, have received much less attention. Therefore, the other objective of this Thesis is to study the processes that display spontaneous development of structure from an initially disordered state for these repulsive binary systems.

In Chapter 2 we will present the study of the behavior of ice systems subjected to uniaxial deformation, both tensile and compressive in nature, investigating the respective mechanisms of failure for TIP4P/ice and mW models. In chapter 3 we will present the study of the response to mechanical indentation by a nanometer-scale tip of the ice I_h basal-plane surface.

In chapter 4 we will show that symmetric binary mixtures described by a variety of purely repulsive pairwise interactions display two kinds of ordering processes, an unmixing process and a spontaneous development of crystalline order, forming a polycrystalline solid of uniform composition, composed of grains with the rock-salt (B1) structure. Finally, in chapther 5 we will expose the conclusions of this Thesis and future perspectives.

Chapter 2

Uniaxial deformation behavior of Ice I_h

This chapter was reproduced from [P. A. Santos-Flórez, C. J. Ruestes, and M. de Koning, J. Chem. Phys. 149, 164711 (2018)], with the permission of AIP Publishing.

2.1 Introduction

The mechanical properties of water ice play a central role in a wide variety of phenomena in such different fields as glaciology, climatology, materials science and engineering, and take place on vastly different time and length scales. [23, 32, 33] For example, the flow of glaciers and ice sheets, which takes place on time and length scales of years and kilometers, respectively, is directly involved in the slow dynamics of Earth's global climate system. On the other hand, the high-velocity impact of pieces of ice with ice-breaker ships, bridge pillars and aircraft parts involve processes that occur on time and length scales of seconds and meters, and affect the integrity of such man-made engineering structures.

While there are at least 19 crystalline and 3 amorphous forms in its phase diagram, [23] under the thermodynamic conditions on Earth the proton-disordered hexagonal ice I_h is the only relevant crystalline form of water. Yet, this single phase

displays an astonishing richness in its mechanical properties. Not only can ice I_h behave as a brittle solid, as one usually observes in daily experience, it can also deform in a ductile manner by flowing along basal planes, depending on factors such as deformation rate and temperature. [34] In fact, Glen and Perutz [35] verified experimentally that, under the application of low stresses ($\sim$ 0.1-0.5 MPa), strains of up to 600% could be reached without apparent macroscopic failure.

The mechanical characteristics of ice have become the focus of substantial research efforts over the past decades.[35–51] Most of these have been experimental in character, focusing mainly on the phenomenological aspects of the deformation behaviors. Much less is known, however, about the molecular-scale processes that underlie these behaviors. For instance, except for insight into the molecular structure of partial dislocations on the basal plane from first-principles calculations on ice I_h, [27] not even the basic molecular-scale mechanism for their motion in ice is understood. While X-ray topography permits the visualization of extended defects and their motion in ice on the scale of millimeters [52–55], an experimental technique that offers nano-scale visualization – such as that provided by *in situ* transmission electron microscopy (TEM) for the case of metals, [56] – remains unavailable.

In this context, atomistic-level simulation has proven an extremely useful alternative route of investigation. It constitutes a method for *in situ* computational "microscopy", [57] which provides detailed insight into the unit mechanisms that operate on atomic length and time scales. For this reason, such simulations are commonplace in physics, chemistry, and materials science and they have been applied innumerous times to investigate the fundamental mechanisms that control the mechanical properties of crystalline and amorphous solids.[58, 59] Water ice, however, has been a notable exception. Although countless simulations have focused on various aspects of the condensed phases of water, including their structural, dielectric, thermodynamic and kinetic properties,[14, 15, 60–83], the mechanical behavior of ice, with the exception of two recent studies concerning methane hydrates [84] and shock Hugoniots, [85] has remained largely out of scope. Indeed, the development process of molecular models by itself, with the objective of proposing interatomic potentials that improve the description of the behaviors of water across different phases, [79] has for the most part

neglected the mechanical properties of crystalline and amorphous phases of water. This implies that the mechanical response of the many water models developed over the past decades are essentially unknown.

In this chapter, we investigate mechanical response of ice I_h for two of the most popular water models that have been used to describe solid phases of water, namely the all-atom TIP4P/Ice model [14, 61, 64, 78, 80–82] and the coarse-grained mW potential. [15, 67, 70–72, 83] The former is a reparametrization of the original TIP4P model [86] with the objective of improving the description of ice phases. The mW model, on the other hand, is an adaptation of Stillinger and Weber's silicon potential [13] with the intent of modeling the interactions between water molecules without explicitly considering the protons and the long-range electrostatic interactions. In particular, we focus on the behavior of the systems subjected to uniaxial deformation, both tensile and compressive in nature, investigating the respective mechanisms of failure. In particular, the specific dependence of the failure mode on parameters such as deformation rate and temperature, is indicative of intrinsic brittle or ductile behavior and thus of interest in the context of characterizing the mechanical response of both water models for ice I_h.

2.2 Computational approach

2.2.1 Generation of Computational Cells

The majority of the simulations were carried out using a periodic cell containing 12800 water molecules, with spatial dimensions $16 \times 10 \times 10$ in units of the a, b and c directions of the conventional orthogonal unit cell containing 8 molecules. [87] To assess possible cell-size effects, a smaller number of simulations was executed using a $36 \times 18 \times 18$ cell containing 93312 molecules. Both cells represent fully proton-disordered realizations of a defect-free I_h structure with zero total dipole moment. They were generated as follows. First, we generate the positions of the oxygen atoms, placing them on the sites of the Wurtzite lattice. Next, we attach two protons to each of them to form water molecules. But given the proton-disordered nature of ice I_h, this must be done randomly, but subject to the constraint imposed by the second

Bernal-Fowler ice rule which requires that there be precisely one proton between each nearest-neighbor pair of oxygen atoms. [23] For a periodic, defect-free ice I_h cell this can be achieved using the approach of Rahman and Stillinger. [88] Their approach amounts to mapping the assignment of molecular orientations onto the problem of generating a 3-dimensional *directed* graph in which each node is connected to four neighbors arranged according to the Wurtzite lattice, with precisely two ingoing and two outgoing links. In this network picture, the nodes represent the oxygen atoms, and the two outgoing links of each node correspond to the two protons that are covalently bonded to it in the water molecule. To generate such a directed graph we start with its *undirected* counterpart and search for a cyclic decomposition using a series of random walks. After finding such a cyclic decomposition, the generated directed network is composed of a set of closed paths in which, by construction, each link of the network has been traversed exactly once, with each node having precisely two incoming and two outgoing links. If the cyclic decomposition has a non-zero total dipole moment due to closed paths that cross the periodic boundary conditions, [88] it may be possible to eliminate it by inverting the direction of a number of them. If this is not possible, we repeat the procedure starting from the original undirected graph until a cell with zero total dipole moment is obtained. Only for the 93312-molecule cell did we need two runs to find a zero-dipole-moment configuration.

2.2.2 Simulation protocols

All simulations have been carried out using molecular dynamics techniques as implemented in the `LAMMPS` package. [89] In all cases, prior to deformation, the ice I_h cells were equilibrated at zero pressure and the desired temperature. We consider 3 temperatures for each water model, namely 50 K and 200 K for both of them, and a third value ~ 5 K below their respective melting temperatures, giving 264 and 269 K, respectively, for the TIP4P/Ice and mW models. Equilibration was achieved by running simulations within an anisotropic zero-pressure isobaric-isothermal NPT ensemble in which all three sides of the orthogonal cell are allowed to vary independently. The corresponding equations of motion are based on a Parrinello-Rahman-type barostat [90–92] and a Langevin thermostat [93].

For the TIP4P/Ice all-atom model, bond lengths and angles are held fixed using the `SHAKE` algorithm, [94] and the long-range electrostatics is handled employing the particle-particle particle-mesh (PPPM) scheme. [17] The equations of motion are integrated using a time step of $\Delta t = 0.5$ fs and the damping time scales for the thermostat and barostat were chosen as $\tau_T = 0.2$ ps and $\tau_p = 2$ ps, respectively. Compared to the TIP4P/Ice model, the only difference for the mW model is the integration time step, chosen at $\Delta t = 1$ fs. Of course, the `SHAKE` and PPPM methods are unnecessary to begin with for the charge-neutral atomic mW model.

After the initial equilibration, the computational cells are isothermally deformed under controlled conditions of strain rate, adopting a protocol similar to that employed by Wu *et al.* in their investigation of the mechanical stability of methane hydrates. [48] Specifically, we apply uniaxial deformations by uniformly rescaling the position components along the axis of deformation at each step. This rescaling is carried out in the spirit of the $NL_dP_1P_2T$ ensemble, in which L_d is the length of the cell along the deformation direction and P_1 and P_2 are the transverse pressure components. In all the deformation simulations L_d varies with time according to $L_d(t) = L_{d0}(1 + \dot{\varepsilon}\, t)$, with $\dot{\varepsilon}$ the strain rate and L_{d0} the initial length deformation axis, while maintaining $P_1 = P_2 = 0$ throughout the entire deformation simulation. This allows expansion or contraction of the transverse directions of the cell associated with the Poisson effect during compressive or tensile uniaxial deformations. Even though the employed strain rates are substantially higher than those used in typical laboratory experiments, the obtained results provide valuable insight into the intrinsic mechanical behavior of the two water models.

In all considered cases, different realizations of the same deformation process were not found to display significant quantitative nor qualitative differences. Accordingly, all stress-strain curves reported below correspond to the results obtained from single deformation simulations, without ensemble averaging.

Furthermore, for all considered deformation rates, the maximum attained strain values in the simulations for the mW model have been chosen to be approximately twice as large as those for the TIP4P/Ice model. As will become clear in the following, this choice is motivated by the distinct mechanical response for both models. Whereas

the failure mode for the TIP4P/Ice model is characterized by a single deformation event, the response of the mW model often displays a succession of further occurrences after the first yield drop, giving rise to strongly non-monotonic behavior of the stress-strain curves up to substantially larger strain values. To explore this behavior, the deformation simulations involving the mW model cover time intervals that are roughly twice as long as those for the TIP4P/Ice model for a given strain rate.

2.3 Results and Discussion

2.3.1 Tensile deformation

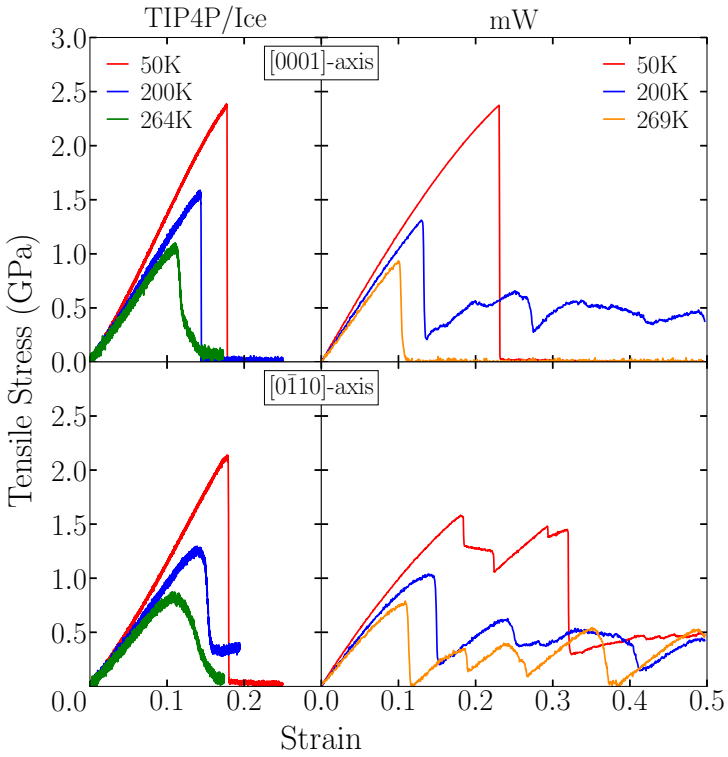

Figure 2.1: Stress - strain curves for the tensile deformation at strain rate of 5×10^7 s^{-1} along the c-axis and the [0$\bar{1}$10] axis for TIP4P/Ice and mW models for the 12800-molecule cell at different temperatures.

We first consider the results obtained for in the simulations in which the computational cells were subjected to uniaxial tensile deformation. The top row of Fig. 2.1 presents the stress-strain response for tensile deformations along the [0001] axis on the 12800-molecule cell, comparing the two water models at temperatures varying

between 50 K and the vicinity of the melting point, at a strain rate $\dot{\varepsilon} = 5 \times 10^7$ s^{-1}. For small strains all systems display the expected linear elastic behavior. In particular, the TIP4P/Ice model features a Young's modulus starting at 11 GPa at 50K and decreasing to 10 GPa as temperature increases to 264 K. For the mW model the values decrease from 11.5 GPa at 50K to 9 GPa at 269K. Both models are consistent with experimental data, [95] which give values decreasing from $\sim$ 12.8 GPa at 200 K to $\sim$ 11.8 GPa at 257 K.

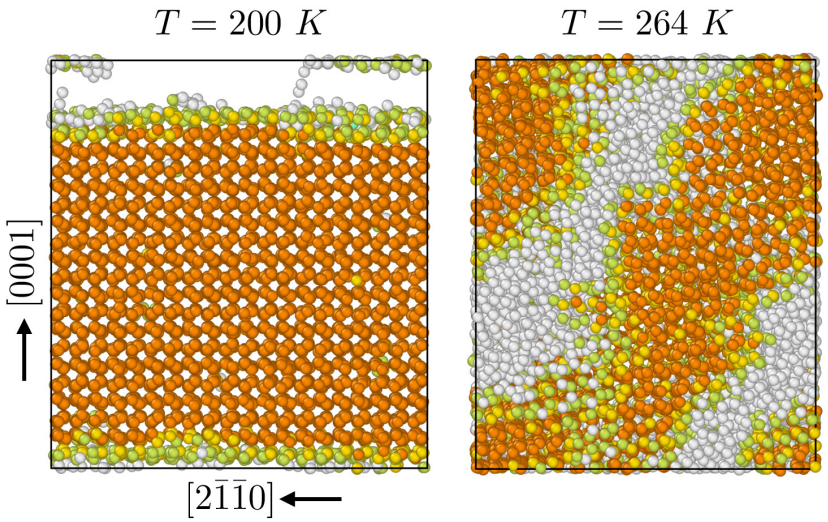

Figure 2.2: Typical failure modes in tensile tests along the c axis for the TIP4P/Ice model and the 12800-molecule cell at a strain rate of 5×10^7 s^{-1}. Colors of particles indicate different crystal symmetries as identified by OVITO : Wurtzite (orange), Wurtzite first neighbor (yellow), Wurtzite second neighbor (green). White particles belong to disordered regions. Brittle failure through cleavage at 0.15 strain and $T = 200\ K$ and partial stress relief due to the formation of a liquid region at 0.15 and 264 K.

For strains of the order of 0.10 the elastic response becomes nonlinear, closely followed by a yield point. As expected, both the critical strain as well as the stress at the yield point decrease with increasing temperature.

To characterize the mode of failure, we visualize structures along the deformation process using the `Identify-diamond-structure` [96] algorithm incorporated into the `OVITO` package. [97] It distinguishes between cubic and hexagonal-diamond structures by analyzing the arrangement of the second-nearest neighbors of a given oxygen atom. Full details can be found in Ref. [96].

Typical results for the TIP4P/Ice model are shown in Fig. 2.2. At $T = 50\ K$ and $T = 200\ K$, the failure is brittle in nature, characterized by complete cleavage along

the basal plane. At 264 K, which is 5 K below the melting temperature T_m, failure no longer involves cleavage and stress relief is achieved by partial melting.

Considering the failure mechanisms of mW model, at 50 K the response displays the same brittle cleavage seen for the TIP4P/Ice model. For the higher temperatures, however, the yield drop is achieved by a different mechanism. This is exemplified in particular by the behavior at $T = 200$ K. Instead of a complete stress relief, there is only a partial drop at the yield point, followed by a renewed stress build-up upon further straining. Inspection of the atomic configurations around the yield drop reveals that the incomplete stress relief is achieved by a plastic deformation event involving the nucleation of a dislocation dipole. This is visualized in Fig. 2.3, where the two thick lines represent the dislocation cores as obtained using the `DXA` algorithm [98] in `OVITO` and the red arrows describe their respective opposite Burgers vectors. They are of the $\frac{1}{6}[0\bar{2}23]$ type, which form imperfect dislocations combining the Burgers vectors of an in-basal-plane Shockley partial and an out-of-basal-plane imperfect dislocation with Burgers vectors of $\frac{1}{3}[0\bar{1}10]$ and $\frac{1}{2}[0001]$ types, respectively. [99, 100] The dislocations are predominantly of edge character, and at the stage shown in the picture the formation of the dipole is almost complete, with both dislocations still touching each other in the center. Since the in-basal-plane component

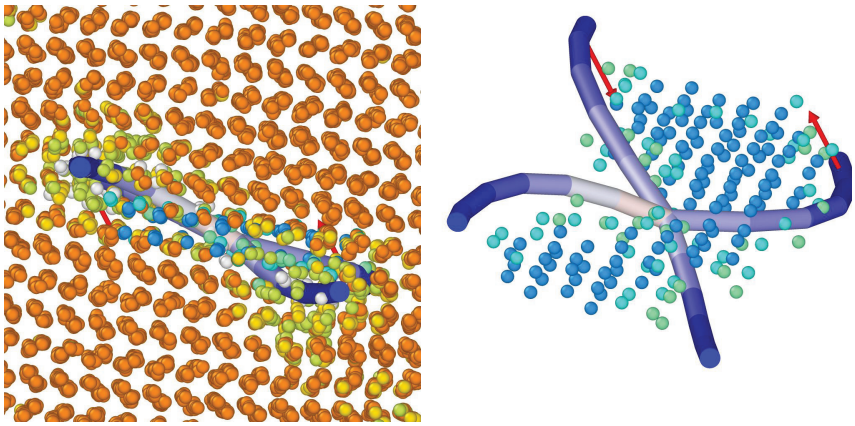

Figure 2.3: Atomistic configurations during tensile deformation along the [0001] axis for the mW model and the 12800-molecule cell at 200 K and a strain of 0.193. Thick lines depict dislocation lines of opposite Burgers vectors shown as red arrows. Left part shows view along the $[0\bar{1}10]$ direction. Right panel only displays the oxygen atoms in the stacking fault area (blue spheres) and the dislocations that delimit its bounds. Both dislocations still touch near the center of the image. Coloring of dislocation indicates its character, with blue and red representing edge and screw character, respectively.

of the opposing Burgers vectors corresponds precisely to that of a Shockley partial, both dislocations bound a stacking-fault area shown by the atoms in blue. Upon further straining the two dislocations of the dipole fully detach, resulting in two almost straight dislocations along the $[0\bar{1}10]$ directions enclosing a rectangular area of stacking fault. Finally, at the highest temperature of 269 K, which is $\sim 5\,K$ below the melting temperature for the mW model, the yield drop is accompanied by complete melting.

To assess possible anisotropies in the response, we repeat the same deformation simulations, but now applying tensile strain along the $[0\bar{1}10]$-axis. The resulting stress-strain response for the 12800-molecule cell and both water models are displayed in the second row of Fig. 2.1. For the TIP4P/Ice model the response curves are qualitatively similar to their c-axis counterparts for all temperatures, displaying a regular elastic rise followed by a single yield drop. In quantitative terms, compared to deformation along the c-axis, the yield stress for the TIP4P/Ice model is $\sim$ 0.1-0.2 GPa lower. At $T = 50\ K$ the yield drop is caused by complete cleavage, while at the higher temperatures stress relief is achieved by the appearance of disordered/melted areas across the system and rotations of the remaining crystalline regions.

The mW model, on the other hand, behaves very differently. At 50 K, for instance, for which the c-axis response displays the usual rise followed by a single yield drop, as shown in Fig. 2.2, the tensile stress develops a non-monotonic response. It is characterized by a sequence of two rises separated by partial drops. Inspection of atomistic configurations along these sequences reveals that, instead of a yield drop, the system first passes through a structural phase transition before the onset of plastic deformation. This is shown in Fig. 2.4, which depicts atomic snapshots along the straining process. Between strains of $\sim$ 0.20 and $\sim$ 0.25 the system undergoes a phase transition to a different crystalline phase, followed by a stress drop close to $\sim$ 0.30, where the cell has returned to a deformed Wurtzite structure accompanied by amorphous regions. The other crystalline phase that appears during the straining process retains a hexagonal structure, as is evident from the snapshot at the strain value of 0.25 in Fig. 2.4. In fact, this crystalline phase has the structure of a strained layered Honeycomb lattice in which the chair-like puckered hexagonal rings [23] of the ice I_h lattice have become planar, lying perpendicular to the c-axis. The stacking of the graphene-like layers is such that the hexagons of subsequent

layers are shifted relative to each other along the $[2\bar{1}\bar{1}0]$ direction by ~ 0.27 Å, as shown in Fig. 2.5. The structure maintains the four-fold coordination of the oxygens, but the angles between pairs of bonds are severely distorted compared to a tetrahedral arrangement. In particular, the angle between the out-of-plane bond and the in-plane bond varies between 88° and 90°. For the same reason, the layered honeycomb structure also does not seem to be related to the cubic ice I_c phase previously observed in the mW model.[83] Like ice I_h, cubic ice features puckered hexagonal rings, with the only difference being their boat-like arrangement compared to the armchair conformation in ice I_h.

To the best of our knowledge, this phase has not been observed in water and it is likely to be an artifact of the mW model.

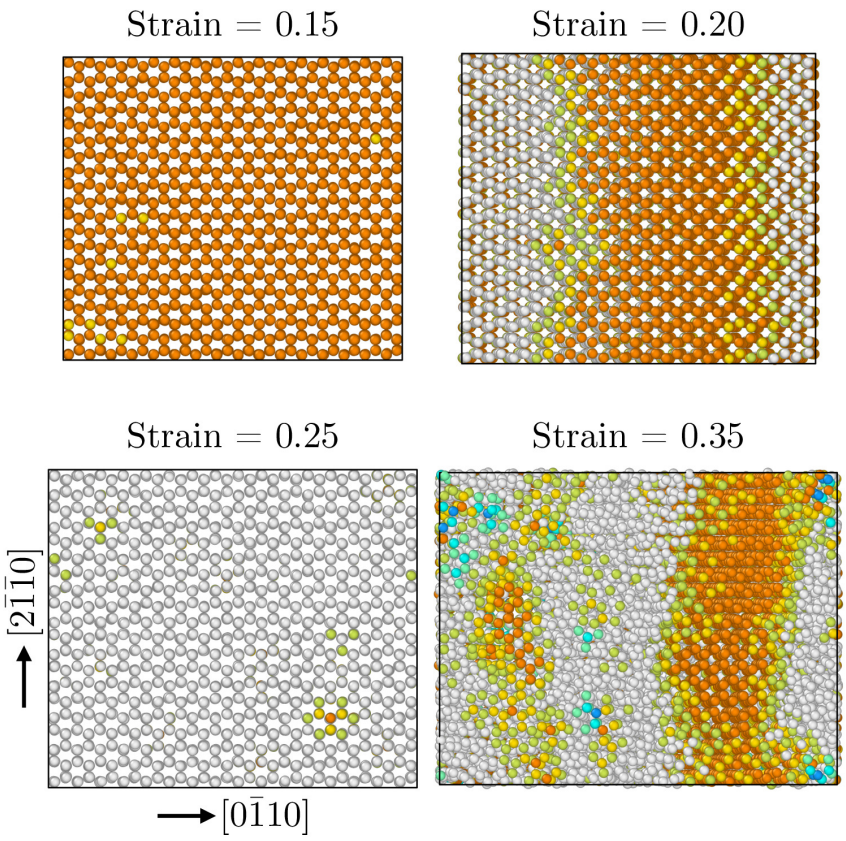

Figure 2.4: Typical atomistic configurations during tensile deformation along the $[0\bar{1}10]$ axis for the mW model and the 12800-molecule cell at 50 K. Crystalline phase reached at a strain of 0.25 corresponds to layered Honeycomb structure.

For 200 K and 269 K the phase transition does not take place and the yield drops in the stress-strain curves are associated with dislocation activity. For instance, the first yield drop at 269 K is associated with the nucleation of a dipole of perfect edge dislocations with Burgers vectors of the type $\frac{1}{3}[\bar{2}110]$ and their line directions along

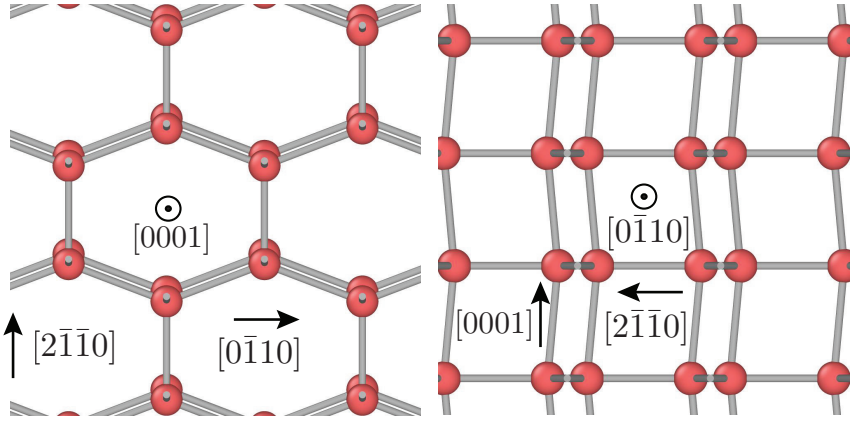

Figure 2.5: Crystal structure of layered Honeycomb phase strained along [0$\bar{1}$10] direction. Bonds connect nearest neighbors. Left panel shows view along the c-axis. Two shown graphene-like sheets are subsequent layers along the c-axis. Their relative in-plane displacement is $\sim$ 0.27 Å in the [2$\bar{1}\bar{1}$0] direction. Right panel depicts view along the [0$\bar{1}$10] direction. Relative shifts of subsequent layers give rise to zig-zag-like structure along the c-axis.

the [0001] axis, as pictured in Fig. 2.6. The subsequent saw-tooth-like evolution of the stress-strain curve upon further straining involves a number of dislocation-related events, including dipole annihilation and re-nucleation.

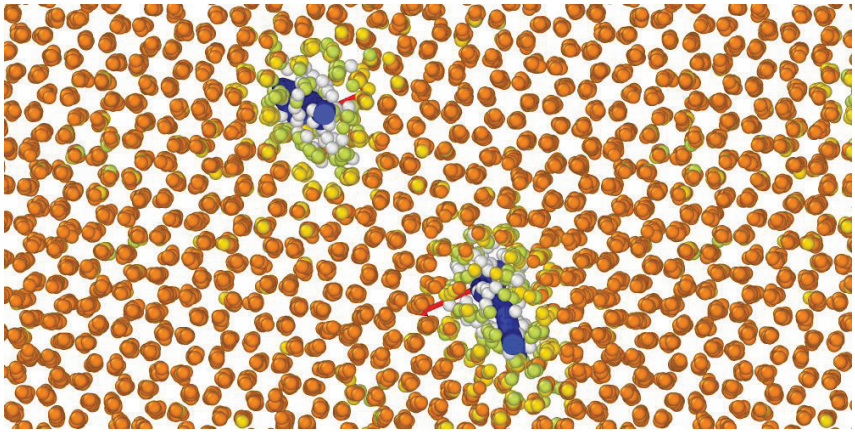

Figure 2.6: Atomistic configuration viewed along the [0001] axis during tensile deformation along the [0$\bar{1}$10] axis (vertical direction in the figure) for the mW model at 269 K and a strain of 0.138. Thick lines depict dislocation lines of opposite Burgers vectors shown as red arrows.

2.3.2 Compressive deformation

Next, we explore the response of the systems under compressive uniaxial deformation. The top row of Fig. 2.7 presents the stress-strain response for compressive

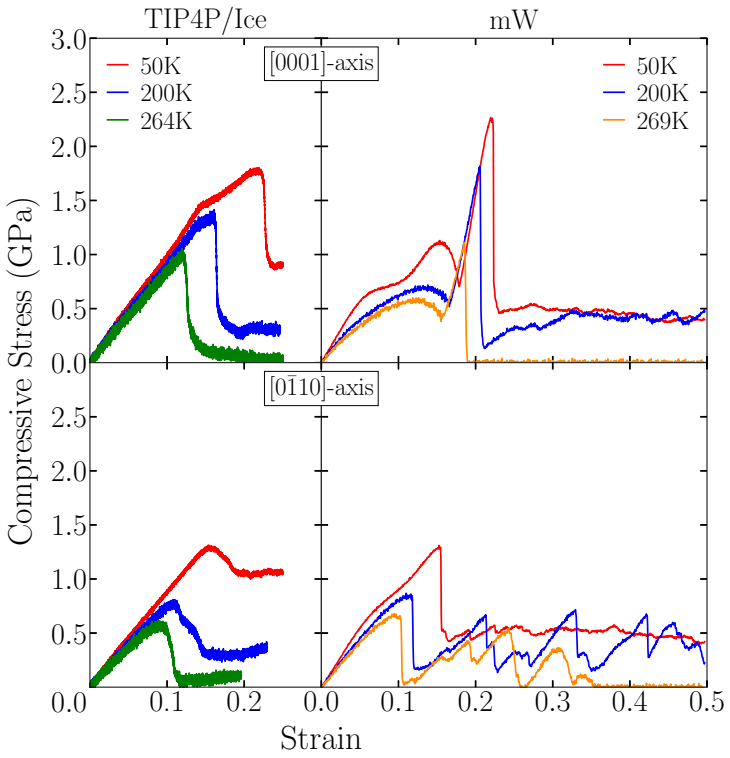

Figure 2.7: Stress - strain curves for the compressive deformation at strain rate of 5×10^7 s^{-1} along the c-axis and the [0$\bar{1}$10] axis for TIP4P/Ice and mW models for the 12800-molecule cell at different temperatures.

deformation along the [0001]-axis on the 12800-molecule cell, comparing the two water models at the same temperatures and strain rate as those considered for the tensile deformations. Again, for small strains, all systems display linear elastic behavior with Young's moduli consistent with the values reported in the preceding section. Notably, for the TIP4P/Ice model at 50 K, the elastic response suddenly changes slope as the compressive strain exceeds 0.13. Inspection of the atomic structure shows that this sudden change of slope in the stress-strain curve can be attributed to a distortion in the alignment of the O-O nearest-neigbor network as exemplified in Fig. 2.8. This distorted structure continues to respond elastically until reaching the yield point close to a strain of ~ 0.22, after which the stress is partially relieved in a manner similar to that seen in the tensile deformations, with the appearance of large-scale disordering as well as substantial deformation and rotations of the remaining crystalline regions. At 200 K and 264 K, the yield points occur at smaller deformations and the low-temperature distorted structure no longer appears. The stress-relief mechanisms, on the other hand, are basically the same, although at 264 K the disordered regions are manifestly liquid in nature, displaying substantial diffusion.

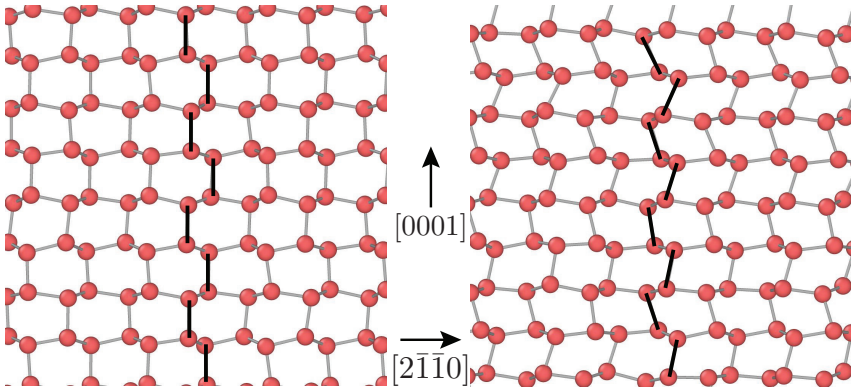

Figure 2.8: Excerpt of the crystal structure of TIP4P/Ice model at 50 K compressed along [0001] direction. Hydrogen atoms not shown for clarity. Grey lines connect nearest-neighbor oxygen pairs. Left and right panel show views below and above 0.13 strain, respectively. The oxygen-oxygen nearest-neighbor pairs that are aligned along the c axis below 0.13 strain develop into a zig-zag pattern, as highlighted by the thick black lines.

For the mW model, although the elastic moduli at the initial stages of deformation are quantitatively similar to those of the tensile deformation test, the compressive elastic response is much more non-linear in the strain interval between $\sim$ 0.05 and $\sim$ 0.18. Surprisingly, further increasing the deformation gives rise to a second, mostly linear, elastic regime regardless of temperature. Inspection of the atomistic structure reveals that the sudden change into a steep second linear elastic regime is due to the same phase transition to the layered honeycomb structure shown in Fig. 2.5, in which the buckled hexagons in the Wurtzite structure become planar, here under the influence of the compressive stress along the c-axis. Finally, at a strain in the range between 0.2 - 0.22, a marked single yield drop occurs. While at 269 K the drop involves complete melting, for the lower two temperatures stress relief is achieved by substantial disordering combined with appreciable deformation and rotations of the remaining crystalline regions.

The bottom row of Fig. 2.7 depicts the stress-strain responses for compressive uniaxial deformation along the [0$\bar{1}$10] direction. As for the tensile deformation case, the anisotropy of the response for the TIP4P/Ice model is only modest. While the values of the yield stresses for compression along the [0$\bar{1}$10] axis are somewhat lower in comparison to those for the [0001] direction, the failure mechanisms are the same. For the mW model, on the other hand, the response is again strongly anisotropic, with stress-strain curves that are qualitatively very distinct for both compression directions. For 200 K and 269 K,

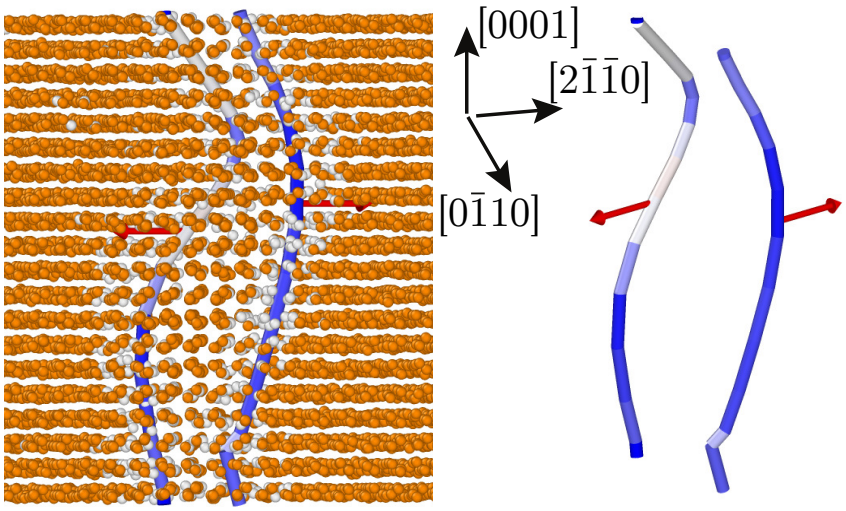

Figure 2.9: Atomistic configurations during compressive deformation along the [0$\bar{1}$10] axis for the mW model and the 12800-molecule cell at 200 K and a strain of 0.25. Thick lines depict a dislocation dipole, of opposite Burgers vectors shown as red arrows, that are immersed in the atomistic structure. Left part shows view along the [0$\bar{1}$10] direction. Right panel only displays a perspective view of the dislocation dipole, Burgers vectors correspond to the $\frac{1}{3}$[1$\bar{2}$10] direction. Coloring of dislocation indicates its character, with blue and red representing edge and screw character, respectively.

they display similar saw-tooth-like behavior as that observed for the tensile deformations. The origin of the serrated curves is again due to dislocation activity, as visualized in Fig. 2.9. The two thick lines again represent the dislocation cores as obtained using the `DXA` algorithm [98] in `OVITO` and the red arrows describe their respective opposite Burgers vectors. They are of the $\frac{1}{3}$[1$\bar{2}$10] type, which form perfect dislocations [100] and they are predominantly of edge character.

2.3.3 Influence of cell size and strain rate

To assess the extent to which the size of the used computational cell affects the obtained results, we repeat the tensile and compressive simulations using the larger cell containing 93312 molecules at the same strain rate of $\dot{\varepsilon} = 5 \times 10^7$ s^{-1}. We find that the cell size does not fundamentally alter the results for both models, neither under tensile nor compressive deformation. This is illustrated in Fig. 2.10 which compares the compressive stress-strain curves for both cell sizes, with the results for the large cell depicted using dashed lines. The values of the yield stresses and strains for the two models are essentially unaffected and the failure modes are also the same. In particular, for the

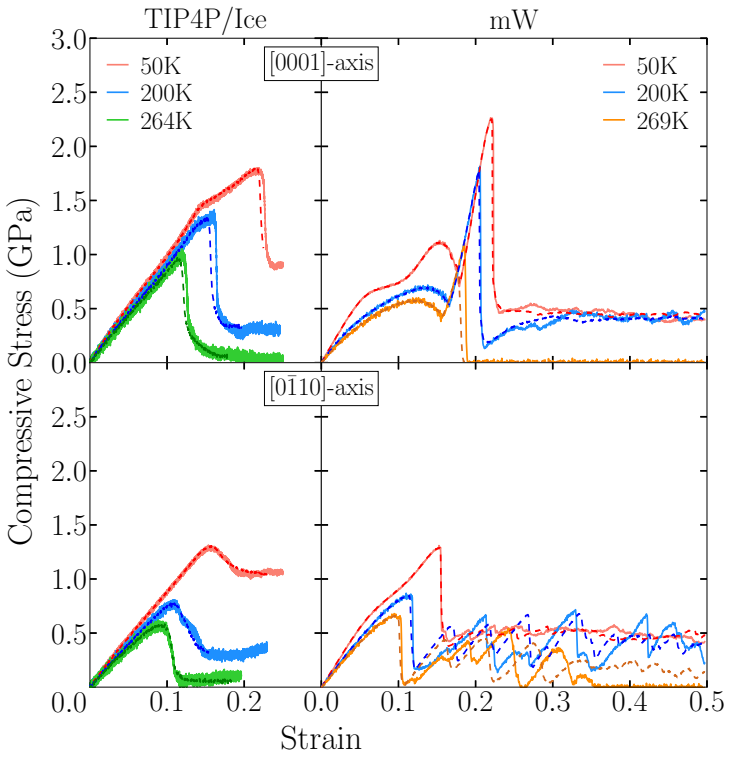

Figure 2.10: Sample size influence on the stress - strain curves for compressive deformation at a strain rate of 5×10^7 s^{-1} and a variety of temperatures. Full and dashed lines represent data for 12800 and 93312-molecule cells, respectively.

mW model the deformation simulations display the same serrated character associated with dislocation activity and features the same phase transition from the Wurtzite to the layered Honeycomb structure.

We also investigated the effect of the applied strain rate on the obtained results. First we carried out a number of deformation simulations at a strain rate of 5×10^8 s^{-1}, an order of magnitude larger than that used to obtain the results described in the previous sections. This increase does not give rise to fundamentally different mechanisms of stress relief for neither of the models. For the mW model we were also able to execute deformation simulations at a strain rate an order of magnitude lower, at 5×10^6 s^{-1}. Again, the mW model displays the same behavior, showing both brittle cleavage in tension for the lowest temperatures as well as dislocation activity for higher temperatures. Due to the elevated computational cost associated with the long-range electrostatics, it has not been possible to carry out deformation simulations for the TIP4P/Ice model at a strain rate lower than 5×10^7 s^{-1}.

2.3.4 Discussion

The results presented in the previous sections clearly demonstrate the fundamentally different mechanical responses of both water models. For the all-atom TIP4P/Ice model, with the exception for low-temperature tensile brittle cleavage, the main mechanism for uniaxial stress relief is large-scale amorphization or melting. The coarse-grained mW model, on the other hand, in addition to also failing by brittle cleavage at low temperatures, uniaxial failure occurs mainly by the usual plastic deformation mechanism involving nucleation and motion of lattice dislocations. In this sense, the mW model may be regarded as more ductile compared to TIP4P/Ice.

Indeed, the fact that mW behaves in such a malleable manner even at strain rates that are substantially higher than those applied in typical experiments indicates that the mW description of ice I_h is much too ductile. Uniaxial deformations carried out in the laboratory [101] have shown that single-crystal ice I_h deforms in a brittle manner already at strain rates $\sim 10^{-2}$ s^{-1}, which is 7-8 orders of magnitude slower than the deformation rates used in our simulations.

An interesting issue concerns the origin of the very different behaviors of TIP4P/Ice and mW. In addition to the very distinct functional forms describing cohesion, a key difference between them is the absence of explicit protons in the mW model. This means that the description of the hydrogen bond (HB) in the mW model does not capture its fundamental asymmetry, with one molecule donating a proton while the other acts as acceptor. While disregarding the HB asymmetry does not seem to prevent the model from correctly reproducing several thermodynamic properties of water and ice, [15] it may preclude it from capturing the essence of kinetic processes that involve the breaking and reformation of HBs.

A particular example of such a process in ice I_h involves the formation and motion of dislocations. A key element of the ice I_h structure is its proton-disordered character and, as analyzed in detail by Glen [23, 102], this randomness acts as an obstacle to both the formation as well as the movement of dislocations. This is so because when two molecular planes are initially bonded by randomly oriented HBs, shearing one plane

with respect to the other will inevitably lead to mismatching hydrogen-bond conditions, for instance having two proton donor or acceptor molecules instead having a pair with one of each. This implies that after breaking a HB under shear, its reformation may not be topologically possible without additional molecular rotations, hampering the shearing process. The fact that the proton disorder is absent within the mW description is therefore a substantial facilitating ingredient in both the nucleation and motion of dislocations, inadvertently enhancing the model's malleability.

2.4 Summary

In summary, we have used molecular dynamics simulations to investigate the uniaxial-deformation response of ice I_h as described by the all-atom TIP4P/Ice potential and the coarse-grained mW model. Considering tensile and compressive uniaxial deformations along the [0001] and [$0\bar{1}10$] crystallographic directions for a series of different temperatures, we classify the respective failure mechanisms and assess their sensitivity to strain rate and cell size. The TIP4P/Ice model fails by either brittle cleavage under tension at low temperatures or large-scale amorphization/melting at higher temperatures. The mW potential, on the other hand, behaves in a much more ductile manner, displaying numerous cases in which stress relief is achieved by the nucleation and subsequent activity of lattice dislocations. In fact, given that mW behaves in such a malleable manner even at strain rates that are substantially higher than those applied in typical experiments indicates that the mW description of ice I_h is overly ductile. A possible factor in this enhanced malleability is the absence of explicit protons in the mW model, disregarding the fundamental asymmetry of the hydrogen bond that plays an important role in the nucleation and motion of lattice dislocations in ice I_h.

Chapter 3

Nanoindentation of Ice I_h

3.1 Introduction

Nanoindentation [103, 104] is an experimental technique that probes mechanical properties of a material by pressing a nanometer-scale tip with known mechanical properties into it. Its most common use being elastic modulus and hardness determination in materials,[105] it has proved useful in a wide range of problems in materials science, such as the study of creep, [106] cracking mechanisms in brittle thin films, [107] fracture toughness and adhesion assessment on dielectric thin films, [108] strain hardening and recovery in bulk metallic glasses, [109] phase transformations,[110] and even for the study of biological tissues. [111]

Recently, nanoindentation techniques have also been used for "non - technological" materials such as water ice. [112, 113] In particular, atomic force microscopy (AFM) has been employed to probe the ice-vapor surface for the presence of a quasi-liquid layer (QLL), [114] which is of the utmost importance in several contexts, including glacier flow, environmental processes in clouds, ice adhesion to man-made

structures and even in winter sports. These AFM studies [115–119] focused on various aspects of the QLL; Döppenschmidt and co-workers first performed measurements of its thickness and explored its growth with temperature,[115] after which they assessed the role of impurities, [116] showing an increase in thickness with the addition of monovalent salt. Butt *et al.* [117] analyzed plastic deformation after their AFM curves, estimating yield strength and investigating the role of the indentation speed and melting rate. They suggested that the liquidlike interfacial layer would be squeezed out by the indenter. Pittenger *et al.* [118], in turn, do suggest the presence of a QLL at the interface between tip and ice. They also reported an increase in QLL thickness with increasing temperature. More recently, however, Constantin *et al.* [119] performed AFM studies with different temperature gradients and tip chemistry, reporting QLLs thicknesses that are much smaller than those seen in previous AFM studies.

These contradicting findings reveal the difficulty with which the interpretation of such experiments is often met. In this scenario, atomistic simulation techniques can often offer complementary insight, providing a tool for *in situ* computational "microscopy", [57] capable of providing detail of materials behavior on atomistic time and length scales. [120, 121] This approach has been particularly useful in the interpretation of nanoindentation experiments for providing atomic-scale details of the processes that occur underneath an indenter tip and which are inaccessible experimentally. [122–127] Nanoindentation simulations for ice, however, have been extremely scarce. To the best of our knowledge, only the study by Constantin *et al.* [128] has reported molecular level simulations of the indentation process of ice surfaces, investigating the response using the particular TIP5P/Ew model to describe the interactions between water molecules and providing insight into the experimental findings of Pittenger and Butt. Modeling the condensed phases of water has been a notoriously difficult task, however, and oftentimes the results depend critically on the employed molecular model.

In this chapter, we employ the same two different water models used in the previous chapter in the study of uniaxial deformations, the explicit-proton TIP4P/Ice model [14] and the coarse-grained mW description [15], in order to investigate the response to mechanical indentation by a nanometer-scale tip of the ice I_h basal-plane

surface. Furthermore, we employ computational cells that are substantially larger than those considered in Ref. [128]. Indeed, the cells utilized in the latter are rather thin in the indentation direction, in some cases provoking direct interactions of the indenter tip with both the top and bottom slab surfaces. Not only do our results contribute to the discussion regarding the interpretation of experimental AFM loading curves [113, 116–119], they provide valuable insight into the behavior of these two popular water models under such circumstances.

3.2 Computational approach

3.2.1 Water models and Computational Cells

To describe the interactions between the water molecules we employ two different approaches, namely, the explicit-molecule TIP4P/Ice model [14] and the mW potential [15] in which the water molecules are treated as "effective atoms" and the protons have been coarse-grained out of the description. A comparison between the results obtained for both force fields provides insight into the role of water's molecular nature and the inherent asymmetry of the hydrogen bonds. [120, 129]

The cells used for the TIP4P/Ice model correspond to defect-free, proton-disordered ice I_h structures with zero total dipole moment as described in the previous chapter.[120] The cells for the mW model correspond to the same structures generated for the TIP4P/Ice model, but with the protons removed. Most of the simulations presented here were carried out using a small indenter on a cell of $10 \times 10 \times 10$ nm^3 containing 32032 water molecules, with free surfaces on the indentation axis (z) and periodic boundary conditions in the x and y directions. In order to assess the role of the indenter size, a larger cell of $20 \times 20 \times 10$ nm^3 containing 128128 molecules was also generated.

3.2.2 Equilibration

The ice cells were first equilibrated at zero pressure and at the desired temperature through a NPT ensemble for which the cell dimensions are allowed to vary independently. In the x and y directions the pressure is controlled by a barostat, while in the z direction the pressure is held at zero by introducing a vacuum space in the simulation box above and below the free surfaces. The insertion of empty volume between atom slabs imposes the need to remove dipole inter-slab interactions (using a planewise geometry approximation to calculate long-range Coulombic forces) so that slab-slab interactions are effectively turned off. [130] All the simulations have been carried out using the `LAMMPS` MD package, [89] using a Parrinello-Rahman-type barostat [90–92] and a Langevin thermostat [93]. The corresponding equations of motion are integrated using a time step of $\Delta t = 1$ fs for the TIP4P/Ice model and $\Delta t = 5$ fs for the mW model. For both models, the damping time scales for the thermostat and barostat were chosen as $\tau_T = 0.2$ ps and $\tau_p = 2$ ps, respectively. For the TIP4P/Ice all-atom model, bond lengths and angles are constrained using the `SHAKE` algorithm, [94] and the long-range electrostatics are handled employing the particle-particle particle-mesh (PPPM) scheme. [17]

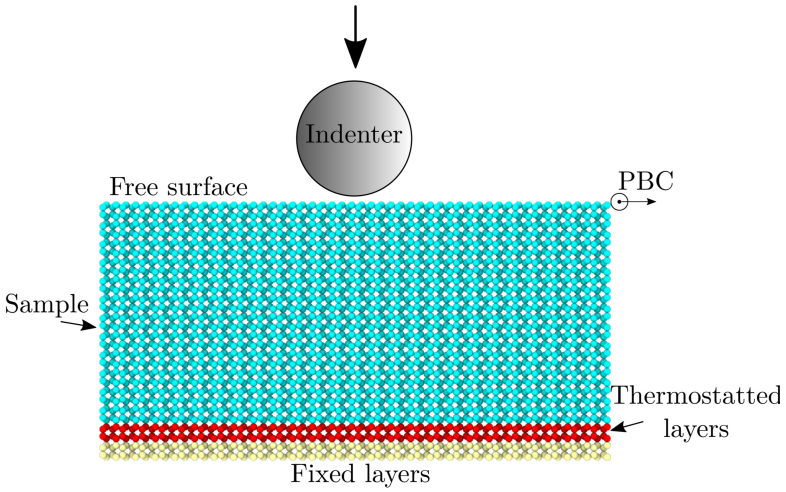

Figure 3.1: Diagram of the sample geometry and boundary conditions employed for the nanoindentation process using a spherical indenter. Periodic boundary conditions are applied in the two directions perpendicular to the indentation direction. The two molecular layers on the bottom of the cell, shown in yellow, are held fixed, whereas thermostatting is applied only to the two subsequent layers, shown in red.

Following the initial NPT run, a second equilibration is carried out using boundary conditions that will also be used during the indentation process, as shown in Fig. 3.1. In addition to turning off the barostat, the deepest two bilayers of the cell are now held fixed. Furthermore, we also modify the thermostatting scheme, applying a Langevin-thermostat bath only to the two bilayers above the two fixed layers. In this fashion, the dynamics of the layers that effectively interact with the indenter is governed only by intermolecular forces and the action of the indenter, not being subjected to the artificial dynamical elements introduced by thermostats and barostats. Indeed, this local thermostatting scheme is adequate in that it produces a homogeneous temperature profile for the molecular layers. To verify whether the local thermostatting scheme gives appropriate temperature control, we monitor the mean temperature per molecular layer, both in the equilibration as well as indentation runs. Typical results for the mW model are shown in Fig. 3.2, which displays average temperature values for the cell as a whole, as well as layer-averaged values at different depths. Except for larger fluctuations due to the smaller number of molecules in individual layers, their mean temperature values are identical to that of the cell as a whole as set by the thermostat, and there are no appreciable temperature gradients.

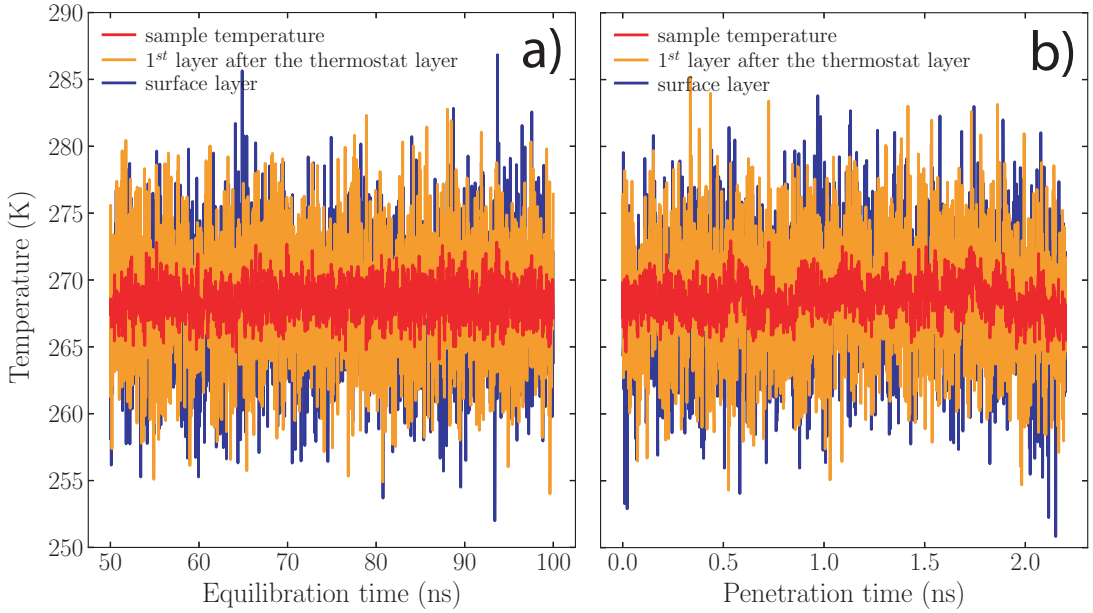

Figure 3.2: Average temperature for different molecular layers for the mW model at 269 K during (a), equilibration and (b), during an indentation simulation. Red lines depict the overall mean temperature, taking into account all the molecules in the cell. Orange lines are the average temperature of those molecules that belong to the layer immediately above the two thermostatted layers. Blue lines correspond to the mean temperature for the top-most surface layer.

The simulations have been carried out for two temperatures for both models, with the intent of analyzing the influence of a quasi-liquid layer (QLL) at the ice surface. In particular, the indentation simulations have been carried out at a low temperature of 50 K, for which the QLL is absent, as well as temperatures $\sim 5\,K$ below the melting point, when a substantial pre-melt layer is known to cover the ice surface for both models. [131–136] For 50 K temperature, both the first and second equilibration stages involved a time interval of 5 ns. On the other hand, for the temperatures close to the melting point, we increased the length of this interval to 25 ns, given that the equilibration of the QLL is comparatively slow. [132] This time interval is sufficiently long to produce a converged, steady-state QLL fraction under these conditions.

3.2.3 Indentation simulations

Following the second equilibration stage, nanoindentation simulations were performed using the same boundary conditions, with a chemically inert indenter characterized by a purely repulsive spherical tip that interacts with the substrate according to the potential-energy expression [137]

$$V(r_i) = \begin{cases} k(R - r_i)^3, & r_i < R, \\ 0, & r_i \geq R, \end{cases} \tag{3.2.1}$$

with R the indenter radius, r_i the distance of molecule i to the center of the indenter, and k is the specified force constant. Given the purely repulsive nature of the indenter-substrate interaction, no capillarity effects are present. The determination of the load-displacement curves is straightforward, as the total normal force exerted by the indenter is determined by summing the pairwise z-axis contributions of all the molecules interacting with the indenter. All indentation processes were carried out by pressing the indenter into the substrate in a displacement-controlled manner [137] characterized by a constant indenter velocity, using values of 1 and 10 m/s, respectively. To assess possible effects associated with the radius of the indenter we carry out simulations using radii of $R = 2$ nm and $R = 3$ nm. To reduce periodic image effects during the indentation, we employ cells with different cross-sectional areas for the two indenter radii, using the $10 \times 10 \times 10$ nm^3 cells for the 2 nm tip, and the $20 \times 20 \times 10$ nm^3 samples for the 3 nm radius. Given

the prohibitively elevated computational cost associated with the long-range electrostatic interactions of the TIP4P/Ice model, the calculations with the largest tip radius have been done only for the mW model. To mitigate strain rate effects and study residual imprints, a subset of simulations was performed in three stages. In stage I (penetration stage), the indenter penetrates into the sample to a prescribed depth. Subsequently, in stage II (holding stage) the indenter is kept at constant depth for a given time, followed by stage III (removal stage) in which the indenter is removed from the substrate using the same speed used in stage I.

At the nanoscale, the tips are usually blunt (rounded). Indeed, most simulations are performed for the spherical tips, and yet the results can be considered useful to investigate some effects during the indentation process and is a good approximation to test the macroscopic laws on the nanoscale. [126] For small penetrations, we can also use the Hertz model, where a conical tip can be considered a spherical tip. [138] This model is also useful for estimating quantities from experimental measures. [117, 118]

3.3 Results and Discussion

3.3.1 Sample equilibration

Before initiating the indentation process we first assess the equilibration of the computational cells, in particular for temperatures close to the melting point, when premelting is known to occur and the formation of a quasi-liquid layer (QLL) on top of an exposed ice surface is established. To analyze the formation of the QLL on the exposed basal plane surface we monitor the evolution of the number of liquid-like molecules during the equilibration. To this end, we use the `Identify-diamond-structure` [96] (IDS) order parameter implemented in the `OVITO` visualization package to analyze the structure of the oxygen-atom configurations. [97] For the ice I_h structure it is able to classify particles as being of the hexagonal-diamond type, as well as its first and second neighbors. We classify as liquid-like those molecules whose oxygen atoms do not belong to any of these structural categories.

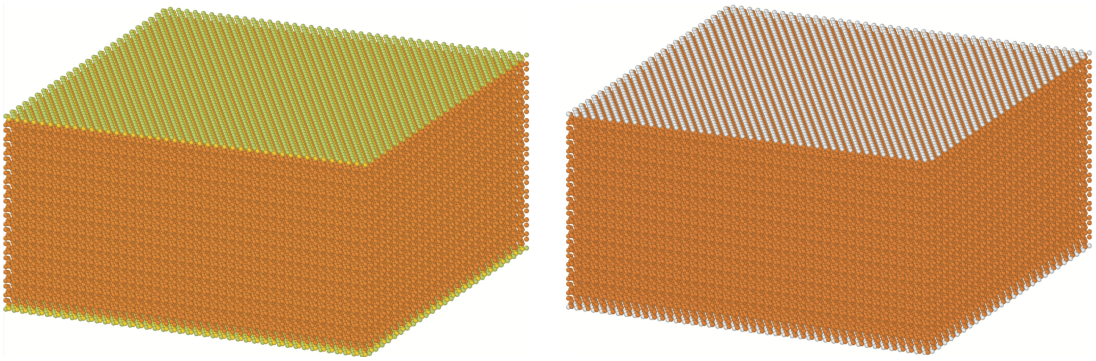

Figure 3.3: Classification of crystallinity on a perfect ice I_h surface as described by the IDS (left) and CHILL+ (right) order parameters. Orange particles are in the hexagonal diamond structure, yellow correspond to hexagonal-diamond first neighbors, green represent hexagonal-diamond second neighbors and white atoms are regarded as in an unknown structure.

The advantage of IDS is that, even in situations of symmetry breaking such as at a surface, it classifies all particles as crystalline when no QLL is present at low temperatures. The Identify-Diamond-Structure (IDS) order parameter [96] that we use prioritizes the relative positions of neighboring atoms to classify the crystallinity of particles. Specifically, the algorithm analyzes the local environment of an atom up to the second neighbor shell to determine the local structural type. In this manner it is able to classify an atom as being in a complete hexagonal/cubic diamond environment, as well as first and second neighbors of the hexagonal/cubic diamond structure. Because of this extended analysis of the IDS algorithm it actually correctly classifies atoms located at the ice-vacuum interface as crystalline. This can be seen in the left part of Fig. 3.3, which displays a slab of ice in perfect Ih structure with 128128 water molecules and in which oxygen atoms have been colored according to the IDS order parameter, with orange being hexagonal diamond, yellow corresponding to hexagonal-diamond first neighbor and green representing hexagonal-diamond second neighbor. This means that, even with the symmetry breaking at the surface, all atoms are being classified as crystalline, as they should. Interestingly, this is different for the `CHILL+` order parameter, [77] as displayed by the right part of the picture below. The particles on the outermost layer (in white) are being classified as "unknown", even when they are clearly in a crystalline arrangement.

Fig. 3.5 displays snapshots from the 32032-molecule cells of the molecular structure of the basal plane for the TIP4P/Ice and mW models after equilibration at

temperatures 264 and 269 K, respectively. For the TIP4P/Ice force field there is a well-formed QLL with a thickness of $\sim$ 7.5 Å, which corresponds to roughly two crystalline layers along the c-axis. In addition, the fraction of liquid-like molecules in these layers is approximately 0.83, which is consistent with previous reports. [131–133] On the other hand, for the mW model the QLL is substantially thinner, showing a layer with a thickness of $\sim$ 3.7 Å, corresponding to a single crystalline bi-layer, and a liquid fraction of only $\sim$ 0.24. This result deviates from recent studies [134–136] in which liquid fractions of $\sim$ 0.65 were reported. To rule out a possible insufficiency in the equilibration time, we executed a single longer simulation of 100 ns, obtaining the same QLL fraction. Fig. 3.4 shows the QLL fraction as a function of time for both the mW and TIP4P/Ice models. It is clear that the QLL equilibrates very quickly for the mW, whereas it takes somewhat longer for TIP4P/Ice. Nevertheless, for an equilibration time of 25 ns, both systems have clearly reached a steady plateau value, attesting that the QLLs have in fact reached a steady state.

A possible reason for this difference is that Refs. [134–136] all use the `CHILL+` order parameter [77] instead of IDS. As shown in Fig. 3.3, in contrast to IDS, the `CHILL+` order parameter does not recognize water molecules at a defect-free ice surface to be crystalline, even at very low temperatures when no QLL is present.

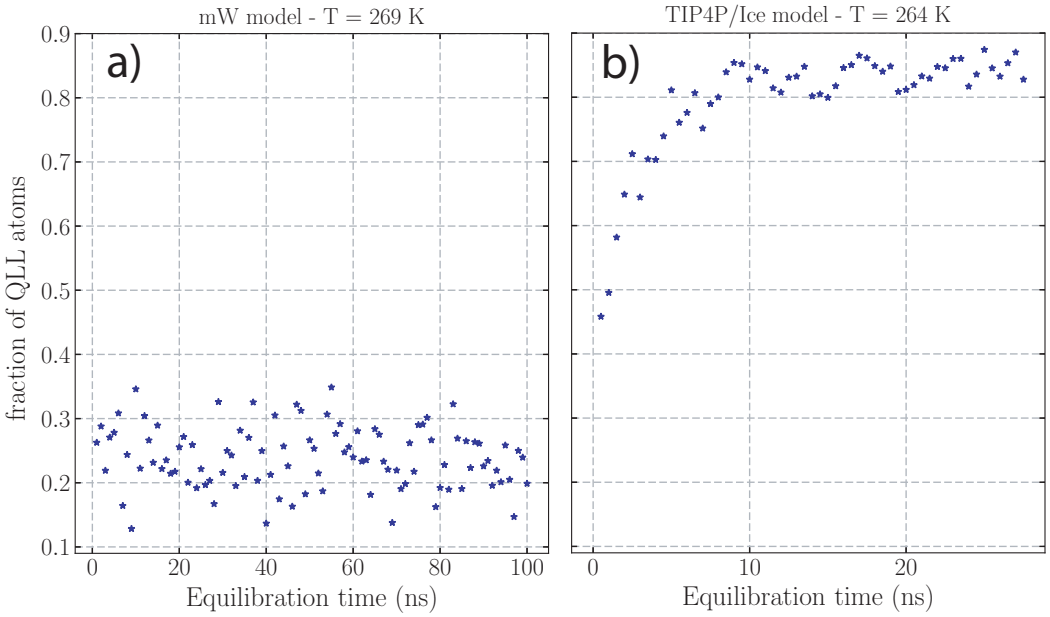

Figure 3.4: Evolution of the QLL fraction as a function of the equilibration time for, (a) the mW model and, (b), the TIP4P/Ice potentials, both at a temperature of 5 K below their respective melting points.

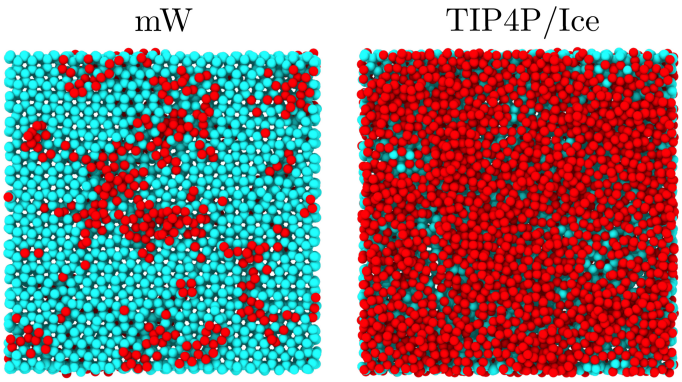

Figure 3.5: Premelting at the ice-vacuum interface at 269 and 264 K from simulations using the mW and the TIP4P/Ice water models. Red and cyan spheres depict water molecules in the QLL and the hexagonal ice structure, respectively. The fraction of liquid water in the top layer for the mW and TIP4P/Ice models are ~ 0.24 and ~ 0.83. respectively.

3.3.2 Loading curves and deformation mechanisms

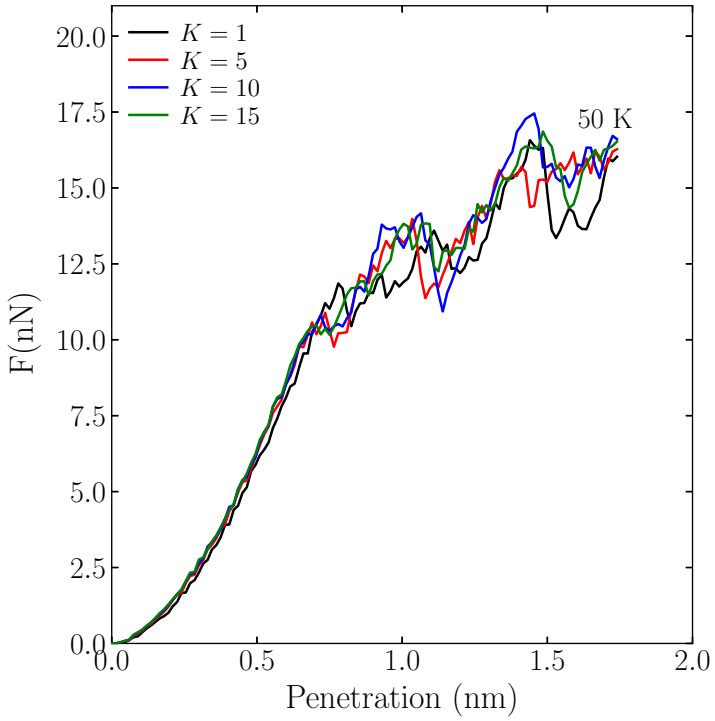

Figure 3.6: Normal force on the indenter as a function of the indentation depth for the 32032-molecule cell interacting through the mW model at $T = 50$ K using the indenter with $R = 2$ nm and a penetration velocity of 1 m/s for 4 different values of k ranging from 1 to 15 eV/Å^3.

To choose a value for the indenter force constant k, we execute a number of indentation simulations for the 32032-molecule cell interacting through the mW model

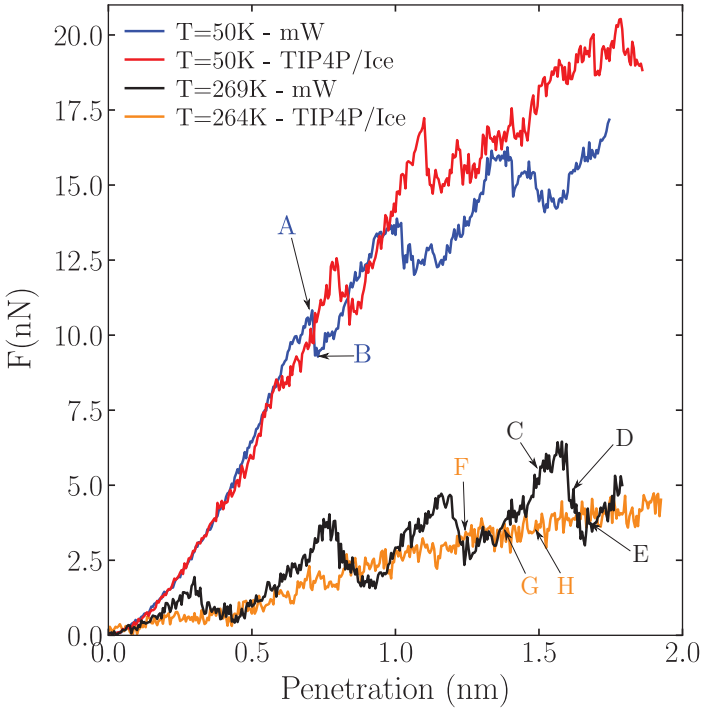

Figure 3.7: Normal force vs indentation depth during the indentation process, comparing the TIP4P/Ice and mW models for the two temperatures in study, with a tip radius of 2 nm and a velocity penetration $v = 1$ m/s. Letters indicate moments immediately before and after large drops in the FP curves due to localized events, as discussed in the text. Distances between the peaks for the mW model at 269 K are close to 3.7 nm, which corresponds to the separation between basal-plane bi-layers in the ice I_h structure.

at $T = 50$ K using the indenter with $R = 2$ nm and a penetration velocity of 1 m/s. Following previous indentation simulations we determine the normal force on the indenter as a function of the penetration depth for 4 different values of k, chosen between 1 and 15 eV/Å^3. [121, 137, 139, 140] As shown in Fig. 3.6 the resulting curves are essentially insensitive to the particular choice of k, indicating that for these values the indenter may be considered to be ideally rigid. All remaining indentation simulations have been carried out using $k = 10$ eV/Å^3, which is widely used in nanoindentation simulations on metals. [121, 137, 139, 140]

Fig. 3.7 compares typical force-penetration (FP) curves obtained for the TIP4P/Ice and mW models at the low and high temperatures using the 2 nm indenter tip at a penetration velocity of 1 m/s. Considering the results obtained for the mW model, the 50 K FP curve can be divided into a comparatively smooth elastic regime followed by the occurrence of a succession of stress-relief events during which the normal

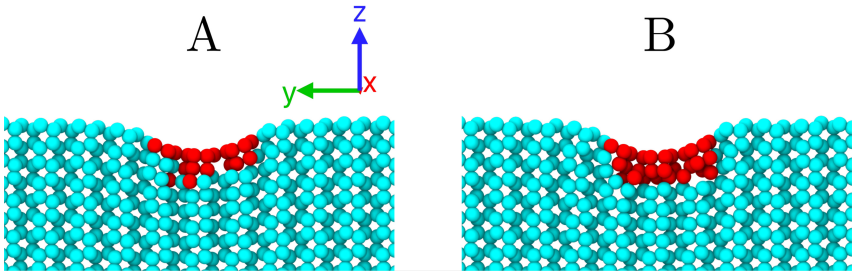

Figure 3.8: Atomic configurations corresponding to the instants A and B marked in Fig. 3.7. Particle colors indicate different crystalline environments, with cyan indicating particles in a Wurtzite-structure surrounding, including either a Wurtzite first- or second-neighbor, and red particles belonging to disordered regions.

force on the indenter tip decreases suddenly upon increasing penetration. The first force drop appears at a depth of $\sim$ 7 Å, between the instants marked as A and B in Fig. 3.7. To correlate the non-monotonic features in the FP curve with changes in the substrate microstructure we analyze atomistic configurations for these two instants and use the hexagonal-diamond-structure order parameter [96] in `OVITO` to classify the crystalline environments of each water molecule. The results are presented in Fig. 3.8, with the cyan color indicating Wurtzite-type crystallinity, while red color indicates amorphous structure. At A, immediately before the first stress-relief event, the top three bi-layers are severely strained with some disorder in the two first layers. At configuration B, right after the drop, the extent of the amorphous region below the indenter tip increases to the first three bi-layers. This localized amorphization acts as a stress-relief mechanism for the deeper layers. For instance, after the local amorphization of the first 3 bi-layers, the strained part of the fourth bi-layer is able to almost entirely restore its unstrained vertical position. The subsequent drops in the FP curve for mW-50K, correspond to a similar amorphization of the 4th and 5th bi-layers, respectively. Indeed, the penetration-depth distance between the drops is close to the separation between two bi-layers in the ice I_h structure.

The FP curve for the TIP4P/Ice model at the same temperature is qualitatively similar to its mW counterpart, with the elastic portions essentially overlapping and a similar pattern of stress-relief events in the plastic regime. Indeed, the basic deformation mechanism associated with the appreciable force drops is the same as that seen for the mW model, i.e., localized amorphization of the region underneath the indenter tip.

Close to the melting point, however, the behavior is markedly different for both models. While both display similar elastic softening compared to the 50 K case for small strains, the FP curves display distinct behavior for larger penetration depths. For the mW model the FP curve features a serrated nature, characterized by a succession of steep rises followed by sudden drops. These sequences are essentially equidistant, separated by a distance of ~ 3.7 Å, which corresponds to the bi-layer separation in the ice I_h structure. For TIP4P/Ice, on the other hand, the FP curve increases steadily with the penetration depth without any pronounced features. Inspection of the configurations reveals that the succession of rises and drops corresponds to consecutive bi-layer by bi-layer melting, followed by partial recrystallization. This is illustrated in Fig. 3.9, which displays the oxygen positions at the instants marked C, D and E in Fig. 3.7. At configuration C, close to the end of a rise in the FP curve, the structure underneath the indenter is almost entirely crystalline such that the increase of the FP curve is related to the build-up of elastic strain in the layers below the tip. The subsequent stress drop, illustrated at point D, is achieved by melting of the bi-layer immediately below the tip, visibly relieving the strain below. However, after the appearance of the melt layer underneath the indenter, a significant fraction recrystallizes, as seen at configuration E, initiating a new build up of elastic stress. This serrated structure is consistent with the previous findings by Constantin *et al.*, [128] using the TIP5P/Ew water model.

Fig. 3.10 explicitly shows the recrystallization occurring during the indentation process when the interactions are described by the mW model. The picture on the left displays a snapshot just after localized melting has occurred, with the entire pit coated with liquid-like particles (shown as white) as identified by the IDS order parameter. The arrows point at 3 particular particles that are classified as liquid-like at this instant. The image on the right displays the situation 80 ps later. Most of the particles in the pit are now in a crystalline environment. Moreover, given that all 3 particles classified as liquid-like in the image on the left are now in crystalline surroundings.

The TIP4P/Ice model at 264 K behaves differently. Although stress relief also occurs by means of bi-layer by bi-layer melting, there is no recrystallization, giving a FP curve that is mostly monotonic. As illustrated in Fig. 3.9 for the configurations marked as F, G and H in Fig. 3.7, the increasing penetration depth gives rise to the

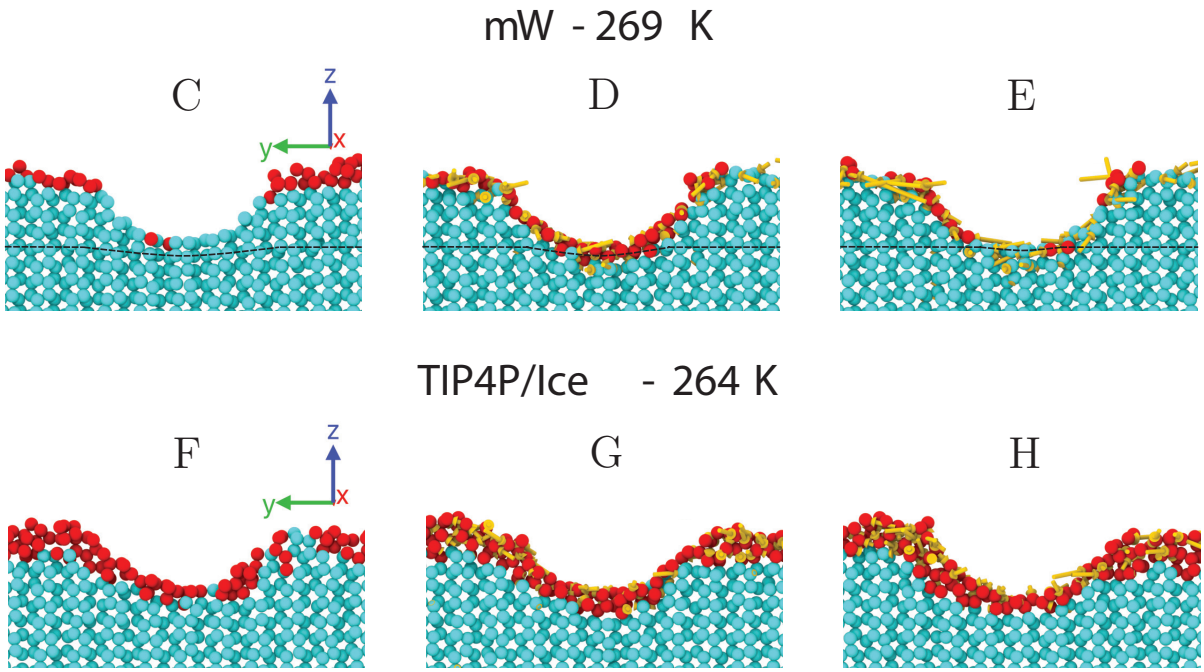

Figure 3.9: Atomic configurations corresponding to the instants C-D-E and F-G-H in Fig. 3.7. Particle colors indicate different crystalline environments, with cyan indicating particles in a Wurtzite-structure surrounding, including either a Wurtzite first- or second-neighbor, and red particles belonging to disordered regions. Yellow arrows depict the displacements. The dashed black line serves as a guide to the eye to appreciate the relaxation of the tension of the third and fourth bi-layers after the melting of the second and third, respectively.

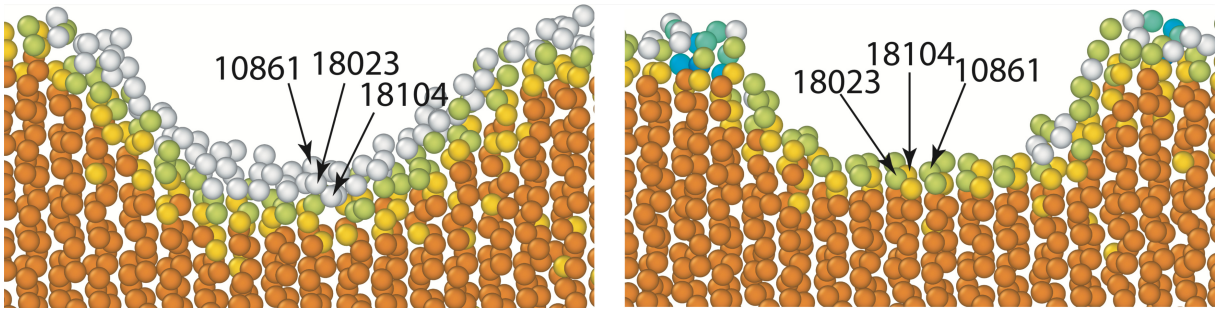

Figure 3.10: Snapshots during indentation simulation based on the mW model. Coloring of the particles is according to the IDS order parameter, using the same coloring scheme as that in Fig. 3.3. Right image corresponds to an instant 80 ps after that shown on the left. The arrows and corresponding labels correspond to the particle numbers during the simulation. Blue atoms are locally in cubic diamond structure.

same bilayer melting process seen for the mW model. However, instead of the substantial recrystallization seen for the latter, the indentation pit for TIP4P/Ice remains coated with a liquid-like layer at all times.

Increasing the size of the indenter does not give rise to substantial alterations in the behavior. This is shown in Fig. 3.11, which compares the 2-nm FP curves to those

obtained for an indenter radius of $R = 3$ nm for the mW model. The latter were carried using the large $20 \times 20 \times 10$ nm^3 cell with double the surface area to reduce image effects due to the larger indenter size. With the exception of the faster rise of the elastic part due to the increased contact area and minor dislocation activity at 50 K, [120] the general features of the FP curves obtained for both indenter sizes are the same, with similar sequences of events and the activity of the same main relief mechanisms of bi-layer by bi-layer amorphization/melting, including its serrated character just below the melting point. The fact that the serrated nature of the FP curve close to the melting point is present for both indenter radii contrasts the findings of Constantin *et al.*, [128] in which an indenter radius of 0.55 nm was found to produce a peak-like structure, whereas a value of 1.80 nm did not. This difference was interpreted as a commensurability issue, with the smaller radius being compatible with the bi-layer spacing of ~ 0.37 nm whereas the larger tip would not. Our results do not display such compatibility issues, giving serrated FP curves for both the 2 nm and 3 nm indenter tips.

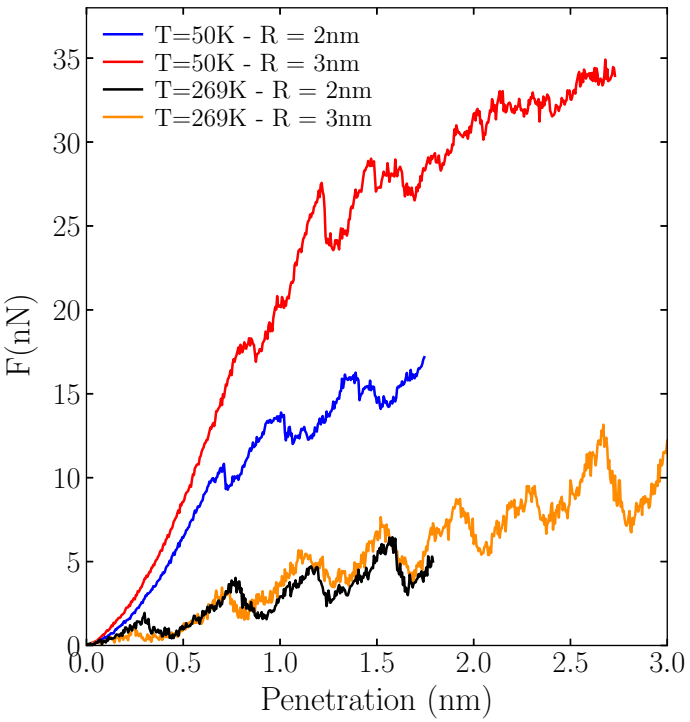

Figure 3.11: Normal force on the indenter as a function of penetration depth for tip radii of $R = 2$ nm and $R = 3$ nm for the mW model at 50 and 269 K for a penetration velocity of 1 m/s.

Overall, the results above show that, although the main mechanism of stress relief under indentation is the same for both models, namely bi-layer by bi-layer

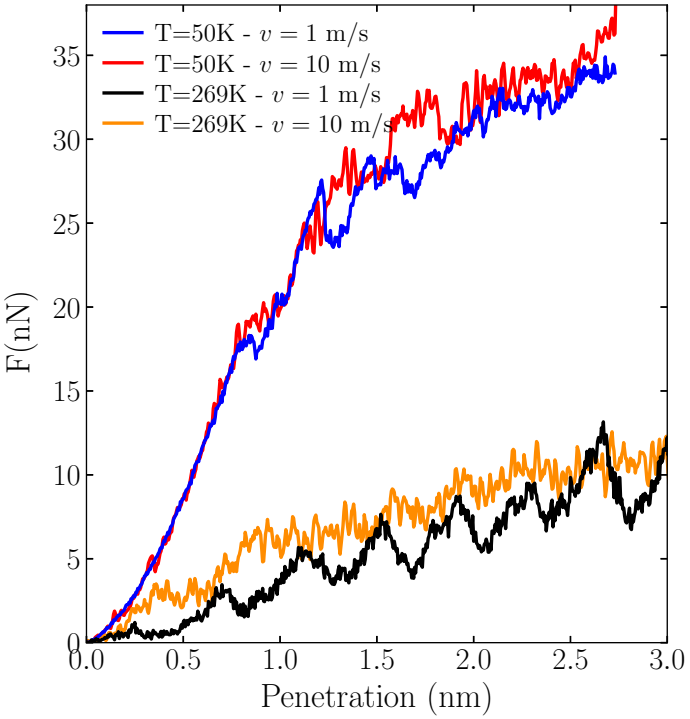

Figure 3.12: Velocity dependency of the normal force vs indentation depth during the indentation process, using the mW model with a 3 nm tip radius for the two temperatures in study.

amorphization/melting, their behavior just below the melting point is very different. While the mW model displays substantial recrystallization following each melting stress-relief event, leading to a serrated FP curve, the TIP4P/Ice model maintains the presence of a liquid-like layer underneath the indenter at all times. Comparison of these findings to experimental AFM results, [115, 116, 118] which indicate the presence of a QLL between the indenter tip and the substrate, [115, 116, 118] thus suggest that the explicit-proton TIP4P/Ice model provides a better description of the indentation process compared to the coarse-grained mW model. This is possibly related to the absence of explicit protons in the mW model, by which the intrinsic asymmetry of the hydrogen bond (HB), with one molecule donating a proton and another accepting it, is lost. As such, the formation of effective HBs in this model is not hampered by steric effects and recrystallization in the presence of a crystalline substrate is facilitated compared to the explicit-proton TIP4P/ice model. In fact, whether or not HBs are treated explicitly has been shown to fundamentally affect mechanical behavior of ice I_h. [120, 141]

An indication that this effect is indeed occurring is obtained by reducing the

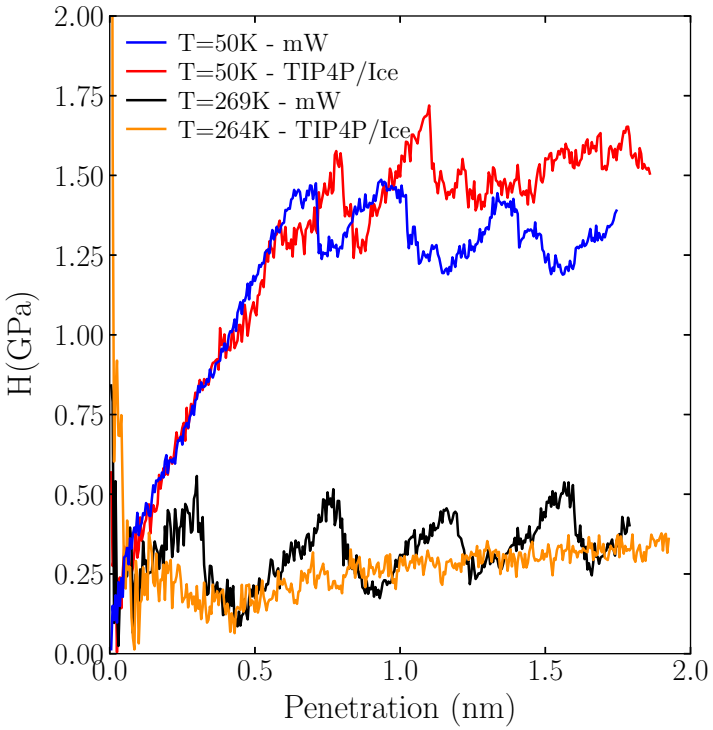

Figure 3.13: Contact pressure as a function of penetration depth for the mW and TIP4P/Ice model for the 2 nm indenter and for the two temperatures in study.

time scale of the indentation process, increasing the tip velocity to 10 m/s. Fig. 3.12 displays the mW FP curves obtained with the 3 nm tip radius at 50 and 269 K for indenter velocities of 1 and 10 m/s, respectively. While the behavior is mostly the same for both velocities at 50 K, the increase of the indenter velocity leads to the disappearance of the serrated character of the FP curve at 269 K. This is due to the elevated penetration rate, which prevents liquid atoms below the indenter from recrystallizing, maintaining a QLL between the indenter and bulk ice throughout the entire process.

3.3.3 Hardness

A property that can be estimated quantitatively during the indentation process is the hardness H, [104] which is related to the contact pressure exerted by the indenter tip. In the Meyer approach, the latter is defined as the ratio between the normal force F_N and the projected contact area A_c of the indenter tip. For a spherical indenter of radius R it is given by the geometric cross-section area, $A_c = \pi(2Rh - h^2)$, [104] with h the penetration depth. Fig. 3.13 displays the contact pressure obtained for the TIP4P/Ice

and mW models using the normal-force data from Fig. 3.7.

Based on the contact-pressure curve, the hardness can be defined as the average contact pressure after it has reached a steady-state value. For the case shown in Fig. 3.13, this corresponds to the final 1 - 1.5 nm of penetration. For the TIP4P/Ice model the corresponding hardnesses are $H \simeq 1.5$ GPa and $H \simeq 0.35$ GPa, respectively, for $T = 50$ and 264 K. For the mW model the determination of the hardness value is more difficult due to the serrated nature of the contact pressure, but taking it to be the average value over last 1 nm of penetration we obtain $H \simeq 1.25$ and $H \simeq 0.4$ GPa at 50 and 269 K, respectively. In addition to an overall elastic softening of the crystal, the strong decrease of the hardness with temperature is enhanced by the presence of the QLL, in particular for the TIP4P/Ice model.

A direct comparison of these values with experimental estimates is difficult. The main issue is the fact that the values of the hardness measured in this manner depend on the penetration velocities, which, in experiment are much smaller than those applied in simulations. From a qualitative standpoint, it is known that increasing penetration velocities give rise to higher hardness measures [112, 118] Our results are consistent with this trend in that the normal-force data for an indenter velocity of 10 m/s in Fig. 3.12 give rise to hardness measures that increase by $\sim 10\,\%$ for both temperatures. A direct quantitative comparison, however, is inconceivable due to the disparities between the experimental and simulation time scales. Experimental values for tip radius, indenter velocity and maximum penetration depth are ~ 10 nm, $\sim 10^{-6}$ m/s, and ~ 100 nm. [112, 117, 118]

One way to mitigate the effects of the finite penetration rate is to adopt the Meyer estimate of the hardness H, which is defined as the average contact pressure with full plasticity developed. [104] This means that, for a given penetration depth, one measures the contact pressure after the indenter tip has created a stable residual pit with a cross-sectional area close to A_c and which persists upon removal of the indenter tip. To this end, we employ a protocol in which, after attaining an indentation depth close to the indenter radius, the position of the tip is held fixed, allowing the system to relax during a time interval sufficiently long to attain equilibrium. Subsequently, after reaching a steady value of the contact pressure, the indenter tip is withdrawn with the

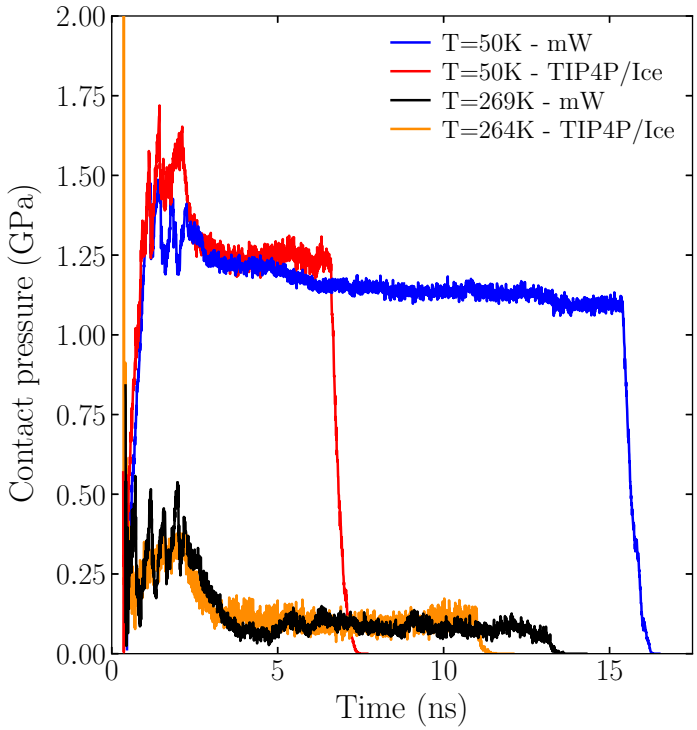

Figure 3.14: Contact pressure as a function of simulation time during the indentation/hold/withdrawal process for indenter radius of 2 nm.

same velocity used for the indentation stage.

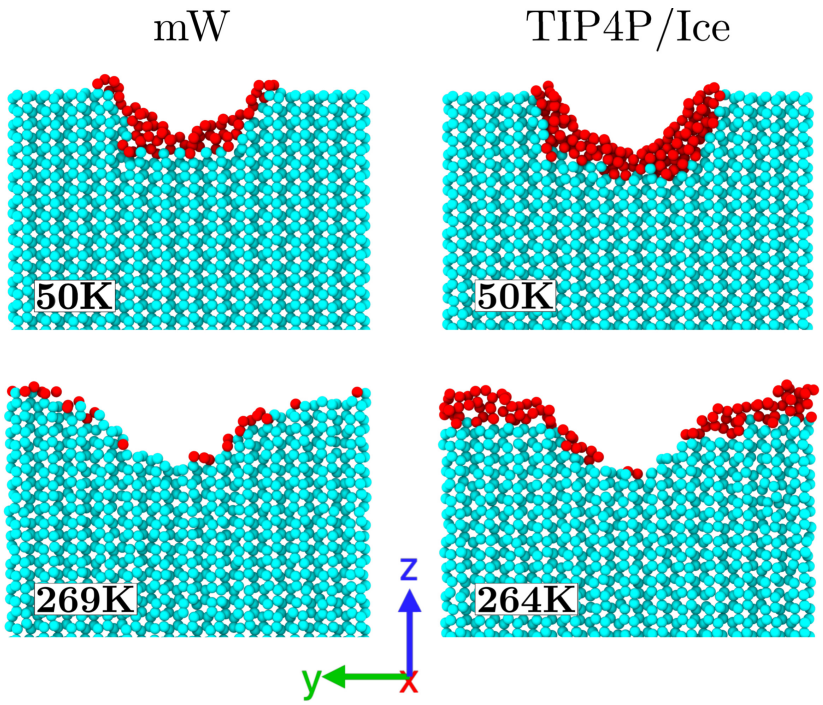

Figure 3.15: Residual structures upon removal of the indenter. Coloring scheme is the same as that in Fig. 3.9.

Fig. 3.14 shows the contact pressure as a function of simulation time along the

entire loading-unloading cycle for the mW and TIP4P/ice models for the 2 nm indenter tip and an indentation velocity of 1 m/s for both temperatures. The plateau values reached during the hold stage provide the Meyer estimates for H. They display very significant reductions compared to their values at the end of the indentation stages, reducing by as much as ~ 0.30 GPa for the mW model at 269 K. The residual indentation pits after full withdrawal are shown in Fig. 3.15, with well-established amorphous layers for both models at 50 K and the presence of some QLL close to the melting temperature. However, the amount of QLL in the relaxed pit is notably smaller than during the indentation process as seen in Fig. 3.9, in particular for the TIP4P/Ice model. Indeed, when computing the corresponding hardnesses using the relaxed steady-state normal forces, the values for mW and TIP4P/Ice in the vicinity of their melting temperatures are very close for both models, $\sim 0.08 - 0.09$ GPa, of the same order of magnitude as that of the lowest experimental indenter velocity result ~ 0.01 GPa reported by Pittenger *et al.* [118] and even comparable to the Brinnel hardness obtained macroscopically, 0.04 GPa, reported by Butkovich [142]. This suggests that, despite the clearly different behavior of the FP curves during the indentation process, in particular close to their respective melting points, the steady-state hardnesses predicted by both models after reaching stable indentation pits are much less affected by the QLL, which is seen to recede mostly to the surface outside the pits for both models. These findings are consistent with the interpretation of the experiments of Butt *et al.* [117], arguing that most of the QLL is squeezed out from the indentation pits and also lend support to the recent experiments of Constantin *et al.* [119] that report substantially reduced QLL thicknesses.

3.4 Summary

In conclusion, we have used molecular dynamics simulations to investigate the response of ice I_h under nanoindentation process on a [0001]-oriented surface, using the all-atom TIP4P/Ice potential and the coarse-grained mW model. Using a purely repulsive, chemically inert spherical tip, we studied the nanoindentation response under controlled displacement conditions for two markedly different temperatures, the first being 50 K, at which the QLL is absent, and the second corresponding to a value 5 K below the

respective melting temperatures for the both models with a substantial QLL presence. Furthermore, we also explore the role of indenter size and displacement velocity on the loading curves and deformation mechanisms.

We find that the QLL fraction is dramatically different for the two potentials just below the melting temperature; not only does the fraction differ by more than a factor three, there are also substantial differences in the QLL thickness, with TIP4P/Ice presenting the largest QLL fraction and thickness.

Overall, the dominating deformation mechanism is the same for both models, namely bi-layer by bi-layer amorphization/melting induced by pressure. However, while the TIP4P/Ice model maintains the presence of a QLL layer below the indenter at all times, the mW model alternates recrystallization and amorphization events, giving rise to serrations in the loading curves for the latter. Such behavior is attributed to the lack of explicit protons in the mW model, which facilitates recrystallization compared to the TIP4P/Ice model.

Notably, despite differences in the formulation of the two water models used, the obtained results for the steady-state hardness for both models were found to be consistent with experimental AFM reports, giving values that are of the same order of magnitude. Furthermore, in agreement with experimental literature, hardness increases as penetration rate grows, while it decreases as temperature increases, with an overall softer response attributed to the presences of the QLL.

Residual imprints remaining after removal of the indenter show that the amorphization found for very low temperature is stable and remains in the pits. Just below the melting point, however, the residual imprints have no amorphous layers, and most of the QLL atoms have been displaced to the surface outside the pit, in agreement with the interpretation of Butt *et al.* in Ref. [117] and possibly explaining the recent measurements by Constantin *et al.*. [119]

The results presented here serve a variety of purposes. In addition to contributing to the discussion regarding the interpretation of experimental AFM loading curves [113, 116–119], they provide valuable information concerning the simulation of contact problems involving ice and the characterization of two popular water models

under such circumstances. In particular, future efforts may include a more accurate computational representation of AFM indenter tips in terms of shape/size and its interaction with the substrate, [143] to capture effects such as jump-to-contact phenomena. [144]

Chapter 4

Nonequilibrium Processes in Repulsive Binary Mixtures

This chapter was reproduced from [P. A. Santos-Flórez and M. de Koning, J. Chem. Phys. 152, 234505 (2020)], with the permission of AIP Publishing.

4.1 Introduction

Classical systems described by repulsive pair potentials have been the subject of intense investigation for over five decades. [145–175] Not in the least due to their role as effective descriptions for interactions in soft-condensed-matter systems, [176–186] substantial effort has been directed towards elucidating the equilibrium phase behavior of such models, considering both single-component samples as well as multi-component mixtures. [161–175]

Nonequilibrium phenomena, on the other hand, have received much less attention, despite their key role in self-organization phenomena in such systems. [187–197] Indeed, one of the challenges in soft-matter materials design concerns the ability to adjust the effective interaction parameters so as to control the self-organization process and achieve desired self-assembled structures. [197] In this context, processes that display spontaneous development of structure from an initially

disordered, far-from-equilibrium state are of particular interest. [187, 196, 197]

A typical example is a process in which a system initially at equilibrium in a high-temperature state is suddenly quenched to low temperature. [198] Because of the instant cooling, the initial high-temperature phase falls out of equilibrium and spontaneously decays into a low-temperature state. However, due to the intrinsic nonequilibrium nature of this cooling protocol the corresponding low-temperature state most often does not correspond to that given by the equilibrium phase diagram, characterizing the intrinsic nonequilibrium nature of the process.

When considering mixtures, the sudden quench of a high-temperature state can give rise to two kinds of decay processes. [198, 199] The prototypical example of the first kind are unmixing phenomena in which the final low-temperature state is characterized by chemical ordering through phase separation, whereas the second type is typified by the development of structural order. While unmixing transitions are quite common for the class of repulsive pair potentials, [185, 200, 201] the occurrence of the second type of process is not. In fact, as far as model systems are concerned, to the best of our knowledge such structural ordering phenomena have so far only been observed for discrete spin systems such as the Ising model, [198] while there have been no reports for systems characterized by continuous interactions. Above all, to date there are no known model systems that can display both types of processes as a function of boundary conditions and/or model parameters.

Here, we show that 3-dimensional binary mixtures described by purely repulsive pairwise interactions display both kinds of decay processes and that the observed type can be controlled by tuning the interactions between unlike particles. While strong inter-species repulsion gives rise to chemical ordering through unmixing, weak values lead to a spontaneous development of structural order, forming a polycrystalline solid of uniform chemical composition. Interestingly, this crystallization process is barrierless in nature and gives rise to grain-size distributions that display scale-invariant characteristics. Furthermore, the results suggest that the dual-type decay behavior is universal for pairwise repulsive potential-energy functions in general and that the propensity of the crystallization process is related to their behavior in the neighborhood of zero separation.

4.2 Computational Approach

4.2.1 Simulation Protocol

We consider the case in which the cooling process is infinitely rapid, meaning that the initial infinite-temperature (i.e., ideal-gas) state is instantly quenched to zero temperature. Because the quench is infinitely fast, the system has no time to explore the potential-energy landscape (PEL) and is instantaneously driven to the local minimum closest to the initial configuration, also known as its inherent structure (IS). [202–204] In this sense, the process is fundamentally different from a quasi-static cooling protocol in which the system is at equilibrium at all times and the outcome is determined by the equilibrium phase diagram.

The quench process is implemented computationally in the following way. First, for a specified particle density, we construct a cubic, periodic simulation cell with a volume V that corresponds to a given total particle number N. Subsequently, the system is initialized by randomly placing the N particles in the cell, giving rise to a structureless, uniform position distribution that represents an infinite-temperature, i.e., ideal-gas state. Then, to locate the corresponding IS, a conjugate-gradient (CG) minimization is invoked. For each set of interaction properties and particle densities this procedure is repeated several times using different random initial conditions. All the CG calculations have been performed using the Polak-Ribiere version of the CG algorithm as implemented in the `LAMMPS` package, [89] which is among the most efficient local minimization algorithms for functions of many variables. [205]

4.2.2 Interaction Models

We carry out the quench protocols described in Sec. 4.2.1 for a set of five different purely repulsive pair interaction models. Specifically, we consider, (i), the Uhlenbeck-Ford (UF) model, [206–209] (ii), the inverse fourth (IPL4) and sixth-power (IPL6) potentials, [201], (iii), the Weeks-Chandler-Andersen (WCA) force field, [210]

and, (iv), the Gaussian-core (GC) potential. [164]

The UF model [206–209] is characterized by a logarithmic divergence at zero separation and belongs to the class of so-called ultrasoft potentials. [180] It is defined by the potential-energy function

$$u_{ij}(r) = -\epsilon_{ij} \ln(1 - e^{-r^2/\sigma_{ij}^2}), \tag{4.2.1}$$

where r is the interparticle distance, the indices i and j denote the species of the interacting particles (either A or B) and ϵ_{ij} and σ_{ij} are the corresponding energy and length scales. The cut-off for the interaction calculation is set at $r_c = 4\,\sigma$.

The potential-energy functions describing the IPL4 and IPL6 models [201] are given by

$$u_{ij}(r) = \epsilon_{ij} \left(\frac{\sigma_{ij}}{r}\right)^n, \tag{4.2.2}$$

The exponents for the IPL4 and IPL6 models are $n = 4$ and $n = 6$, respectively, and the cut-offs for the interaction calculation are set at $r_c = 6\,\sigma$ and $r_c = 4\,\sigma$ for the IPL4 and IPL6 models.

The WCA model [210] is defined by the repulsive part of the Lennard-Jones

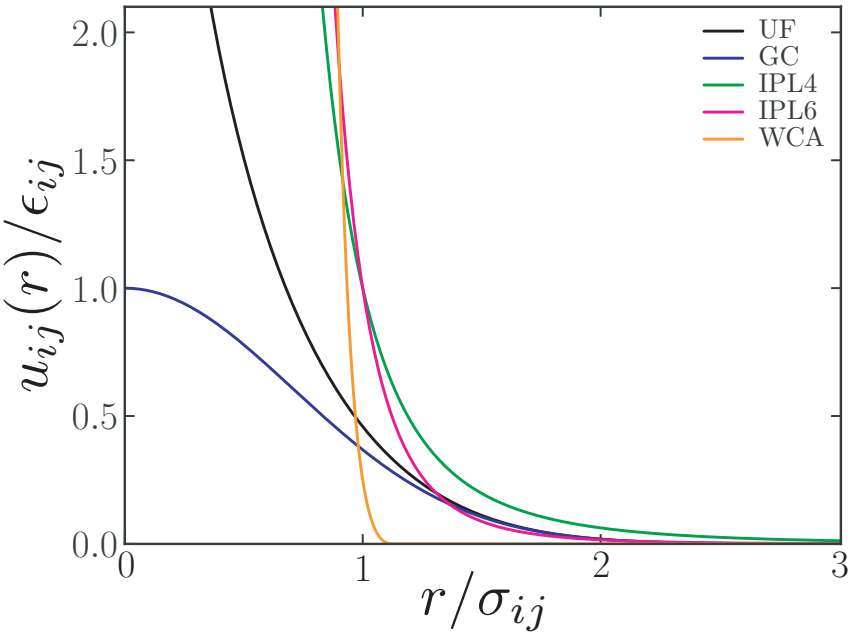

Figure 4.1: Graphs of considered repulsive pair potentials.

(LJ) potential energy function, shifting the LJ function such that the minimum value corresponds to zero, and truncating it for distances beyond that of its minimum at $r = 2^{1/6}\,\sigma$. Accordingly, the WCA force field is defined as

$$u_{ij}(r) = \begin{cases} 4\,\epsilon_{ij}\left[\left(\frac{\sigma_{ij}}{r}\right)^{12} - \left(\frac{\sigma_{ij}}{r}\right)^{6}\right] + \epsilon_{ij}, & \text{if } r \leq 2^{1/6}\,\sigma_{ij} \\ 0, & \text{otherwise.} \end{cases} \tag{4.2.3}$$

Finally, the GC model also belongs to the category of ultrasoft interaction models and is defined as [164]

$$u_{ij}(r) = \epsilon_{ij}\exp(-r^2/\sigma_{ij}^2). \tag{4.2.4}$$

Figure 4.1 compares the behaviors of these interaction models, plotting u/ϵ_{ij} as a function of the scaled interparticle distance r/σ_{ij}. The main difference between these models is their behavior near the origin. The UF, IPL4, IPL6 and WCA models all diverge at the origin, yet at different rates. Whereas the UF model diverges only logarithmically, the IPL4, IPL6 and WCA force fields diverge according to the inverse powers r^{-4}, r^{-6} and r^{-12}, respectively. The GC, on the other hand, does not diverge at all as $r \to 0$, reaching a constant value at zero slope.

4.3 Results and Discussion

For all models we fix the energy scales of the interactions between particles of the same species to be $\epsilon_{AA} = 100\,\epsilon$ and $\epsilon_{BB} = 200\,\epsilon$, respectively, whereas ϵ_{AB} for inter-species interactions between A and B particles is variable. The length scale is chosen to be the same for all interaction types, i.e., $\sigma_{AA} = \sigma_{BB} = \sigma_{AB} = \sigma$. Furthermore, we consider symmetric binary mixtures in all cases, meaning that species A and B are present in equal proportions.

As a first case we consider the quench-simulation results for the binary mixture described by UF inter-particle model. [206–209] Figure 4.2 displays typical configurations

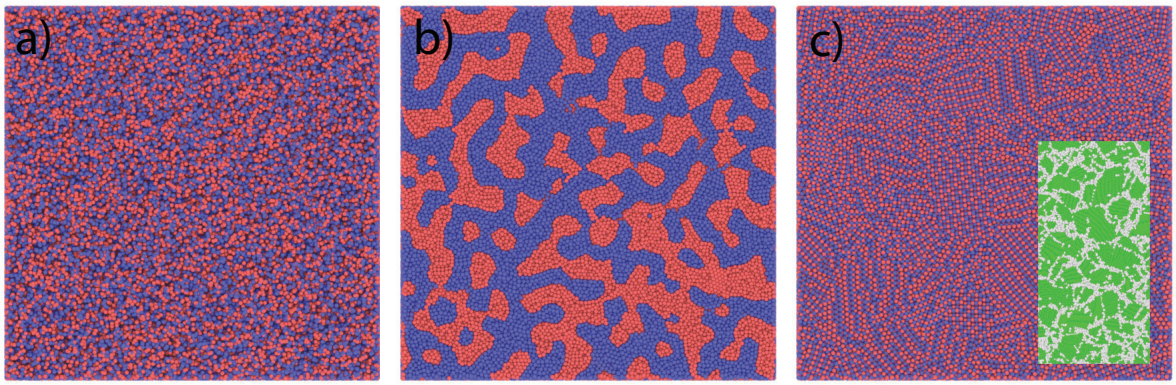

Figure 4.2: Typical configurations containing $N = 10^7$ particles, with the distinct species shown in blue and red, respectively, as obtained from the CG quench protocol for the binary UF model for two different values for the inter-species interaction energy scale. a) Infinite-temperature (i.e., ideal-gas) initial configuration. b) Phase-separating system for strong inter-species repulsion. c) Spontaneous ordering into a rock-salt (B1) type polycrystal of uniform composition. Inset displays part of the grain structure, with the green and white particles representing those in the B1 structure and in the disordered surroundings of the grain boundaries, respectively, as determined using the Ovito package. [97, 211]

obtained for the UF mixture containing 10^7 particles at a reduced particle density $\rho^* \equiv N\sigma^3/V = 1$. Figure 4.2a) depicts a typical random ideal-gas initial condition that is completely disordered, both chemically and structurally. Figures 4.2b) and c) then show snapshots obtained from the subsequent CG minimizations for two different values of the inter-species interaction parameter, ϵ_{AB}.

Fig. 4.2b) portrays a case of strong inter-species repulsion at $\epsilon_{AB} = 175\epsilon$. Under these conditions the initial ideal-gas phase undergoes a chemical ordering transition by which the two species unmix. Indeed, the depicted structure strongly resembles the typical patterns of spinodal decomposition often seen for phase separation. [199, 212, 213] Note, however, that the structure depicted in Fig. 4.2b) has not yet fully converged to the completely unmixed IS. This is because the computational cost to reach a fully unmixed state is prohibitively large for the system size considered here, even for efficient minimizers such as CG. For smaller system sizes, however ($N \sim 10^5 - 10^6$), complete unmixing is attained within reasonable computational limits.

For a weak inter-species interaction at $\epsilon_{AB} = 20\epsilon$, the decay phenomenon is fundamentally different. In this case the CG minimization rapidly converges to the IS displayed in Fig. 4.2c), which remains uniform with respect to chemical composition but

has spontaneously developed structural order. In particular, it features a polycrystalline morphology composed of grains with the rock-salt (B1) structure, which consists of two interpenetrating fcc lattices, each occupied by either A or B. Interestingly, the nature of this crystallization process is rather different from the usual equilibrium freezing phenomena, which occur by nucleation and growth. Here, the crystallization transition between the initial ideal-gas phase and the final polycrystalline structure is barrierless since they are connected by a CG sequence that always moves downhill on the PEL. [205]

A further interesting property is that the grain-size distribution reveals power-law characteristics, suggesting the existence of scale-invariant features in the polycrystalline IS. This is illustrated in Fig. 4.3, which depicts a log-log representation of the rank-size distribution [214, 215] of the grain sizes obtained for a 10^8-particle cell, such that the largest and smallest grains are ranked first and last, respectively. To identify the individual grains and determine their sizes we employed the recently developed grain-segmentation algorithm (GSA) in `Ovito`. [97, 211] The rank-size graph in Fig. 4.3 shows a manifest linear regime for grain sizes $\gtrsim 10^4$ particles, indicating that the grain-size distribution follows a power law asymptotically, indicating scale invariance. [214]

In all of the cases shown above, the results are independent of the random initial condition, displaying the same unmixing and crystallization processes for different random-number seeds. Accordingly, for a given particle-number density, the type of process that occurs is determined by the magnitude of the interspecies interaction strength ϵ_{AB} only. To further analyze its role we carry out a series of quench CG simulations for a set of ϵ_{AB}-values between 0 and $200\,\epsilon$, employing cells containing of the order of $10^3 - 10^4$ particles. In addition, we also investigate the possible influence of the particle-number density by considering a range of ρ^*-values for each ϵ_{AB}. To automate the detection of the unmixing and crystallization processes we monitor the displacements of the particles during each quench simulation, comparing their positions in the initially structureless state to those at the end of the CG minimization procedure. Fig. 4.4a) displays a density plot of the mean particle displacements (MPD) for the UF system as a function of ϵ_{AB} and ρ^*, expressed in units of the particle-density length scale

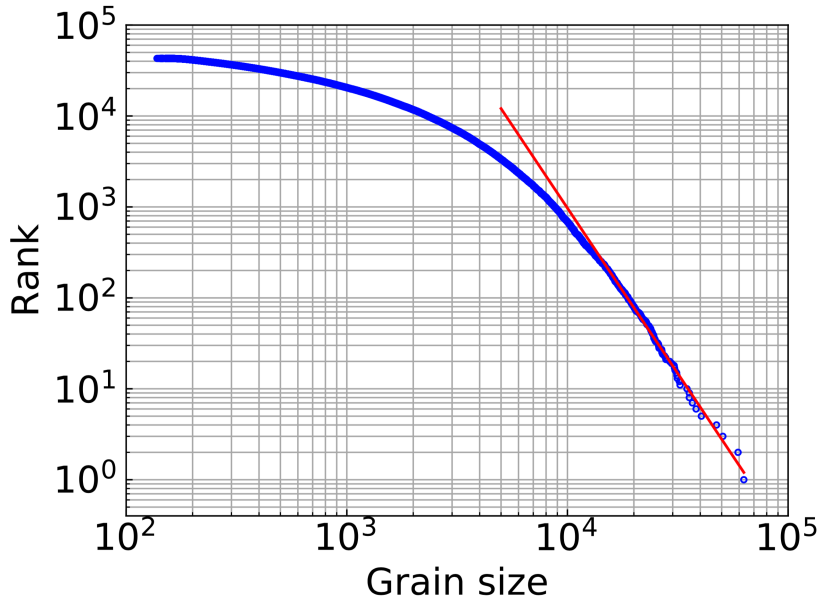

Figure 4.3: Log-log graph of rank-size representation of the grain size distribution for cell containing 10^8 particles as obtained using the grain-segmentation tool of the Ovito package [97, 211] , plotting the rank of each grain as a function of its size k such that the largest and smallest grains are ranked first and last, respectively. Blue circles depict results data points of individual grains. Red line represents a guide to the eye, obtained by a linear fit to the data for the 200 largest grains, giving a distribution $p(k) \sim k^{-\alpha}$ with $\alpha = 3.64 \pm 0.02$.

$d \equiv {\rho^*}^{-1/3}$. It displays three well-defined regimes, characterized by distinct values for the mean particle displacement. The yellow band on the left corresponds to values of the order of $\sim 2d$ and signals the decay of the initial ideal-gas configuration into the self-similar rock-salt structure. The mostly blue band on the right corresponds to the unmixing transition in which particles move over significantly larger distances. Finally, in the orange-colored areas the displacements are less than the average particle separation, meaning that the initial configurations are metastable, i.e., they are "close" to their corresponding local minima, which retain their chemically uniform and structurally disordered character. A further notable characteristic is that the identification of these 3 groups involves ϵ_{AB} only, being essentially independent of ρ^*, except for very low values for which the distances between the particles become large and the interactions between them weak. This implies that the ISs associated with high-temperature configurations are invariant with respect to uniform volume scaling. [203]

Interpreted from the perspective of the PEL formalism, [203] the above findings

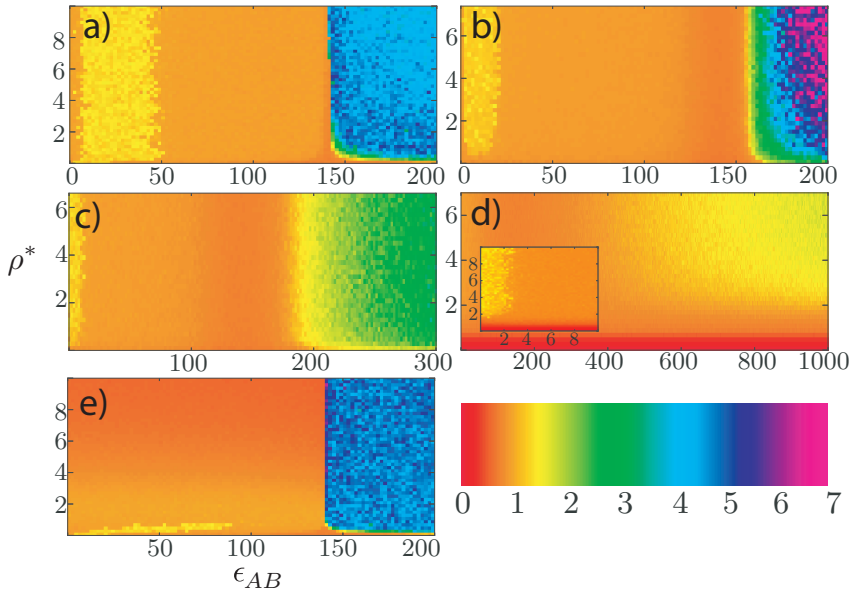

Figure 4.4: Density plots of mean particle displacement in units of the mean interparticle distance $d \equiv \rho^{*-1/3}$ during CG quench as a function of the interaction energy scale ϵ_{AB} and the reduced density ρ^* for the UF model (a), the IPL4 (b), IPL6 (c), WCA (d) and GC (e) potentials. Inset in (d) shows zoom into region with $\epsilon_{AB} < 10\epsilon$. Colors defined in the color bar distinguish between different displacement magnitudes.

imply that, for the considered binary UF model, the topography of the inherent structures for uniformly sampled ideal-gas configurations undergoes abrupt transitions as a function of the interspecies interaction intensity. At $\epsilon_{AB} \simeq 5$ and 50 there is an abrupt transition between chemically uniform, amorphous inherent structures and local minima that display polycrystalline structural order at a homogeneous composition. When reaching $\epsilon_{AB} \simeq 150$, on the other hand, there is a second kind of transition, with the nature of the inherent structures changing from chemically uniform and structurally ordered to compositionally unmixed without long-range structural order.

Depending of the magnitude of the inter-species energy scale, the random initial configuration for the UF model is unstable with respect to composition fluctuations, giving rise to the unmixing transition. This is illustrated in Fig. 4.5, which shows the mean energy obtained for 5000 random initial conditions as a function of composition at a reduced density $\rho^* = 1$ for a number of different values for ϵ_{AB}. For $\epsilon_{AB} \lesssim 140$, the energies are convex functions of the particle-type fraction, implying that the mixtures in these cases are stable. For $\epsilon_{AB} \gtrapprox 150$, on the other hand, the curves have become concave for any composition, implying that mixtures in any proportion of A and B species are unstable [216], giving rise to an unmixing transition.

Another important finding is that the observed phenomena are not limited to the binary UF system but seem to be universal for repulsive interaction potential-energy functions in general. This is illustrated in Figs. 4.4 b-e), which depict density plots of the mean particle distance for the inverse fourth-power law (IPL4), the inverse sixth-power law (IPL6), the Weeks-Chandler-Andersen (WCA) and the Gaussian core (GC) models described in Sec. 4.2.2, respectively. For all these systems the same 3 regimes can be identified, observing unmixing for large values for ϵ_{AB}, structural ordering to chemically uniform, rock-salt-type polycrystals for weak interspecies interactions and chemically/structurally amorphous configurations in between.

A particularly interesting issue in this context concerns the relation between the crystallization regime and the functional form of the repulsive interaction. Specifically, the shape and the extent of the structural ordering region in Fig. 4.4 is seen to correlate with the rate at which the potential-energy function diverges at the origin. Along the sequence shown in Fig. 4.4 a) to d), in which the divergence changes from slow (logarithmic) to fast (r^{-12}), as displayed in Fig. 4.1, the range of energy scales ϵ_{AB} for which crystallization occurs reduces systematically. Indeed, the role of the behavior of the pair potential at the origin in the ordering process becomes even more evident when considering the GC force field, which does not diverge at all, tending to a constant

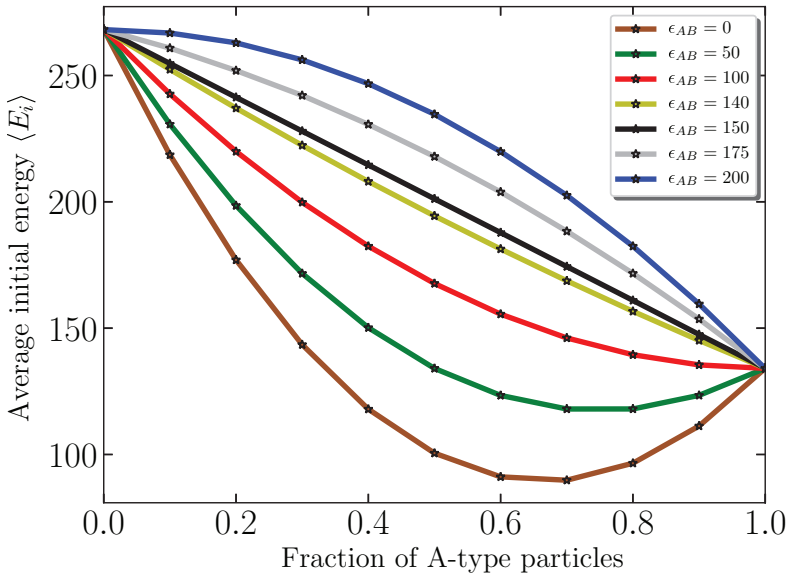

Figure 4.5: (Color online) Mean initial energy as a function of the A-particle fraction for different values of ϵ_{AB}.

value and zero derivative at the origin. As shown in Fig. 4.4 e), the decay to the rock-salt polycrystal structure in this case is restricted to a very narrow region in the $\epsilon_{AB} - \rho^*$ plane, disappearing altogether for densities above ~ 0.8.

Finally, the observed unmixing and crystallization phenomena closely resemble the two types of continuous non-equilibrium phase transition that are known to occur in mixtures such as metallic alloys. [198, 199] As discussed in detail in Ref. [199] such transitions start from an initial instability, meaning that any infinitesimal variation in, for instance, the chemical concentration or degree of crystallinity, lowers the free energy of the system, with spinodal decomposition and a number of structural order-disorder transitions as examples. The phenomena observed here are very similar to such behavior, with the spontaneous decay of infinite-temperature ideal-gas configurations into chemically or structurally ordered states, respectively. However, a formal classification of these phenomena in terms of such continuous nonequilibrium phase transitions also requires an analysis of the system's time-evolution, which, for such phenomena, is known to exhibit dynamical scaling properties. [198, 212, 213] Such an analysis requires modeling protocols that include system dynamics, which is inaccessible to the employed CG minimization protocol here.

4.4 Summary

In conclusion, we have considered nonequilibrium behavior of classical, 3-dimensional binary mixtures of particles interacting through purely repulsive forces during processes in which an infinite-temperature, ideal-gas initial structure is instantly quenched to zero temperature using conjugate-gradient minimization. We find that such systems display two different types of ordering process which can be controlled by tuning the interactions between unlike particles. Whereas strong inter-species repulsion giving rise to unmixing, weak interactions lead to a spontaneous development of structural order, forming a rock-salt-type polycrystalline solid of uniform composition. Furthermore, the findings suggest that the dual-type transition behavior is universal for repulsive pair interaction potential-energy functions in general, with the propensity for the crystallization processes being related to their behavior in the neighborhood of zero

separation. Finally, the observed phenomenology displays features that resemble the two kinds of continuous nonequilibrium phase transitions that are known to occur in mixtures such as metallic alloys. However, a formal classification of these phenomena in terms of such continuous nonequilibrium phase transitions also requires an analysis of the system's time-evolution, which is inaccessible to the minimization protocol employed here.

Chapter 5

Conclusions

In this chapter, we summarize the main conclusions from the work presented in this Thesis.

Although there are several models for the study of water through atomistic simulations, one must choose the model that best represents the phenomenon under study. Most models seek to improve the description of the behavior of liquid water across different phases, but have neglected the mechanical properties of crystalline and amorphous phases of water. This implies that the mechanical response of the many water models developed over the past decades are essentially unknown. In this Thesis, we investigated the mechanical response of ice I_h as described by two popular models, the all-atom TIP4P/Ice potential and the coarse-grained mW model, through two experiments of mechanical deformation. On one hand, we investigated the response under uniaxial deformations, aiming at the mechanical properties of the bulk. On the other hand, we investigated the mechanical properties of the surface through the nanoindentation process.

Even though the employed strain rates are substantially higher than those used in typical laboratory experiments, and direct quantitative comparison is inconceivable, the obtained results provide valuable insight into the intrinsic mechanical behavior of the two water models. Young's modulus for both models are consistent with experimental data and the steady-state hardness for both models were found to be consistent with

experimental AFM reports, giving values that are of the same order of magnitude.

On the other hand, whether or not protons (hydrogens) are explicitly included in the water models leads to a totally different mechanical response. In particular, for the monoatomic model mW, in the absence of explicit protons there are anomalous behaviors such as recrystallization, nucleation and motion of lattice dislocations and unknown phase transitions. This means that the description of the hydrogen bond (HB) in the mW model does not capture its fundamental asymmetry, with one molecule donating a proton while the other acts as acceptor. Thus, while ignoring HB asymmetry does not seem to prevent the mW model from properly reproducing various thermodynamic properties of water and ice, it does not capture the essence of the kinetic processes involved in breaking and reforming HB. This is due to a different time scale in the formation of the HB. For if we break one of these bonds, the molecule must rotate to form another bond. In silicon, for example, where there are no hydrogen atoms, this type of bonds is easier and takes much less time. Therefore, this lack of explicit protons makes the HB reforming easier, thus facilitating phenomena such as nucleation and movement of displacements and recrystallization. Thus, the TIP4P/Ice model, which explicitly considers hydrogen atoms, works best to describe this type of mechanical deformations.

Finally, repulsive pair potentials are very useful in the study of soft-matter materials such as polymers and colloids. Although there is an extensive study of equilibrium phase behavior of such models, nonequilibrium phenomena, have received much less attention. In this Thesis, we investigated the nonequilibrium behavior of classical, 3-dimensional binary mixtures of particles interacting through purely repulsive forces during processes in which an infinite-temperature, ideal-gas initial structure is instantly quenched to zero temperature using conjugate-gradient minimization.

We find that such systems display two different types of ordering process which can be controlled by tuning the interactions between unlike particles. Whereas strong inter-species repulsion giving rise to unmixing, weak interactions lead to a spontaneous development of structural order, forming a rock-salt-type polycrystalline solid of uniform composition. Furthermore, the findings suggest that the dual-type transition behavior is universal for repulsive pair interaction potential-energy functions in general, with the propensity for the crystallization processes being related to their

behavior in the neighborhood of zero separation.

Finally, the observed unmixing and crystallization phenomena closely resemble the two types of continuous non-equilibrium phase transition that are known to occur in mixtures such as metallic alloys. When considering nonequilibrium processes in which an initial high-temperature state is suddenly quenched to low temperature, there can be two types of continuous nonequilibrium phase transition. By analyzing the minimization process, we can establish unequivocally that they are fundamentally different from discontinuous (first order) transitions, with the process being barrierless. However, an analysis of the temporal evolution of the system is necessary to establish a formal classification of these phenomena in terms of continuous nonequilibrium phase transition.

5.1 Future perspectives

To continue the study of the mechanical properties of ice I_h, the next step should seek to understand how mechanical deformation occurs in polycrystalline ice, which will be of great importance to understand real phenomena that occur in large ice masses, such as in the flow of glaciers.

A the next step in the study of nonequilibrium processes of repulsive binary mixtures, is to study the dynamics of the observed transitions in order to be able to analyze in a formal way dynamic scaling. In particular, the continuous nature of the phase transitions is related to two properties: [198]

a) In contrast to discontinuous (first-order) transitions, the process is barrierless.

b) The time-development of structure (for instance, the length scale $L(t)$ of A and B-type domains in the unmixing transition) shows dynamical scaling of the form $L \sim t^{1/z}$, where z is a dynamical exponent.

This second property is what distinguishes a nonequilibrium continuous phase transition from a "normal" equilibrium continuous phase transition in which

scaling properties appear in thermodynamic equilibrium properties. Formally defining these types of transitions is important since, to date, a continuous system presenting the two types of continuous nonequilibrium phase transitions (unmixing and crystallization) has never been observed.

References

1. Allen, M. P. & Tildesley, D. J. *Computer simulation of liquids* (Oxford university press, 1989) (Cited on pages 21, 31).
2. Newman, M. E. J. & Barkema, G. T. *Monte Carlo methods in statistical physics* (Clarendon Press Oxford, 1999) (Cited on page 22).
3. Tuckerman, M. *Statistical mechanics: theory and molecular simulation* (Oxford University Press, 2010) (Cited on pages 22, 30).
4. Frenkel, D. & Smit, B. *Understanding molecular simulation: from algorithms to applications* (Academic press, 2001) (Cited on pages 22, 30).
5. Papon, P., Leblond, J., Meijer, P. H. E. & Schnur, S. L. *The physics of phase transitions* (Springer, 2002) (Cited on page 22).
6. Rapaport, D. C. *The art of molecular dynamics simulation* (Cambridge university press, 2004) (Cited on page 22).
7. Fermi, E., Pasta, J. & Ulam, S. Studies of nonlinear problems. *Los Alamos Report LA-1940* **978** (1955) (Cited on page 23).
8. Alder, B. J. & Wainwright, T. E. Phase transition for a hard sphere system. *The Journal of chemical physics* **27,** 1208 (1957) (Cited on page 23).
9. Alder, B. J. & Wainwright, T. E. Studies in molecular dynamics. I. General method. *The Journal of Chemical Physics* **31,** 459–466 (1959) (Cited on page 23).
10. Rahman, A. Correlations in the motion of atoms in liquid argon. *Physical Review* **136,** A405 (1964) (Cited on page 23).

11. Verlet, L. Computer "experiments" on classical fluids. I. Thermodynamical properties of Lennard-Jones molecules. *Physical review* **159,** 98 (1967) (Cited on pages 23, 30).

12. Stillinger, F. H. & Rahman, A. Improved simulation of liquid water by molecular dynamics. *The Journal of Chemical Physics* **60,** 1545–1557 (1974) (Cited on page 23).

13. Stillinger, F. H. & Weber, T. A. Computer simulation of local order in condensed phases of silicon. *Phys. Rev. B* **31,** 5262–5271 (1985) (Cited on pages 26, 27, 42).

14. Abascal, J. L. F., Sanz, E., García Fernández, R. & Vega, C. A potential model for the study of ices and amorphous water: TIP4P/Ice. *J. Chem. Phys.* **122,** 234511 (2005) (Cited on pages 27, 41, 42, 58, 59).

15. Molinero, V. & Moore, E. B. Water Modeled As an Intermediate Element between Carbon and Silicon. *J. Phys. Chem. B* **113,** 4008–4016 (2009) (Cited on pages 27, 28, 41, 42, 55, 58, 59).

16. *ISAACS program (Interactive Structure Analysis of Amorphous and Crystalline Systems)* Available at `http://isaacs.sourceforge.net/phys/pbc.html`. Central Michigan University (2010) (Cited on page 29).

17. Hockney, R. W. *Computer Simulation Using Particles* (Taylor & Francis Group, 2017) (Cited on pages 29, 44, 60).

18. Goldstein, H., Poole, C. P. & Safko, J. L. *Classical mechanics* 3ra Ed. (Adsison-Wesley, 2001) (Cited on page 30).

19. Swope, W. C., Andersen, H. C., Berens, P. H. & Wilson, K. R. A computer simulation method for the calculation of equilibrium constants for the formation of physical clusters of molecules: Application to small water clusters. *The Journal of Chemical Physics* **76,** 637–649 (1982) (Cited on page 30).

20. Kubo, R. The fluctuation-dissipation theorem. *Reports on progress in physics* **29,** 255 (1966) (Cited on page 32).

21. Bussi, G. & Parrinello, M. Accurate sampling using Langevin dynamics. *Physical Review E* **75,** 056707 (2007) (Cited on page 32).

22. Boltzmann, L. *Lectures on Gas Theory. Translated, together with (Boltzmann 1896) by S. G. Brush* (University of California Press, 1964) (Cited on page 33).

23. Petrenko, V. F. & Whitworth, R. W. *Physics of ice* (Oxford University Press, New York, 1999) (Cited on pages 34, 40, 43, 48, 55).

24. Bartels-Rausch, T. *et al.* Ice structures, patterns, and processes: A view across the icefields. *Rev. Mod. Phys.* **84,** 885–944 (2012) (Cited on page 34).

25. Benedict, W. S., Gailar, N. & Plyler, E. K. Rotation-Vibration Spectra of Deuterated Water Vapor. *The Journal of Chemical Physics* **24,** 1139–1165 (1956) (Cited on page 35).

26. *The Structure and Entropy of Ice* Available at http://mini.physics.sunysb.edu/~marivi/TEACHING-OLD/PHY313/doku.php?id=lectures:4. Stony Brook University (2011) (Cited on pages 36, 37).

27. Silva Junior, D. L. & de Koning, M. Structure and energetics of extended defects in ice I_h. *Phys. Rev. B* **85,** 024119 (2 2012) (Cited on pages 36, 41).

28. Bernal, J. & Fowler, R. A theory of water and ionic solution, with particular reference to hydrogen and hydroxyl ions. *J. Chem. Phys.* **1,** 515–548 (1933) (Cited on page 37).

29. Pauling, L. The Structure and Entropy of Ice and of Other Crystals with Some Randomness of Atomic Arrangement. *J. Am. Chem. Soc.* **57,** 2680–2684 (1935) (Cited on page 37).

30. Bjerrum, N. Structure and Properties of Ice. *Science* **115,** 385 (1952) (Cited on page 37).

31. Kuhs, W. F. & Lehmann, M. S. The structure of the ice Ih by neutron diffraction. *The Journal of Physical Chemistry* **87,** 4312–4313 (1983) (Cited on page 37).

32. Schulson, E. M. The structure and mechanical behavior of ice. *JOM* **51,** 21–27 (1999) (Cited on page 40).

33. Schulson, E. & Duval, P. *Creep and fracture of ice* (Cambridge University Press, 2009) (Cited on page 40).

34. Reusch, E. Beiträge zur Lehre vom Eis. *Ann. Phys.* **197,** 573–578 (1864) (Cited on page 41).

35. Glen, J. & Perutz, M. The growth and deformation of ice crystals. *J. Glaciol.* **2,** 397–403 (1954) (Cited on page 41).

36. Currier, J. & Schulson, E. The tensile strength of ice as a function of grain size. *Acta Metall.* **30,** 1511–1514 (1982) (Cited on page 41).

37. Lange, M. A. & Ahrens, T. J. The dynamic tensile strength of ice and ice-silicate mixtures. *J. Geophys. Res. Solid Earth* **88,** 1197–1208 (1983) (Cited on page 41).

38. Andrews, R. Measurement of the fracture toughness of glacier ice. *J. Glaciol.* **31,** 171–176 (1985) (Cited on page 41).

39. Jones, S. J. High Strain-Rate Compression Tests on Ice. *J. Phys. Chem. B* **101,** 6099–6101 (1997) (Cited on page 41).

40. Dempsey, J., Adamson, R. & Mulmule, S. Scale effects on the in-situ tensile strength and fracture of ice. Part II: First-year sea ice at Resolute, NWT. *Int. J. Fract.* **95,** 347 (1999) (Cited on page 41).

41. Schulson, E. M. Brittle failure of ice. *Eng. Fract. Mech.* **68,** 1839–1887 (2001) (Cited on page 41).

42. Jones, S. J., Gagnon, R. E., Derradji, A. & Bugden, A. Compressive strength of iceberg ice. *Can. J. Phys.* **81,** 191–200 (2003) (Cited on page 41).

43. Dutta, P. K., Cole, D. M., Schulson, E. M., Sodhi, D. S., *et al.* A fracture study of ice under high strain rate loading. *Int. J. Offshore Polar Eng.* **14,** 182–188 (2004) (Cited on page 41).

44. Kim, H. & Keune, J. N. Compressive strength of ice at impact strain rates. *J. Mater. Sci.* **42,** 2802 (2007) (Cited on page 41).

45. Shazly, M., Prakash, V. & Lerch, B. A. High strain-rate behavior of ice under uniaxial compression. *Int. J. Solids Struct.* **46,** 1499–1515 (2009) (Cited on page 41).

46. Combescure, A., Chuzel-Marmot, Y. & Fabis, J. Experimental study of high-velocity impact and fracture of ice. *Int. J. Solids Struct.* **48,** 2779–2790 (2011) (Cited on page 41).

47. Sain, T. & Narasimhan, R. Constitutive modeling of ice in the high strain rate regime. *Int. J. Solids Struct.* **48,** 817–827 (2011) (Cited on page 41).

48. Wu, X. & Prakash, V. Dynamic compressive behavior of ice at cryogenic temperatures. *Cold Reg. Sci. Technol.* **118,** 1–13 (2015) (Cited on pages 41, 44).

49. Pernas-Sánchez, J., Pedroche, D., Varas, D., López-Puente, J. & Zaera, R. Numerical modeling of ice behavior under high velocity impacts. *Int. J. Solids Struct.* **49,** 1919–1927 (2012) (Cited on page 41).

50. Pernas-Sánchez, J., Artero-Guerrero, J. A., Varas, D. & López-Puente, J. Analysis of Ice Impact Process at High Velocity. *Exp. Mech.* **55,** 1669–1679 (2015) (Cited on page 41).

51. Qi, C., Lian, J., Ouyang, Q. & Zhao, X. Dynamic Compressive Strength and Failure of Natural Lake Ice Under Moderate Strain Rates at Near Melting Point Constant-Temperature. en. *Lat. Am. J. Solids Struct.* **14,** 1669–1694 (2017) (Cited on page 41).

52. Ahmad, S., Ohtomo, M. & Whitworth, R. W. Observation of a dislocation source in ice by synchrotron radiation topography. *Nature* **319,** 659 (1986) (Cited on page 41).

53. Ahmad, S. & Whitworth, R. W. Dislocation motion in ice: A study by synchrotron X-ray topography. *Philos. Mag. A* **57,** 749–766 (1988) (Cited on page 41).

54. Shearwood, C. & Whitworth, R. W. The velocity of dislocations in ice. *Philos. Mag. A* **64,** 289–302 (1991) (Cited on page 41).

55. Shearwood, C. & Whitworth, R. Novel processes of dislocation multiplication observed in ice. *Acta Metall. Mater.* **41,** 205–210 (1993) (Cited on page 41).

56. Kacher, J. & Robertson, I. M. In situ TEM characterisation of dislocation interactions in α-titanium. *Philos. Mag.* **96,** 1437–1447 (2016) (Cited on page 41).

57. Zepeda-Ruiz, L. A., Stukowski, A., Oppelstrup, T. & Bulatov, V. V. Probing the limits of metal plasticity with molecular dynamics simulations. *Nature* **550,** 492 (2017) (Cited on pages 41, 58).

58. Duesbery, M. S. & Richardson, G. Y. The dislocation core in crystalline materials. *Crit. Rev. Solid State Mater. Sci.* **17,** 1–46 (1991) (Cited on page 41).

59. Bulatov, V. V. *et al.* Parameter-free modelling of dislocation motion: The case of silicon. *Philos. Mag. A* **81,** 1257–1281 (2001) (Cited on page 41).

60. Mishima, O. & Stanley, H. E. The relationship between liquid, supercooled and glassy water. *Nature* **396,** 329–335 (1998) (Cited on page 41).

61. Vega, C., Abascal, J. L. F., Sanz, E., MacDowell, L. G. & McBride, C. Can simple models describe the phase diagram of water? *J. Phys.: Condens. Matter* **17,** S3283 (2005) (Cited on pages 41, 42).

62. García Fernández, R., Abascal, J. L. F. & Vega, C. The melting point of ice Ih for common water models calculated from direct coexistence of the solid-liquid interface. *J. Chem. Phys.* **124,** 144506 (2006) (Cited on page 41).

63. Vega, C., Sanz, E., Abascal, J. L. F. & Noya, E. G. Determination of phase diagrams via computer simulation: methodology and applications to water, electrolytes and proteins. *J. Phys.: Condens. Matter* **20,** 153101– (2008) (Cited on page 41).

64. Handel, R., Davidchack, R. L., Anwar, J. & Brukhno, A. Direct calculation of solid-liquid interfacial free energy for molecular systems: TIP4P ice-water interface. *Phys. Rev. Lett.* **100,** 036104 (2008) (Cited on pages 41, 42).

65. Liu, Y., Panagiotopoulos, A. Z. & Debenedetti, P. G. Low-temperature fluid-phase behavior of ST2 water. *J. Chem. Phys.* **131,** 104508–7 (2009) (Cited on page 41).

66. MacDowell, L. G. & Vega, C. Dielectric Constant of Ice Ih and Ice V: A Computer Simulation Study. *J. Phys. Chem. B* **114,** 6089 (2010) (Cited on page 41).

67. Kastelowitz, N., Johnston, J. C. & Molinero, V. The anomalously high melting temperature of bilayer ice. *J. Chem. Phys.* **132,** 124511 (2010) (Cited on pages 41, 42).

68. Aragones, J. L., MacDowell, L. G. & Vega, C. Dielectric Constant of Ices and Water: A Lesson about Water Interactions. *J. Phys. Chem. A* **115,** 5745–5758 (2011) (Cited on page 41).

69. Limmer, D. T. & Chandler, D. The putative liquid-liquid transition is a liquid-solid transition in atomistic models of water. *J. Chem. Phys.* **135,** 134503–10 (2011) (Cited on page 41).

70. Moore, E. B. & Molinero, V. Structural transformation in supercooled water controls the crystallization rate of ice. *Nature* **479,** 506–508 (2011) (Cited on pages 41, 42).

71. Moore, E. B. & Molinero, V. Is it cubic? Ice crystallization from deeply supercooled water. *Phys. Chem. Chem. Phys.* **13,** 20008–20016 (2011) (Cited on pages 41, 42).

72. Johnston, J. C. & Molinero, V. Crystallization, melting, and structure of water nanoparticles at atmospherically relevant temperatures. *J. Am. Chem. Soc.* **134,** 6650–6659 (2012) (Cited on pages 41, 42).

73. Liu, Y., Palmer, J. C., Panagiotopoulos, A. Z. & Debenedetti, P. G. Liquid-liquid transition in ST2 water. *J. Chem. Phys.* **137,** 214505–10 (2012) (Cited on page 41).

74. Shepherd, T. D., Koc, M. A. & Molinero, V. The Quasi-Liquid Layer of Ice under Conditions of Methane Clathrate Formation. *J. Phys. Chem. C* **116,** 12172–12180 (2012) (Cited on page 41).

75. Limmer, D. T. & Chandler, D. The putative liquid-liquid transition is a liquid-solid transition in atomistic models of water. II. *J. Chem. Phys.* **138,** 214504–15 (2013) (Cited on page 41).

76. Sanz, E. *et al.* Homogeneous Ice Nucleation at Moderate Supercooling from Molecular Simulation. *J. Am. Chem. Soc.* **135,** 15008–15017 (2013) (Cited on page 41).

77. Nguyen, A. H. & Molinero, V. Identification of Clathrate Hydrates, Hexagonal Ice, Cubic Ice, and Liquid Water in Simulations: the CHILL+ Algorithm. *J. Phys. Chem. B* **119,** 9369–9376 (2015) (Cited on pages 41, 64, 65).

78. Zaragoza, A. *et al.* Competition between ices Ih and Ic in homogeneous water freezing. *J. Chem. Phys.* **143,** 134504 (2015) (Cited on pages 41, 42).

79. Cisneros, G. A. *et al.* Modeling Molecular Interactions in Water: From Pairwise to Many-Body Potential Energy Functions. *Chem. Rev.* **116,** 7501–7528 (2016) (Cited on page 41).

80. Espinosa, J. R. *et al.* Interfacial Free Energy as the Key to the Pressure-Induced Deceleration of Ice Nucleation. *Phys. Rev. Lett.* **117,** 135702– (2016) (Cited on pages 41, 42).

81. Espinosa, J. R., Navarro, C., Sanz, E., Valeriani, C. & Vega, C. On the time required to freeze water. *J. Chem. Phys.* **145,** 211922 (2016) (Cited on pages 41, 42).

82. Espinosa, J. R., Vega, C. & Sanz, E. Ice-Water Interfacial Free Energy for the TIP4P, TIP4P/2005, TIP4P/Ice, and mW Models As Obtained from the Mold Integration Technique. *J. Phys. Chem. C* **120,** 8068–8075 (2016) (Cited on pages 41, 42).

83. Lupi, L. *et al.* Role of stacking disorder in ice nucleation. *Nature* **551,** 218– (2017) (Cited on pages 41, 42, 49).

84. Wu, J. *et al.* Mechanical instability of monocrystalline and polycrystalline methane hydrates. *Nat. Commun.* **6,** 8743 (2015) (Cited on page 41).

85. Min, S. H. & Berkowitz, M. L. A comparative computational study of coarse-grained and all-atom water models in shock Hugoniot states. *J. Chem. Phys.* **148,** 144504 (2018) (Cited on page 41).

86. Jorgensen, W. L. & Madura, J. D. Temperature and size dependence for Monte Carlo simulations of TIP4P water. *Mol. Phys.* **56,** 1381–1392 (1985) (Cited on page 42).

87. Hayward, J. A. & Reimers, J. R. Unit cells for the simulation of hexagonal ice. *J. Chem. Phys.* **106,** 1518–1529 (1997) (Cited on page 42).

88. Rahman, A. & Stillinger, F. H. Proton Distribution in Ice and the Kirkwood Correlation Factor. *J. Chem. Phys.* **57,** 4009–4017 (1972) (Cited on page 43).

89. Plimpton, S. Fast Parallel Algorithms for Short-Range Molecular Dynamics. *J. Comput. Phys.* **117,** 1–19 (1995) (Cited on pages 43, 60, 81).

90. Parrinello, M. & Rahman, A. Polymorphic transitions in single crystals: A new molecular dynamics method. *J. Appl. Phys.* **52,** 7182–7190 (1981) (Cited on pages 43, 60).

91. Martyna, G. J., Tobias, D. J. & Klein, M. L. Constant pressure molecular dynamics algorithms. *J. Chem. Phys.* **101,** 4177–4189 (1994) (Cited on pages 43, 60).

92. Shinoda, W., Shiga, M. & Mikami, M. Rapid estimation of elastic constants by molecular dynamics simulation under constant stress. *Phys. Rev. B* **69,** 134103– (2004) (Cited on pages 43, 60).

93. Schneider, T. & Stoll, E. Molecular-dynamics study of a three-dimensional one-component model for distortive phase transitions. *Phys. Rev. B* **17,** 1302–1322 (1978) (Cited on pages 43, 60).

94. Ryckaert, J.-P., Ciccotti, G. & Berendsen, H. J. Numerical integration of the cartesian equations of motion of a system with constraints: molecular dynamics of n-alkanes. *J. Comput. Phys.* **23,** 327–341 (1977) (Cited on pages 44, 60).

95. Gammon, P. H., Kiefte, H. & Clouter, M. J. Elastic constants of ice samples by Brillouin spectroscopy. *J. Phys. Chem.* **87,** 4025–4029 (1983) (Cited on page 46).

96. Maras, E., Trushin, O., Stukowski, A., Ala-Nissila, T. & Jönsson, H. Global transition path search for dislocation formation in Ge on Si(001). *Comput. Phys. Commun.* **205,** 13–21 (2016) (Cited on pages 46, 63, 64, 68).

97. Stukowski, A. Visualization and analysis of atomistic simulation data with OVITO: the Open Visualization Tool. *Model. Simul. Mater. Sci. Eng.* **18,** 015012– (2010) (Cited on pages 46, 63, 84–86).

98. Stukowski, A., Bulatov, V. V. & Arsenlis, A. Automated identification and indexing of dislocations in crystal interfaces. *Modell. Simul. Mater. Sci. Eng.* **20,** 085007– (2012) (Cited on pages 47, 53).

99. Berghezan, A., Fourdeux, A. & Amelinckx, S. Transmission electron microscopy studies of dislocations and stacking faults in a hexagonal metal: Zinc. *Acta Metall.* **9,** 464–490 (1961) (Cited on page 47).

100. Hull, D. & Bacon, D. *Introduction to dislocations* (Butterworth-Heinemann, 2001) (Cited on pages 47, 53).

101. Rist, M. A. High-Stress Ice Fracture and Friction. *J. Phys. Chem. B* **101,** 6263–6266 (1997) (Cited on page 55).

102. Glen, J. The effect of hydrogen disorder on dislocation movement and plastic deformation of ice. *Z. Phys. B Con. Mat.* **7,** 43–51 (1 1968) (Cited on page 55).

103. Oliver, W. C. & Pharr, G. M. Measurement of hardness and elastic modulus by instrumented indentation: Advances in understanding and refinements to methodology. *J. Mater. Res.* **19,** 3–20 (2004) (Cited on page 57).

104. Fischer-Cripps, A. C. *Nanoindentation* (Springer New York, 2011) (Cited on pages 57, 73, 74).

105. Gouldstone, A. *et al.* Indentation across size scales and disciplines: Recent developments in experimentation and modeling. *Acta Mater.* **55,** 4015–4039 (2007) (Cited on page 57).

106. Fischer-Cripps, A. C. A simple phenomenological approach to nanoindentation creep. *Mater. Sci. Eng. A* **385,** 74–82 (2004) (Cited on page 57).

107. Harding, D., Oliver, W. & Pharr, G. Cracking during nanoindentation and its use in the measurement of fracture toughness. *MRS Online Proceedings Library Archive* **356** (1994) (Cited on page 57).

108. Volinsky, A. A., Vella, J. B. & Gerberich, W. W. Fracture toughness, adhesion and mechanical properties of low-K dielectric thin films measured by nanoindentation. *Thin Solid Films* **429,** 201–210 (2003) (Cited on page 57).

109. Yang, B., Riester, L. & Nieh, T. Strain hardening and recovery in a bulk metallic glass under nanoindentation. *Scr Mater* **54,** 1277–1280 (2006) (Cited on page 57).

110. Domnich, V., Gogotsi, Y. & Dub, S. Effect of phase transformations on the shape of the unloading curve in the nanoindentation of silicon. *Appl. Phys. Lett.* **76,** 2214–2216 (2000) (Cited on page 57).

111. Ebenstein, D. M. & Pruitt, L. A. Nanoindentation of biological materials. *Nano Today* **1,** 26–33 (2006) (Cited on page 57).

112. Li, Y. & Somorjai, G. A. Surface Premelting of Ice. *J. Phys. Chem. C* **111,** 9631–9637 (2007) (Cited on pages 57, 74).

113. Petrenko, V. F. Study of the Surface of Ice, Ice/Solid and Ice/Liquid Interfaces with Scanning Force Microscopy. *J. Phys. Chem. B* **101,** 6276–6281 (1997) (Cited on pages 57, 59, 77).

114. Slater, B. & Michaelides, A. Surface premelting of water ice. *Nature Reviews Chemistry* **3,** 172–188 (2019) (Cited on page 57).

115. Döppenschmidt, A., Kappl, M. & Butt, H.-J. Surface Properties of Ice Studied by Atomic Force Microscopy. *J. Phys. Chem. B* **102,** 7813–7819 (1998) (Cited on pages 58, 72).

116. Döppenschmidt, A. & Butt, H.-J. Measuring the Thickness of the Liquid-like Layer on Ice Surfaces with Atomic Force Microscopy. *Langmuir* **16,** 6709–6714 (2000) (Cited on pages 58, 59, 72, 77).

117. Butt, H.-J., Döppenschmidt, A., Hüttl, G., Müller, E. & Vinogradova, O. I. Analysis of plastic deformation in atomic force microscopy: Application to ice. *J. Chem. Phys.* **113,** 1194–1203 (2000) (Cited on pages 58, 59, 63, 74, 76, 77).

118. Pittenger, B. *et al.* Premelting at ice-solid interfaces studied via velocity-dependent indentation with force microscope tips. *Phys. Rev. B* **63,** 134102– (2001) (Cited on pages 58, 59, 63, 72, 74, 76, 77).

119. Gelman Constantin, J., Gianetti, M. M., Longinotti, M. P. & Corti, H. R. The quasi-liquid layer of ice revisited: the role of temperature gradients and tip chemistry in AFM studies. *Atmos. Chem. Phys.* **18,** 14965–14978 (2018) (Cited on pages 58, 59, 76, 77).

120. Santos-Flórez, P. A., Ruestes, C. J. & de Koning, M. Uniaxial-deformation behavior of ice Ih as described by the TIP4P/Ice and mW water models. *J. Chem. Phys.* **149,** 164711 (2018) (Cited on pages 58, 59, 71, 72).

121. Valencia, F. *et al.* Mechanical Properties Obtained by Indentation of Hollow Pd Nanoparticles. *J. Phys. Chem. C* **122,** 25035–25042 (2018) (Cited on pages 58, 67).

122. Landman, U., Luedtke, W. D., Burnham, N. A. & Colton, R. J. Atomistic Mechanisms and Dynamics of Adhesion, Nanoindentation, and Fracture. *Science* **248,** 454–461 (1990) (Cited on page 58).

123. Luan, B. & Robbins, M. O. The breakdown of continuum models for mechanical contacts. *Nature* **435,** 929 (2005) (Cited on page 58).

124. Szlufarska, I. Atomistic simulations of nanoindentation. *Mater. Today* **9,** 42–50 (2006) (Cited on page 58).

125. Szlufarska, I., Chandross, M. & Carpick, R. W. Recent advances in single-asperity nanotribology. *J. Phys. D: Appl. Phys.* **41,** 123001 (2008) (Cited on page 58).

126. Ruestes, J. C., Alhafez, A. I. & Urbassek, M. H. Atomistic Studies of Nanoindentation–A Review of Recent Advances. *Crystals* **7** (2017) (Cited on pages 58, 63).

127. Chavoshi, S. Z. & Xu, S. Nanoindentation/scratching at finite temperatures: Insights from atomistic-based modeling. *Prog. Mater Sci.* **100,** 1–20 (2019) (Cited on page 58).

128. Gelman Constantin, J., Carignano, M. A., Corti, H. R. & Szleifer, I. Molecular Dynamics Simulation of Ice Indentation by Model Atomic Force Microscopy Tips. *J. Phys. Chem. C* **119,** 27118–27124 (2015) (Cited on pages 58, 59, 69, 71).

129. Franco Pinheiro Moreira, P. A., Gomes de Aguiar Veiga, R. & de Koning, M. Elastic constants of ice Ih as described by semi-empirical water models. *J. Chem. Phys.* **150,** 044503 (2019) (Cited on page 59).

130. Yeh, I.-C. & Berkowitz, M. L. Ewald summation for systems with slab geometry. *J. Chem. Phys.* **111,** 3155–3162 (1999) (Cited on page 60).

131. Conde, M. M., Vega, C. & Patrykiejew, A. The thickness of a liquid layer on the free surface of ice as obtained from computer simulation. *J. Chem. Phys.* **129,** 014702 (2008) (Cited on pages 62, 65).

132. Limmer, D. T. & Chandler, D. Premelting, fluctuations, and coarse-graining of water-ice interfaces. *The Journal of Chemical Physics* **141,** 18C505 (2014) (Cited on pages 62, 65).

133. Louden, P. B. & Gezelter, J. D. Why is Ice Slippery? Simulations of Shear Viscosity of the Quasi-Liquid Layer on Ice. *J. Phys. Chem. Lett.* **9,** 3686–3691 (2018) (Cited on pages 62, 65).

134. Hudait, A., Allen, M. T. & Molinero, V. Sink or Swim: Ions and Organics at the Ice-Air Interface. *J. Am. Chem. Soc.* **139,** 10095–10103 (2017) (Cited on pages 62, 65).

135. Qiu, Y. & Molinero, V. Why Is It So Difficult to Identify the Onset of Ice Premelting? *J. Phys. Chem. Lett.* **9,** 5179–5182 (2018) (Cited on pages 62, 65).

136. Pickering, I., Paleico, M., Sirkin, Y. A. P., Scherlis, D. A. & Factorovich, M. H. Grand Canonical Investigation of the Quasi Liquid Layer of Ice: Is It Liquid? *J. Phys. Chem. B* **122,** 4880–4890 (2018) (Cited on pages 62, 65).

137. Kelchner, C. L., Plimpton, S. J. & Hamilton, J. C. Dislocation nucleation and defect structure during surface indentation. *Phys. Rev. B* **58,** 11085–11088 (1998) (Cited on pages 62, 67).

138. Hertz, H. Ueber die Berührung fester elastischer Körper. ger. *Journal für die reine und angewandte Mathematik* **92,** 156–171 (1882) (Cited on page 63).

139. Ruestes, C. J., Schwen, D., Millán, E. N., Aparicio, E. & Bringa, E. M. Mechanical properties of Au foams under nanoindentation. *Comp. Mater. Sci.* **147,** 154–167 (2018) (Cited on page 67).

140. Ruestes, C. J., Anders, C., Bringa, E. M. & Urbassek, H. M. Nanoindentation tests of heavy-ion-irradiated Au foams - molecular dynamics simulation. *J. Appl. Phys.* **123,** 225903 (2018) (Cited on page 67).

141. Guo, Q., Ghaani, M. R., Nandi, P. K. & English, N. J. Pressure-Induced Densification of Ice Ih under Triaxial Mechanical Compression: Dissociation versus Retention of Crystallinity for Intermediate States in Atomistic and Coarse-Grained Water Models. *J. Phys. Chem. Lett.* **9,** 5267–5274 (2018) (Cited on page 72).

142. Butkovich, T. R. *Hardness of single ice crystals* (Snow, Ice and Permafrost Research Establishment, Corps of Engineers, US Army, 1954) (Cited on page 76).

143. Vishnubhotla, S. B. *et al.* Matching Atomistic Simulations and In Situ Experiments to Investigate the Mechanics of Nanoscale Contact. *Tribol. Lett.* **67,** 97 (2019) (Cited on page 78).

144. Landman, U., Luedtke, W., Burnham, N. A. & Colton, R. J. Atomistic mechanisms and dynamics of adhesion, nanoindentation, and fracture. *Science* **248,** 454–461 (1990) (Cited on page 78).

145. Stillinger, F. H. & Helfand, E. Critical Solution Behavior in a Binary Mixture of Gaussian Molecules. *J. Chem. Phys.* **41,** 2495–2502 (1964) (Cited on page 79).

146. Helfand, E. & Stillinger, F. H. Critical Solution Behavior in a Binary Mixture of Gaussian Molecules. II. *J. Chem. Phys.* **49,** 1232–1242 (1968) (Cited on page 79).

147. Baram, A. A Toeplitz representation for repulsive systems. *J. Phys. A* **16,** L19– (1983) (Cited on page 79).

148. Baram, A. & Rowlinson, J. S. Some mathematical properties of classical many-body systems with repulsive interactions. *J. Phys. A* **23,** L399– (1990) (Cited on page 79).

149. Baram, A. & Rowlinson, J. S. Studies of the Gaussian model I: The one-component system. *Mol. Phys.* **74,** 707–713 (1991) (Cited on page 79).

150. Baram, A., Maddox, M. & Rowlinson, J. S. Studies of the Gaussian model II: The two-component system. *Mol. Phys.* **76,** 1093–1101 (1992) (Cited on page 79).

151. Baram, A., Maddox, M. & Rowlinson, J. S. Studies of the Gaussian model III: The three-component system. *Mol. Phys.* **79,** 589–596 (1993) (Cited on page 79).

152. Dijkstra, M. & van Roij, R. Vapour-liquid coexistence for purely repulsive point-Yukawa fluids. *J. Phys.: Condens. Matter* **10,** 1219– (1998) (Cited on page 79).

153. Lang, A., Likos, C. N., Watzlawek, M. & Löwen, H. Fluid and solid phases of the Gaussian core model. *J. Phys.: Condens. Matter* **12,** 5087– (2000) (Cited on page 79).

154. Louis, A. A., Bolhuis, P. G. & Hansen, J. P. Mean-field fluid behavior of the Gaussian core model. *Phys. Rev. E* **62,** 7961–7972 (6 2000) (Cited on page 79).

155. Speedy, R. J. The energy-density landscape for soft spheres. *J. Phys.: Condens. Matter* **15,** S1243– (2003) (Cited on page 79).

156. Cinacchi, G. *et al.* Large attractive depletion interactions in soft repulsive-sphere binary mixtures. *J. Chem. Phys.* **127,** 214501 (2007) (Cited on page 79).

157. Glaser, M. A. *et al.* Soft spheres make more mesophases. *EPL* **78,** 46004 (2007) (Cited on page 79).

158. Saija, F., Prestipino, S. & Malescio, G. Anomalous phase behavior of a soft-repulsive potential with a strictly monotonic force. *Phys. Rev. E* **80,** 031502 (3 2009) (Cited on page 79).

159. Berthier, L., Flenner, E., Jacquin, H. & Szamel, G. Scaling of the glassy dynamics of soft repulsive particles: A mode-coupling approach. *Phys. Rev. E* **81,** 031505– (2010) (Cited on page 79).

160. Schmiedeberg, M., Haxton, T. K., Nagel, S. R. & Liu, A. J. Mapping the glassy dynamics of soft spheres onto hard-sphere behavior. *EPL* **96,** 36010– (2011) (Cited on page 79).

161. Russo, J. & Tanaka, H. Selection mechanism of polymorphs in the crystal nucleation of the Gaussian core model. *Soft Matter* **8,** 4206–4215 (2012) (Cited on page 79).

162. Travesset, A. Binary nanoparticle superlattices of soft-particle systems. *Proc Natl Acad Sci USA* (2015) (Cited on page 79).

163. Horst, N. & Travesset, A. Prediction of binary nanoparticle superlattices from soft potentials. *J. Chem. Phys.* **144,** 014502 (2016) (Cited on page 79).

164. Stillinger, F. H. Phase transitions in the Gaussian core system. *J. Chem. Phys.* **65,** 3968–3974 (1976) (Cited on pages 79, 82, 83).

165. Hansen J., P., Goulding, D. & van Roij, R. Effective interactions between charged colloidal particles : Repulsion, attraction and phase separation. *J. Phys. IV France* **10,** Pr5-27–Pr5-38 (2000) (Cited on page 79).

166. Prestipino, S., Saija, F. & Giaquinta, P. V. Phase diagram of softly repulsive systems: The Gaussian and inverse-power-law potentials. *J. Chem. Phys.* **123,** 144110 (2005) (Cited on page 79).

167. Prestipino, S., Saija, F. & Giaquinta, P. V. Phase diagram of the Gaussian-core model. *Phys. Rev. E* **71,** 050102(R) (2005) (Cited on page 79).

168. Malescio, G. & Pellicane, G. Stripe phases from isotropic repulsive interactions. *Nature Materials* **2,** 97 (2003) (Cited on page 79).

169. Mladek, B. M., Gottwald, D., Kahl, G., Neumann, M. & Likos, C. N. Formation of Polymorphic Cluster Phases for a Class of Models of Purely Repulsive Soft Spheres. *Phys. Rev. Lett.* **96,** 045701 (2006) (Cited on page 79).

170. Likos, C. N., Mladek, B. M., Gottwald, D. & Kahl, G. Why do ultrasoft repulsive particles cluster and crystallize? Analytical results from density-functional theory. *J. Chem. Phys.* **126,** 224502 (2007) (Cited on page 79).

171. Likos, C. N., Mladek, B. M., Moreno, A. J., Gottwald, D. & Kahl, G. Cluster-forming systems of ultrasoft repulsive particles: statics and dynamics. *Comput. Phys. Commun.* **179,** 71–76 (2008) (Cited on page 79).

172. Overduin, S. D. & Likos, C. N. Phase behaviour in binary mixtures of ultrasoft repulsive particles. *EPL* **85,** 26003– (2009) (Cited on page 79).

173. Archer, A. J., Likos, C. N. & Evans, R. Soft-core binary fluid exhibiting a λ-line and freezing to a highly delocalized crystal. *J. Phys.: Condens. Matter* **16,** L297–L303 (2004) (Cited on page 79).

174. Shin, H., Grason, G. M. & Santangelo, C. D. Mesophases of soft-sphere aggregates. *Soft Matter* **5,** 3629–3638 (2009) (Cited on page 79).

175. Shall, L. A. & Egorov, S. A. Structural and dynamical anomalies of a Gaussian core fluid: A mode-coupling theory study. *J. Chem. Phys.* **132,** 184504 (2010) (Cited on page 79).

176. Likos, C. N. *et al.* Star Polymers Viewed as Ultrasoft Colloidal Particles. *Phys. Rev. Lett.* **80,** 4450–4453 (20 1998) (Cited on page 79).

177. Watzlawek, M., Likos, C. N. & Löwen, H. Phase Diagram of Star Polymer Solutions. *Phys. Rev. Lett.* **82,** 5289–5292 (1999) (Cited on page 79).

178. Von Ferber, C., Jusufi, A., Watzlawek, M., Likos, C. N. & Löwen, H. Polydisperse star polymer solutions. *Phys. Rev. E* **62,** 6949–6956 (2000) (Cited on page 79).

179. Likos, C. N. Effective interactions in soft condensed matter physics. *Phys. Rep.* **348,** 267–439 (2001) (Cited on page 79).

180. Likos, C. N., Hoffmann, N., Löwen, H. & Louis, A. A. Exotic fluids and crystals of soft polymeric colloids. *J. Phys.: Condens. Matter* **14,** 7681– (2002) (Cited on pages 79, 82).

181. Likos, C. N. Soft matter with soft particles. *Soft Matter* **2,** 478–498 (2006) (Cited on page 79).

182. Mayer, C. *et al.* Asymmetric caging in soft colloidal mixtures. *Nat. Mater.* **7,** 780–784 (2008) (Cited on page 79).

183. Mladek, B. M., Kahl, G. & Likos, C. N. Computer Assembly of Cluster-Forming Amphiphilic Dendrimers. *Phys. Rev. Lett.* **100,** 028301 (2008) (Cited on page 79).

184. Mayer, C. *et al.* Multiple Glass Transitions in Star Polymer Mixtures: Insights from Theory and Simulations. *Macromolecules* **42,** 423–434 (2009) (Cited on page 79).

185. Camargo, M. & Likos, C. N. Interfacial and wetting behaviour of phase-separating ultrasoft mixtures. *Mol. Phys.* **109,** 1121–1132 (2011) (Cited on pages 79, 80).

186. Nikoubashman, A., Mahynski, N. A., Capone, B., Panagiotopoulos, A. Z. & Likos, C. N. Coarse-graining and phase behavior of model star polymer-colloid mixtures in solvents of varying quality. *J. Chem. Phys.* **143,** 243108 (2015) (Cited on page 79).

187. Nicolis, G. & Prigogine, I. *Self-Organization in Nonequilibrium Systems: From Dissipative Structures to Order Through Fluctuations* (Wiley, 1977) (Cited on pages 79, 80).

188. Witten, T. A. Insights from soft condensed matter. *Rev. Mod. Phys.* **71,** S367–S373 (1999) (Cited on page 79).

189. Marson, R. L., Phillips, C. L., Anderson, J. A. & Glotzer, S. C. Phase Behavior and Complex Crystal Structures of Self-Assembled Tethered Nanoparticle Telechelics. *Nano Lett.* **14,** 2071–2078 (2014) (Cited on page 79).

190. Kalsin, A. M. *et al.* Electrostatic Self-Assembly of Binary Nanoparticle Crystals with a Diamond-Like Lattice. *Science* **312,** 420 (2006) (Cited on page 79).

191. Miller, W. L. & Cacciuto, A. Hierarchical self-assembly of asymmetric amphiphatic spherical colloidal particles. *Phys. Rev. E* **80,** 021404 (2009) (Cited on page 79).

192. Ye, X. *et al.* Structural diversity in binary superlattices self-assembled from polymer-grafted nanocrystals. *Nature Communications* **6,** 10052 (2015) (Cited on page 79).

193. Kumar, A. & Molinero, V. Self-Assembly of Mesophases from Nanoparticles. *J. Phys. Chem. Lett.* **8,** 5053–5058 (2017) (Cited on page 79).

194. Ye, X., Chen, J. & Murray, C. B. Polymorphism in Self-Assembled AB6 Binary Nanocrystal Superlattices. *J. Am. Chem. Soc.* **133,** 2613–2620 (2011) (Cited on page 79).

195. Macfarlane, R. J. *et al.* Nanoparticle Superlattice Engineering with DNA. *Science* **334,** 204 (2011) (Cited on page 79).

196. Knorowski, C., Burleigh, S. & Travesset, A. Dynamics and Statics of DNA-Programmable Nanoparticle Self-Assembly and Crystallization. *Phys. Rev. Lett.* **106,** 215501 (2011) (Cited on pages 79, 80).

197. Knorowski, C. & Travesset, A. Materials design by DNA programmed self-assembly. *Curr. Opin. Solid State Mater. Sci.* **15,** 262–270 (2011) (Cited on pages 79, 80).

198. Henkel, M. & Pleimling, M. *Non-Equilibrium Phase Transitions: Volume 2: Ageing and Dynamical Scaling Far from Equilibrium* (Springer Netherlands, 2011) (Cited on pages 80, 89, 93).

199. Balluffi, R., Allen, S., Carter, W. & Kemper, R. *Kinetics Of Materials* (J. Wiley & Sons, 2005) (Cited on pages 80, 84, 89).

200. Archer, A. J. & Evans, R. Binary Gaussian core model: Fluid-fluid phase separation and interfacial properties. *Phys. Rev. E* **64,** 041501 (2001) (Cited on page 80).

201. Kambayashi, S. & Hiwatari, Y. Instability and phase separation of a binary mixture: The role of short-range repulsion and core-size ratio. *Phys. Rev. A* **46,** 1014–1021 (1992) (Cited on pages 80–82).

202. Stillinger, F. H. A Topographic View of Supercooled Liquids and Glass Formation. *Science* **267,** 1935– (1995) (Cited on page 81).

203. Stillinger, F. *Energy Landscapes, Inherent Structures, and Condensed-Matter Phenomena* (Princeton University Press, 2015) (Cited on pages 81, 86).

204. Wales, D. J. *Energy Landscapes: Applications to Clusters, Biomolecules and Glasses* (Cambridge University Press, 2003) (Cited on page 81).

205. Press, W., Teukolsky, S., Vetterling, W. & Flannery, B. *Numerical Recipes 3rd Edition: The Art of Scientific Computing* (Cambridge University Press, 2007) (Cited on pages 81, 85).

206. Uhlenbeck, G. & Ford, G. in *Series in physics* (eds de Boer, J. & Uhlenbeck, G.) v. 1, 182 (North-Holland Publishing Company, 1962) (Cited on pages 81–83).

207. Paula Leite, R., Freitas, R., Azevedo, R. & de Koning, M. The Uhlenbeck-Ford model: Exact virial coefficients and application as a reference system in fluid-phase free-energy calculations. *J. Chem. Phys.* **145,** 194101 (2016) (Cited on pages 81–83).

208. Paula Leite, R., Santos-Flórez, P. A. & de Koning, M. Uhlenbeck-Ford model: Phase diagram and corresponding-states analysis. *Phys. Rev. E* **96,** 032115– (2017) (Cited on pages 81–83).

209. Paula Leite, R. & de Koning, M. Nonequilibrium free-energy calculations of fluids using LAMMPS. *Comput. Mater. Sci.* **159,** 316–326 (2019) (Cited on pages 81–83).

210. Weeks, J. D., Chandler, D. & Andersen, H. C. Role of Repulsive Forces in Determining the Equilibrium Structure of Simple Liquids. *J. Chem. Phys.* **54,** 5237–5247 (1971) (Cited on pages 81, 82).

211. Larsen, P. M., Schmidt, S. & Schiötz, J. Robust structural identification via polyhedral template matching. *Modelling and Simulation in Materials Science and Engineering* **24,** 055007 (2016) (Cited on pages 84–86).

212. Laradji, M., Toxvaerd, S. & Mouritsen, O. G. Molecular Dynamics Simulation of Spinodal Decomposition in Three-Dimensional Binary Fluids. *Phys. Rev. Lett.* **77,** 2253–2256 (1996) (Cited on pages 84, 89).

213. Thakre, A. K., den Otter, W. K. & Briels, W. J. Domain formation and growth in spinodal decomposition of a binary fluid by molecular dynamics simulations. *Phys. Rev. E* **77,** 011503 (1 2008) (Cited on pages 84, 89).

214. Newman, M. Power laws, Pareto distributions and Zipf's law. *Contemp. Phys.* **46,** 323–351 (2005) (Cited on page 85).

215. Clauset, A., Shalizi, C. & Newman, M. Power-Law Distributions in Empirical Data. *SIAM Rev.* **51,** 661–703 (2009) (Cited on page 85).

216. Porter, D. A., Easterling, K. E. & Sherif, M. *Phase Transformations in Metals and Alloys (Revised Reprint)* (CRC Press, 2009) (Cited on page 87).